NATIONAL & INTERNATIONAL SCIENTIFIC EVENTS

33rd International Symposium on Power Semiconductor Devices and ICs (ISPSD)

Venue: Nagoya Congress Center
Location: Nagoya, Japan

Begins: May 30, 2021
Ends: June 3, 2021

35th IAS Meeting of Sedimentology

Venue: Conference Centre of the Vienna House Diplomat Hotel
Location: Prague, Czech Republic

Begins: June 22, 2021
Ends: June 24, 2021

39th IAHR World Congress

Venue: Palacio de Congresos de Granada
Location: Granada, Spain

Begins: July 4, 2021
Ends: July 9, 2021

50th International Congress and Exposition on Noise Control Engineering

Venue: Marriott Wardman Park
Location: Washington, USA

Begins: August 1, 2021
Ends: August 4, 2021

25th International Congress of Theoretical and Applied Mechanics

Venue: MiCo Congress Centre
Location: Milano, Italy

Begins: August 22, 2021
Ends: August 27, 2021

20th International Conference on Soil Mechanics and Geotechnical Engineering 2021

Venue: International Convention Centre
Location: Sydney, Australia

Begins: September 12, 2021
Ends: September 17, 2021

18th International Conference on Microwave and High Frequency Applications (AMPERE 2021)

Venue: Chalmers University of Technology
Location: Gothenburg, Sweden

Begins: September 13, 2021
Ends: September 16, 2021

14th Mediterranean Congress of Chemical Engineering

Venue: Gran Via Venue, Pavillion 3
Location: Barcelona, Spain

Begins: September 14, 2021
Ends: September 17, 2021

17th International Symposium on Biopolymers (ISBP 2021)

Venue: Congress Center Le Regent
Location: Crans-Montana, Switzerland

Begins: September 14, 2021
Ends: September 17, 2021

2021 International Conference on Smart Transportation and Future Mobility (CSTFM 2021)

Location: Frankfurt, Germany

Begins: September 17, 2021
Ends: September 19, 2021

8th World Congress on Engineering and Technology (CET 2021)

Venue: The Grand Dynasty Culture Hotel
Location: Xi'an, China

Begins: October 22, 2021
Ends: October 24, 2021

42nd Ibero-Latin-American Congress on Computational Methods in Engineering (XLII CILAMCE)

Location: Rio de Janeiro, Brazil

Begins: November 09, 2021
Ends: November 12, 2021

Abstracted & Indexed in:

TR Dizin Mühendislik ve Temel Bilimler Veri Tabanı | CrossRef | Google Scholar | MIP Database | StuartxChange | ResearchBib | Scientific Indexing Services (SIS)

HITTITE

HJSE Official Journal of Hitit University Volume 8, Issue 1, 2021 www.hjse.hitit.edu.tr

HITIT UNIVERSITY

ISSN 2148-4171

JOURNAL OF SCIENCE & ENGINEERING

HITTITE

HJSE Official Journal of Hitit University Volume 8, Issue 1, 2021 www.hjse.hitit.edu.tr

Volume 8, Issue 1, 2021

www.hjse.hitit.edu.tr

JOURNAL OF SCIENCE & ENGINEERING
HITTITE

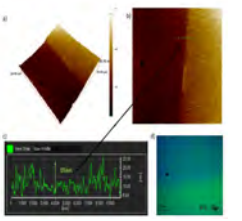

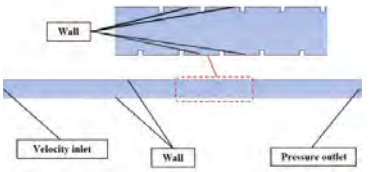

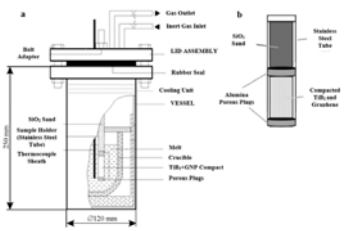

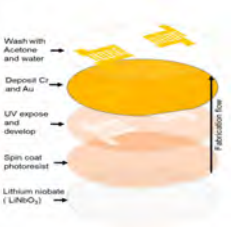

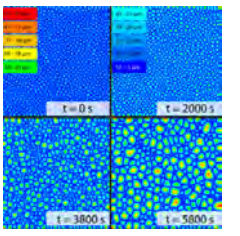

JOURNAL OF SCIENCE & ENGINEERING
HITTITE

CONTENT

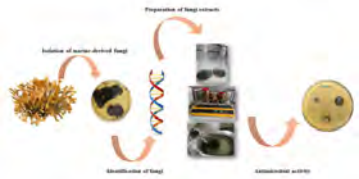

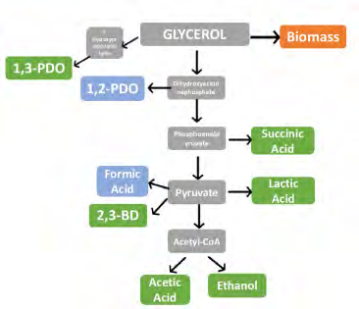

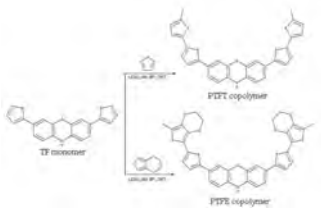

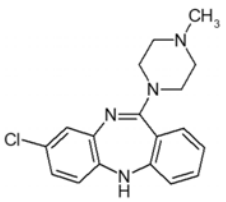

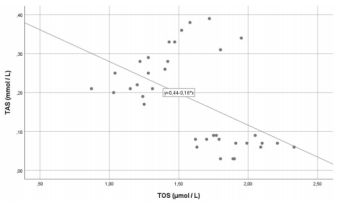

Owner
Prof. Dr. Ali Osman ÖZTÜRK on behalf of Hitit University

Editor-in-chief
Prof. Dr. Ali KILIÇARSLAN

Associate Editors
Prof. Dr. D. Ali KÖSE
Assist. Prof. Dr. Öncü AKYILDIZ

Production
Assoc. Prof. Dr. Kazım KÖSE
Res. Asst. Dr. Erhan ÇETİN
Res. Asst. Mustafa Reşit HABOĞLU
Res. Asst. Harun Emre KIRAN
Res. Asst. Ömer Faruk TOZLU
Lect. Tugrul YILDIRIM

Editor's Office
Tel: +90 364 227 45 33 / 12 36
Fax: +90 364 227 45 35
Email: alikilicarslan@hitit.edu.tr

Subscription Service:
Tel: +90 364 227 45 33 / 12 82
Fax: +90 364 227 45 35
Email: hjse@hitit.edu.tr

EDITORIAL BOARD

Journal Name	: HITTITE JOURNAL OF SCIENCE AND ENGINEERING
Year	: 2021
Managing Editor	: Prof. Dr. Ali KILIÇARSLAN
Managing Office	: Hitit University Faculty of Engineering
Managing Office Tel	: +90 364 227 45 33 / 12 36
Publication Language	: English
Publication Type	: Peer Reviewed, Open Access, International Journal
Delivery Format	: 4 times a year (quarterly)
Print ISSN	: 2149-2123
Online ISSN	: 2148-4171
Publisher Address	: Hitit Üniversitesi Kuzey Kampüsü Çevre Yolu Bulvarı 19030 Çorum / TÜRKİYE
Publisher Tel	: +90 364 227 45 33/1236

This new issue of Hittite Journal of Science and Engineering contains twelve manuscripts from the disciplines of chemistry, molecular biology and genetics, bioengineering, food science and engineering, mechanical engineering, electrical and electronics engineering, materials science and engineering. These manuscripts was first screened by Section Editors using plagiarism prevention software and then reviewed and corrected according to the reviewer's comments. I would like to express my gratitude to all our authors and contributing reviewers of this issue.

I would like to thank to the new President of Hitit University, Prof. Dr. Ali Osman Öztürk, for his support and interest in HJSE and also to the Section Editors of HJSE, namely Prof. Dr. Dursun Ali Kose and Assoc. Prof. Dr. Oncu Akyildiz, as well as our Production Editors Assoc. Prof. Dr. Kazim Kose, Mustafa Reşit Haboğlu, Dr. Erhan Çetin, Tugrul Yildirim, Harun Emre Kıran and Ömer Faruk Tozlu for their invaluable efforts in making of the journal.

It's my pleasure to invite the researchers and scientists from all branches of science and engineering to join us by sending their best papers for publication in Hittite Journal of Science and Engineering.

Prof. Dr. Ali Kilicarslan

Editor-in-Chief

Hittite Journal of Science and Engineering, 2021, 8(1) 01-05
ISSN NUMBER: 2148-4171
DOI: 10.17350/HJSE19030000206

Fabrication and Analysis Of 2D/3D Heterojunction Between Continuous Few-layer WS_2 Film and Si (100)†

Merve Acar[1] **Soheil Mobtakeri**[2] **Mehmet Ertugrul**[1] **Emre Gur**[2]
[1]Ataturk University, Department of Electrical and Electronics Engineering, Erzurum, Turkey
[2]Ataturk University, Department of Physics, Erzurum, Turkey

ABSTRACT

Transition metal dichalcogenide (TDMCs) placed on a 3D semiconductor substrate have leads to significant advances in the electronic industry with new opportunities based on 2D/3D heterojunction based diverse devices without any restrictions, such as lattice compatibility. In this study, magnetron sputtering technique was used to grow layered tungsten disulfide (WS_2) thin films onto p-Si and thus WS_2/p-Si heterojunctions were created. The structural and chemical parameters of this sputtered WS_2 films were investigated using Raman spectroscopy, X-ray photoelectron spectroscopy (XPS) and atomic force microscopy (AFM). Electrical characterization of WS_2/p-Si heterojunction was also obtained to investigate Log (I)-V and linear I-V characteristics. A typical diode like I-V behavior was observed with a five-ordered rectifying ratio. It was observed that the heterojunction has a barrier height of 0.48 eV, the leakage current at -0.2 V is 2.25×10^{-6} A and the ideality factor is 5.7. This work show that single step magnetron sputtering WS_2/p-Si heterojunction has great importance for heterojunction based future nanoelectronic devices.

Article History:
Received: 2020/05/30
Accepted: 2020/12/27
Online: 2021/03/31

***Correspondence to**: Emre Gür, Deparment of Electrical and Electronics Engineering, Atatürk University, Erzurum, Turkey*
Tel: +90 442 236 6733
Fax: +90 442 236 0948
E-Mail:emregur@atauni.edu.tr

Keywords:
2D materials, TMDC, WS_2, 2D/3D heterojunctions

INTRODUCTION

The excellent electronic properties of the various two-dimensional (2D) materials have led to new developments for the nanoelectronic devices after discovering of the graphene. Heterostructures created by using 2D and 3D materials are becoming one of the main research area for the nanoelectronic devices in recent years [1]. TMDCs such as WS_2, MoS_2, $MoSe_2$, and WSe_2 have adjustable bandgaps to be indirect in their bulk form and direct in the monolayer [2]. This feature has potential in various electronic and optical applications for TMDCs [3]. Structurally, WS_2 has a crystal structure consisting of S-W-S sandwich layers and the atoms in the layers are packaged hexagonally [4]. These layers are held together by the weak van der Waals (vdW) forces so WS_2 can easily be converted into a single layer form [5]. Because of these significant features, WS_2 has become a good candidate for the new generation micro and nanoelectronics [6]. Unlike the graphene, the WS_2 has a direct band gap semiconductor with a gap of 2.1 eV in single layer form while as the material passes into a bulk form, the gap is direct in the size of 1.3 eV [7]. The presence of this bandgap made it possible to produce WS_2 transistors with a 10^8 on/off ratio and high sensitivity photo detectors [8].

Integration of TMDCs with 3D materials such as Si and GaN offers interesting opportunities. Lattice matching is very important in the integration of different bulk semiconductors [9, 10]. These heterojunction can be vertical and lateral structures, without lattice matching restrictions [11]. 2D vdW heterostructures offer unique features compared to TMDC devices. Recently, researchers have begun to study various heterojunction device based on 2D/3D materials [12].

MoS_2/Si heterojunctions have found used in high performance device applications such as photodetectors [13-15] and solar cells [16]. It has also been studied MoS_2/GaAs [17], MoS_2/InP [18], MoS_2/SiC [19, 20] and MoS_2/GaN heterojunctions [12, 16, 21-26] for a diverse applications. MoS_2/WSe_2 [27-29] and MoS_2/GaN [12, 25] heterojunctions based devices have also found a place in different electronic device applications. On the other hand, heterojunction based devices have also been carried out with 2D WS_2. WS_2/Si p-n junction was fabricated and rectifying characteristics was demonstrated [30]. GaN and WS_2 monolayers have the same crystal structures and lattice constants compatible with each other, WS_2/GaN junction was fabricated with wafer-

scale grown WS_2 film [31]. In another study, WS_2/GaN heterojunction was manufactured for UV detection [32].

Large area and continuous WS_2 thin film creation is a crucial step for nanoelectronic device production [33, 34]. WS_2 films can be prepared in two different ways: top-down or bottom-up. The top-down method contains exfoliation method (mechanical or chemical) is not suitable for commercialization, as is not possible to control the thickness and size of WS_2 films in this method [35]. The chemical vapor deposition (CVD) method from bottom-up methods is the most widely used method [36]. Although large area single crystal 2D graphene can be grown with this method. However, TMDC (MoS_2, WS_2) creation of wafer-scale single-layer films with the CVD method [37]. It is important to create the heterojunction with large area WS_2 thin films [38] and Si. Therefore, integration of WS_2 with Si, multifunctional devices can be realized. However, there are no studies on the production of heterojunctions composed of single step sputtered WS_2 thin films and Si.

In this study, the magnetron sputtering method was utilized to produce a continuous and centimeter size WS_2 film with a thickness of ~ 15 nm. WS_2 thin films were sputtered on p-type Si to produce 2D/3D heterojunctions.

MATERIAL AND METHODS

The resistivity of the highly doped p type silicon was used in this study to prepare WS_2/Si heterojunction. Before the fabrication of devices, Si substrates were cleaned by using RCA procedure. Afterward Si substrate rinsed in DI water and dried N_2 gas. The fabrication process WS_2/Si heterojunction is given step by step as shown in Fig. 1. Before the growth of WS_2 on Si, the Al was created on the unpolished side of the Si in a sputter system and p-Si/Al was annealed to achieve ohmic contact in N_2 gas flow at 540 ° C for 3 minutes. WS_2 thin continuous films were grown on p-Si (100) substrate for the 10s at 5×10-7 Torr base pressure and 20mTorr growth pressure. Substrate temperature and sputtering power were set to the 300 °C and 120 W respectively. Ar gas was adjusted as 220 sccm. Schematic diagram of deposition of WS_2 by magnetron sputtering is shown in Fig. 2. AZ5214 photoresist was coated for lithography and then exposed under UV light. Then, 5/50 nm thick Ti/Pt contacts were deposited on the WS_2 layer using sputtering at 10^{-6} Torr base pressure and 20mTorr growth pressure in Ar ambient. After coating, using lift-off process Ti/Pt contacts were created as square with dimensions of 150µ×150µ. For the electrical characterization DC voltage was applied to the top and bottom contacts at atmosphere condition.

Before the fabrication process, structural and chemical properties of the WS_2 layer were characterized using Raman

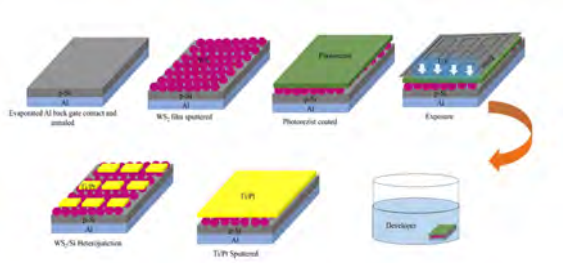

Figure 1. Schematic fabrication procedure of WS_2/Si heterojunction.

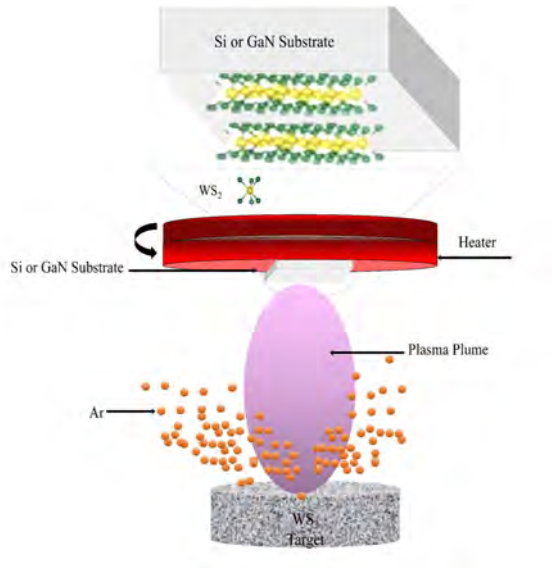

Figure 2. Schematic illustration of the sputtering process.

spectroscopy (Witec Alfa-300), XPS (SPECs Flex-Mod) and AFM measurement.

Once and for all, the current (I)-voltage (V) characteristics of WS_2/Si heterojunctions were determined using Keithley 2400 source meter at atmosphere condition.

RESULTS AND DISCUSSION

Raman spectroscopy used to sputtered growth WS_2 film. Fig. 3 shows the Raman spectrum of a few layers WS_2 films on p-Si substrates. The Raman two important modes, E^1_{2g} at 340, 4 cm^{-1} and A_{1g} at 406, 5 cm^{-1} of the grown multilayer WS_2 film. The peak difference between E^1_{2g} and A_{1g} mode Raman peaks are measured as 66.1 cm^{-1}, which demonstrates the presence of the multilayer WS_2 film [39].

Moreover, the surface morphology of the few layer WS_2 film on p-Si substrate is analyzed by optic microscope images and AFM characterizations, the results are shown in Fig. 4. In Fig. 4(a) 3D AFM images clearly show the step formed at the interface where WS_2 grown on p-Si. Drawn green line in Fig. 4(b) is show height profile of the surface. It can be seen from the Fig. 4(c) that the thickness of 10 s grown WS_2

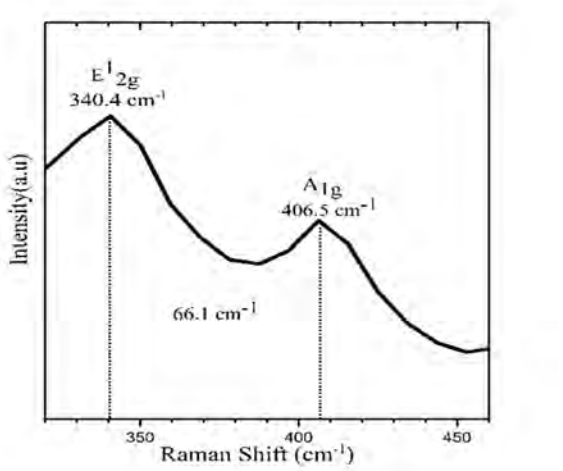

Figure 3. Raman spectrum of the grown continuous few layer WS_2 films on p-Si substrate.

film is 15 nm. Fig. 4(d) shows an optical microscope image of 2D WS_2 thin films where continuous and uniform films can be easily seen over a large area.

Chemical composition of the WS_2 film was analyzed with XPS measurement. XPS W 4f spectrum of WS_2 film is shown in figure 5(a). The peaks observed W $4_{f7/2}$ at 32.0 eV, W $4_{f5/2}$ at 34.8 eV and W $5_{p3/2}$ at 38 eV. Fig. 5(b) illustrates the S 2p spectra; the peaks identified S $2_{p3/2}$ at 162. 98 eV. Atomic ratio of the S/W is also determined from the XPS measurements as 1.38. These XPS result confirms that S deficient WS_2 films were successfully grown by sputtering.

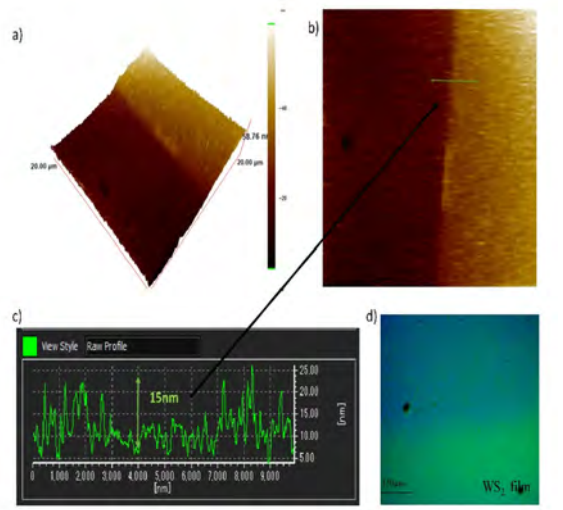

Figure 4. a) An AFM 3D image of few layer WS2 film. b) Large area scanned AFM image of the WS_2-Si interface. c) Height profile showing the thickness of WS_2 passing through the green line in b). d) An optical microscope image of a few layer continuous WS_2 film growth on p-Si substrate.

I-V measurements were performed under atmosphere conditions to evaluate the electrical properties of the WS_2/p-

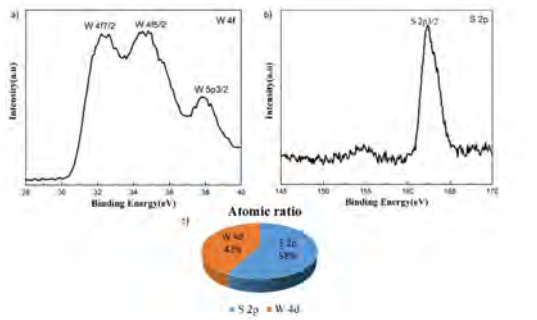

Figure 5. XPS spectrum of a) W 4f and b) S 2p spectrums of the WS_2 film on Si c) Atomic ratio of WS_2 film.

Si heterojunction. I-V graph of WS_2/p-Si heterojunction taken between -2 volts and +2 volts is given in Fig. 6. The linear and logarithmic I-V curve are shown in Fig. 6(a) and 6(b). Fig. 6(c) shows schematic representation of Al back gated WS_2/Si heterojunction with connections. The log I-V curves shows diode like rectifying characteristic with rectification ratio over 10^5 in the range of ±2V. Almost saturated I-V curve for reverse bias depicts the less interface effects at the junction. The leakage current is about 2.28×10^{-6} A at −0.2V was observed. The turn on voltage, which is the point where the current starts to increase rapidly, was observed at 0.5 V.

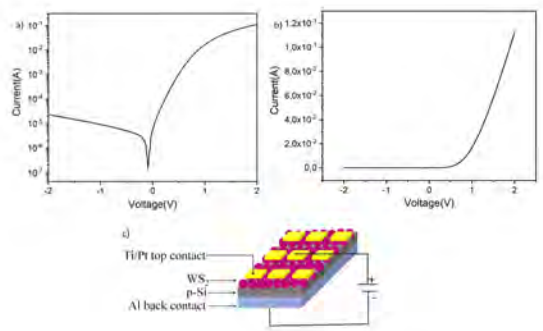

Figure 6. I–V characteristics of the heterojunction on a) logarithmic and b) linear scales in the atmosphere condition. c) Schematic representation of WS_2/Si heterojunction.

As in the metal-semiconductor contact of the WS_2/Si heterojunction, the carrier transport is mainly caused by minority charge carriers. But in this article, since Si is highly doped, it may work like a unilateral Schottky junction. Thermionic emission (TE) current equation can be used to calculate ideality factor (n) and barrier height (Φb). For this, the slope and intersection of the log I-V curve are used. The current passing through the WS_2/p-Si heterojunction as defined the theory of TE, as in the following Eq. 1:

$$I = I_0 \exp\left(\frac{qV}{nkT}\right)\left[1-\exp\left(-\frac{qV}{kT}\right)\right] \quad (1)$$

where q:electronic charge, v:applied voltage, T:temperature, k:Boltzmann constant, n:ideality factor, I_0:

reverse saturation current. The ideality factor (n) is calculated from forward bias linear region of the ln (I) -V graph using the following Eq. 2:

$$n = \frac{q}{kT}\left(\frac{dV}{d(lnI)}\right) \quad (2)$$

In addition, another important parameter, Barrier height (Φb), can be calculated using the Eq. 3 below.

$$\Phi b = \frac{kT}{q} In\left(\frac{AA^{*}T^{2}}{I_{0}}\right) \quad (3)$$

A: area and A*: effective Richardson constant (32 $Acm^{-2}K^{-2}$ for Si). Ideality factor (n) and barrier height (Φb) accounted for the WS_2/p-Si heterojunction according to the above equations, the corresponding values were 5.7 and 0.48 eV, respectively. The ideality factor value (n) is greater than 1 when there is the presence of interface layer or surface conditions, the effect of series resistance, the height of the barrier caused by interface defects and manufacturing defects. The larger ideality factor might show that current carrying mechanisms is other than thermionic emissions [40].

CONCLUSION

In summary, large-area and continuous few layer WS_2 films were synthesized on the p-Si by single step magnetron sputtering successfully. WS_2/Si heterojunction device was fabricated by lithography. Electrical measurements shows that the WS_2/Si heterojunction have remarkable rectifying behavior, around 10^5. This type heterojunctions might be advantageous for future nano and optoelectronic device applications.

REFERENCES

1. Jariwala, D.; Marks, T. J.; Hersam, M. C., Mixed-dimensional van der Waals heterostructures. Nature materials 2017, 16 (2), 170-181.
2. Liu, B. L.; Abbas, A.; Zhou, C. W., Two-Dimensional Semiconductors: From Materials Preparation to Electronic Applications. Adv Electron Mater 2017, 3 (7).
3. Shim, J.; Park, H. Y.; Kang, D. H.; Kim, J. O.; Jo, S. H.; Park, Y.; Park, J. H., Electronic and Optoelectronic Devices based on Two-Dimensional Materials: From Fabrication to Application. Adv Electron Mater 2017, 3 (4).
4. Choi, W.; Choudhary, N.; Han, G. H.; Park, J.; Akinwande, D.; Lee, Y. H., Recent development of two-dimensional transition metal dichalcogenides and their applications. Mater Today 2017, 20 (3), 116-130.
5. Sumesh, C. K., Temperature dependant electronic charge transport characteristics at MX2 (M=Mo,W; X=S, Se)/Si heterojunction devices. J Mater Sci-Mater El 2019, 30 (4), 4117-4127.
6. Wang, Q. H.; Kalantar-Zadeh, K.; Kis, A.; Coleman, J. N.; Strano, M. S., Electronics and optoelectronics of two-dimensional transition metal dichalcogenides. Nature nanotechnology 2012, 7 (11), 699.
7. Ahmed, S.; Yi, J., Two-dimensional transition metal dichalcogenides and their charge carrier mobilities in field-effect transistors. Nano-Micro Lett 2017, 9 (4), 50.
8. Ye, M.; Zhang, D.; Yap, Y. K., Recent advances in electronic and optoelectronic devices based on two-dimensional transition metal dichalcogenides. Electronics 2017, 6 (2), 43.
9. Dong, R.; Kuljanishvili, I., Progress in fabrication of transition metal dichalcogenides heterostructure systems. Journal of Vacuum Science & Technology B, Nanotechnology and Microelectronics: Materials, Processing, Measurement, and Phenomena 2017, 35 (3), 030803.
10. Gupta, P.; Rahman, A.; Subramanian, S.; Gupta, S.; Thamizhavel, A.; Orlova, T.; Rouvimov, S.; Vishwanath, S.; Protasenko, V.; Laskar, M. R., Layered transition metal dichalcogenides: promising near-lattice-matched substrates for GaN growth. Sci Rep-Uk 2016, 6, 23708.
11. Wang, J. W.; Li, Z. Q.; Chen, H. Y.; Deng, G. W.; Niu, X. B., Recent Advances in 2D Lateral Heterostructures. Nano-Micro Lett 2019, 11 (1).
12. O'Regan, T. P.; Ruzmetov, D.; Neupane, M. R.; Burke, R. A.; Herzing, A. A.; Zhang, K.; Birdwell, A. G.; Taylor, D. E.; Byrd, E. F.; Walck, S. D., Structural and electrical analysis of epitaxial 2D/3D vertical heterojunctions of monolayer MoS2 on GaN. Appl Phys Lett 2017, 111 (5), 051602.
13. Li, B.; Shi, G.; Lei, S.; He, Y.; Gao, W.; Gong, Y.; Ye, G.; Zhou, W.; Keyshar, K.; Hao, J., 3D band diagram and photoexcitation of 2D–3D semiconductor heterojunctions. Nano Lett 2015, 15 (9), 5919-5925.
14. Krishnamoorthy, S.; Lee, E. W.; Lee, C. H.; Zhang, Y.; McCulloch, W. D.; Johnson, J. M.; Hwang, J.; Wu, Y.; Rajan, S., High current density 2D/3D MoS2/GaN Esaki tunnel diodes. Appl Phys Lett 2016, 109 (18), 183505.
15. Esmaeili-Rad, M. R.; Salahuddin, S., High performance molybdenum disulfide amorphous silicon heterojunction photodetector. Sci Rep-Uk 2013, 3 (1), 1-6.
16. Hao, L.; Liu, Y.; Gao, W.; Han, Z.; Xue, Q.; Zeng, H.; Wu, Z.; Zhu, J.; Zhang, W., Electrical and photovoltaic characteristics of MoS2/Si pn junctions. J Appl Phys 2015, 117 (11), 114502.
17. Hao, L.; Liu, Y.; Han, Z.; Xu, Z.; Zhu, J., Large lateral photovoltaic effect in MoS 2/GaAs heterojunction. Nanoscale research letters 2017, 12 (1), 562.
18. Lin, S.; Wang, P.; Li, X.; Wu, Z.; Xu, Z.; Zhang, S.; Xu, W., Gate tunable monolayer MoS2/InP heterostructure solar cells. Appl Phys Lett 2015, 107 (15), 153904.
19. Lee, E. W.; Ma, L.; Nath, D. N.; Lee, C. H.; Arehart, A.; Wu, Y.; Rajan, S., Growth and electrical characterization of two-dimensional layered MoS2/SiC heterojunctions. Appl Phys Lett 2014, 105 (20), 203504.
20. Din, H.; Idrees, M.; Rehman, G.; Nguyen, C. V.; Gan, L.-Y.; Ahmad, I.; Maqbool, M.; Amin, B., Electronic structure, optical and photocatalytic performance of SiC–MX 2 (M= Mo, W and X= S, Se) van der Waals heterostructures. Phys Chem Chem Phys 2018, 20 (37), 24168-24175.
21. Zhang, K.; Jariwala, B.; Li, J.; Briggs, N. C.; Wang, B.; Ruzmetov, D.; Burke, R. A.; Lerach, J. O.; Ivanov, T. G.; Haque, M., Large scale 2D/3D hybrids based on gallium nitride and transition metal dichalcogenides. Nanoscale 2018, 10 (1), 336-341.
22. Ruzmetov, D.; Zhang, K.; Stan, G.; Kalanyan, B.; Bhimanapati, G. R.; Eichfeld, S. M.; Burke, R. A.; Shah, P. B.; O'Regan, T. P.; Crowne, F. J., Vertical 2D/3D semiconductor heterostructures

based on epitaxial molybdenum disulfide and gallium nitride. Acs Nano 2016, 10 (3), 3580-3588.
23. Liao, J.; Sa, B.; Zhou, J.; Ahuja, R.; Sun, Z., Design of high-efficiency visible-light photocatalysts for water splitting: MoS2/AlN (GaN) heterostructures. The Journal of Physical Chemistry C 2014, 118 (31), 17594-17599.
24. Jeong, H.; Bang, S.; Oh, H. M.; Jeong, H. J.; An, S.-J.; Han, G. H.; Kim, H.; Kim, K. K.; Park, J. C.; Lee, Y. H., Semiconductor–insulator–semiconductor diode consisting of monolayer MoS2, h-BN, and GaN heterostructure. Acs Nano 2015, 9 (10), 10032-10038.
25. Lee, E. W.; Lee, C. H.; Paul, P. K.; Ma, L.; McCulloch, W. D.; Krishnamoorthy, S.; Wu, Y.; Arehart, A. R.; Rajan, S., Layer-transferred MoS2/GaN PN diodes. Appl Phys Lett 2015, 107 (10), 103505.
26. Tangi, M.; Mishra, P.; Ng, T. K.; Hedhili, M. N.; Janjua, B.; Alias, M. S.; Anjum, D. H.; Tseng, C.-C.; Shi, Y.; Joyce, H. J., Determination of band offsets at GaN/single-layer MoS2 heterojunction. Appl Phys Lett 2016, 109 (3), 032104.
27. Nourbakhsh, A.; Zubair, A.; Dresselhaus, M. S.; Palacios, T. s., Transport properties of a MoS2/WSe2 heterojunction transistor and its potential for application. Nano Lett 2016, 16 (2), 1359-1366.
28. Roy, T.; Tosun, M.; Cao, X.; Fang, H.; Lien, D.-H.; Zhao, P.; Chen, Y.-Z.; Chueh, Y.-L.; Guo, J.; Javey, A., Dual-gated MoS2/WSe2 van der Waals tunnel diodes and transistors. Acs Nano 2015, 9 (2), 2071-2079.
29. Lee, C.-H.; Lee, G.-H.; Van Der Zande, A. M.; Chen, W.; Li, Y.; Han, M.; Cui, X.; Arefe, G.; Nuckolls, C.; Heinz, T. F., Atomically thin p–n junctions with van der Waals heterointerfaces. Nature nanotechnology 2014, 9 (9), 676.
30. Aftab, S.; Khan, M. F.; Min, K.-A.; Nazir, G.; Afzal, A. M.; Dastgeer, G.; Akhtar, I.; Seo, Y.; Hong, S.; Eom, J., Van der Waals heterojunction diode composed of WS2 flake placed on p-type Si substrate. Nanotechnology 2017, 29 (4), 045201.
31. Yu, Y.; Fong, P. W.; Wang, S.; Surya, C., Fabrication of WS 2/GaN pn Junction by Wafer-Scale WS 2 Thin Film Transfer. Sci Rep-Uk 2016, 6, 37833.
32. Zhao, Z. H.; Wu, D.; Guo, J. W.; Wu, E. P.; Jia, C.; Shi, Z. F.; Tian, Y. T.; Li, X. J.; Tian, Y. Z., Synthesis of large-area 2D WS2 films and fabrication of a heterostructure for self-powered ultraviolet photodetection and imaging applications. J Mater Chem C 2019, 7 (39), 12121-12126.
33. Tang, H.; Zhang, H.; Chen, X.; Wang, Y.; Zhang, X.; Cai, P.; Bao, W., Recent progress in devices and circuits based on wafer-scale transition metal dichalcogenides. Science China Information Sciences 2019, 62 (12), 220401.
34. Zavabeti, A.; Jannat, A.; Zhong, L.; Haidry, A. A.; Yao, Z.; Ou, J. Z., Two-Dimensional Materials in Large-Areas: Synthesis, Properties and Applications. Nano-Micro Lett 2020, 12 (1), 1-34.
35. Brent, J. R.; Savjani, N.; O'Brien, P., Synthetic approaches to two-dimensional transition metal dichalcogenide nanosheets. Prog Mater Sci 2017, 89, 411-478.
36. Cai, Z.; Liu, B.; Zou, X.; Cheng, H.-M., Chemical vapor deposition growth and applications of two-dimensional materials and their heterostructures. Chemical reviews 2018, 118 (13), 6091-6133.
37. Wong, S. L.; Liu, H.; Chi, D., Recent progress in chemical vapor deposition growth of two-dimensional transition metal dichalcogenides. Progress in Crystal Growth and Characterization of Materials 2016, 62 (3), 9-28.
38. Koçak, Y.; Gür, E., Growth control of WS2; from 2D layer by layer to 3D vertical standing Nano-Walls. Acs Appl Mater Inter 2020.
39. Berkdemir, A.; Gutiérrez, H. R.; Botello-Méndez, A. R.; Perea-López, N.; Elías, A. L.; Chia, C.-I.; Wang, B.; Crespi, V. H.; López-Urías, F.; Charlier, J.-C., Identification of individual and few layers of WS 2 using Raman spectroscopy. Sci Rep-Uk 2013, 3 (1), 1-8.
40. Gora, V.; Chawanda, A.; Nyamhere, C.; Auret, F. D.; Mazunga, F.; Jaure, T.; Chibaya, B.; Omotoso, E.; Danga, H. T.; Tunhuma, S. M., Comparison of nickel, cobalt, palladium, and tungsten Schottky contacts on n-4H-silicon carbide. Physica B: Condensed Matter 2018, 535, 333-337.

Hittite Journal of Science and Engineering, 2021, 8 (1) 07–17
ISSN NUMBER: 2148–4171
DOI: 10.17350/HJSE19030000207

Computational Study On The Effect Of The Staggered Ribs On Heat Transfer Phenomena Between The Horizontal Plates

Ilker Goktepeli **Ulas Atmaca**
Konya Technical University, Department of Mechanical Engineering, Konya, Turkey

ABSTRACT

In terms of multifarious technical applications, various kinds of passive methods are preferred to the active techniques when it comes to increase the amount of convection heat transfer via less energy consumption. As a vortex generator within the scope of the passive method, rib is usually employed to induce the heat transfer enhancement. In this study, the rectangular cross-sectional ribs have been placed to increase the amount of the heat transfer for the staggered arrangement between the horizontal parallel plates. Numerical simulations have been conducted by using k-ω SST turbulence model at Re = 10000. The rib effect has been comparatively investigated in case of thermal and hydraulic performance presented via the numerical results. Time-averaged results for temperature, pressure, streamwise velocity component and streamline patterns have been presented in terms of contour graphics. Furthermore, heat transfer enhancement by using the ribs has been given depending on the increment ratio of Nusselt numbers. Including friction losses due to the ribs mounted on the plates, the values of thermal performance factor for all ducts have been calculated. According to these results for heat transfer augmentation at Re = 10000, h' = 0.1 with S' = 0.5 having η = 1.049 and h' = 0.1 with S' = 0.75 having η = 1.019 have been recommended rather than the smooth duct.

Article History:
Received: 2020/09/02
Accepted: 2021/03/12
Online: 2021/03/31

***Correspondence to**: Ilker Goktepeli, Deparment of Mechanical Engineering, Konya Technical University, Konya, Turkey*

E-Mail:igoktepeli@ktun.edu.tr

Keywords:
Heat transfer enhancement, k-ω SST, Ribbed plate, Staggered arrangement, Thermal performance

INTRODUCTION

Heat transfer enhancement via passive methods is accepted as a popular subject in the engineering disciplines since it draws interests for the power expenditure reduction of the system while improving thermal performance. For instance, mechanism in ribbed channels is a challenging issue for the development of high-performance cooling or heating units requiring less cooling working fluid (Sundén, 2011). However, the working fluid having lower thermal diffusivity is a potential restrictive component for the thermal system in some cases as also pointed out by Kashyap et al. (2018). Therefore, the main goal is to increase the amount of convective heat transfer via various techniques depending on the conditions. It is possible to emphasize that all passive techniques are almost based on the extension of wetted surface area by mounting artificial surface elements or the interruption of both hydrodynamic and thermal boundary layers by escalating the flow mixing. What is more, the interruption of these layers makes compactness higher in the duct (Yang and Chen, 2015). On that note, a rib is not only preferred as an artificial surface element for heat transfer enhancement but also it is used to boost the turbulence intensity for the increment of the thermal performance in the ducts. As stated by Alfarawi et al. (2017), passive heat transfer enhancement method is fundamentally applied for the disruption of the profiles near to the plates as well as the production of recirculation regions in the vicinity of the artificial surface elements. Furthermore, it is known that the vortices tend to follow swirling paths provoking the fluid displacement between the core zones and the plates (Tiggelbeck et al., 1993). Thus, the amount of convection heat transfer is enhanced by dispatching more fresh fluid towards the plates with respect to the study done by Abdollahi and Shams (2015). These aforementioned situations cause the increment of the local heat transfer coefficient. The rectangular cross-sectional ribs have been placed on the plates in this study for this reason. Although various kinds of vortex generators are encountered in the previous works studies done by Ki-

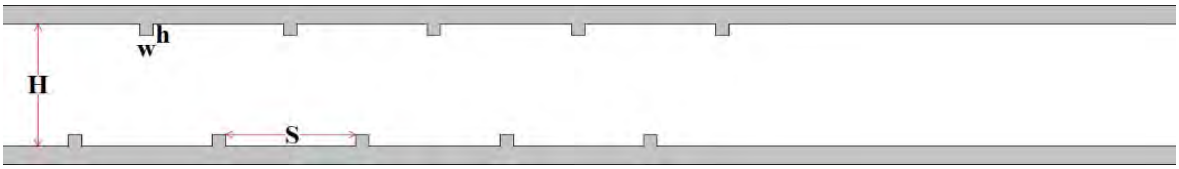

Figure 1. The schematic of the duct with the staggered ribs

licaslan and Sarac (1998), Sripattanapipat and Promvonge (2009), Manca et al. (2011), Wongcharee et al. (2011), Ahmed et al. (2013) and Aslan et al. (2016) on the augmentation of heat transfer, the rib having the rectangular shape is one of the most frequently used elements in terms of heat transfer augmentation. As the rib design is crucial for the level of heat transfer enhancement, also its orientations and arrangements affect the thermal performance for the considered problem. Another supportive study prepared by Moon et al. (2014) reaches a conclusion over the improvement of thermal performance via the ribs. What is more, it has been explained with the influence of the rib shape and its arrangement on the separation bubble and the fluctuations triggering the turbulent kinetic energy. If it is briefly stated, staggered arrangement has been found useful to place the rectangular ribs on the horizontal plates. It does not matter that cooling or heating is aspired in the ducts where the working fluid is used, the staggered baffles are placed to improve the efficiency of thermal process as similar approach proposed by Kaewkohkiat et al. (2017). Staggered rib configuration is applicable for the thermal systems needing periodical flow conditions as in the leading study discussed by Patankar et al. (1977). Consecutive studies for the staggered arrangement of the rectangular ribs have been done about convective heat transfer (Webb and Ramadhyani, 1985, Mayle, 1991, Liu and Wang, 2011, Wongcharee et al., 2011, Desrues et al., 2012, Xie et al., 2013, Marocco and Franco, 2017). In comparison studies done by Promvonge and Thianpong (2008), Skullong et al. (2015), Vanaki and Mohammed (2015), Yang et al. (2017); the staggered and symmetrical formations have been given together for the same rib design.

Different channels having both various rib heights and rib spacings have been considered for the comparison at Re = 10000. The contour graphics of heat transfer and flow characteristics were occasionally encountered in the past studies. For this reason, the graphics for temperature (T) contours, pressure (P) distributions, streamwise velocity components (u) and streamline patterns (Ψ) have been presented for understanding the problem. The aim of the study is to obtain the ducts having acceptable thermal performance factor values by taking Nusselt numbers and pressure coefficients into account depending on the graphics for thermal and hydraulic characteristics.

COMPUTATIONAL STUDY

The rectangular ribs have been mounted on the opposite plates of the horizontal duct for the staggered arrangement. Heat transfer augmentation due to the ribs has been examined for two dimensional analyses by employing k-ω SST model. One of the ribbed channels was indicated in Fig. 1 as an example.

The distance between the plates, H, is taken as 0.05 m. All dimensions in the study have been given in the non-dimensional form, L' = L/H = 20, as dividing by the channel height for its length. The constant rib width is w' = w/H = 0.1 as shown. The range for the rib height values is $0.1 \leq h' = h/H \leq 0.3$ while the spacing between two successive ribs is from S' = S/H = 0.5 to 1. What is more, a rib of any wall has been centered in compliance with the ones on the opposite wall. The ribs were placed after L' = 10 for the effect of fully developed flow (Cengel and Cimbala, 2006). Ten different models have been used by taking the aforementioned dimensions into consideration.

Thermal and hydraulic characteristics of the parallel plates have been discussed at $Re = U_\infty D_H / \nu = 10000$ for constant thermophysical properties. Computational Fluid Dynamics (CFD) is widely used for the engineering applications including problems of fluid mechanics, heat transfer and thermodynamics.

The flow domains for ten models have been utilized for the numerical analyses. For the following pace, the proper grid system is constituted by considering the reference parameters. The boundary conditions for the flow field have been defined as represented in Fig. 2. Uniform velocity inlet for the fluid at 300 K and pressure outlet were determined. No-slip boundary condition has been defined for the plates which are kept at 400 K as can be seen.

Generation of the grid structure depends on various components and parameters. Accordingly, a corre-

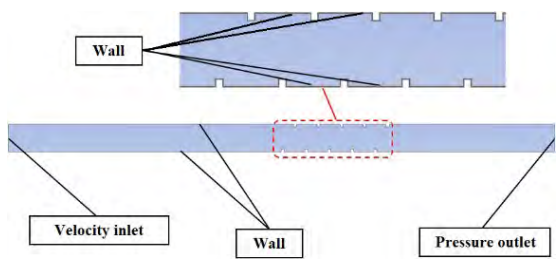

Figure 2. Boundary conditions

Table 1. Nusselt numbers attained from different turbulence models (Goktepeli et al., 2020)

Turbulence model	*Nu*
k-ε Realizable	*97.63*
k-ε Re-Normalisation Group (RNG)	*115.37*
k-ω Shear Stress Transport (SST)	*86.43*
k-ω Standard	*87.55*

lation of Eq. 1 has been utilized for the result validation in the smooth duct (Matsubara et al., 2016). Therefore, the numerical solution has to have no dependence of the grid system.

$$Nu = 0.021 Pr^{0.5} Re^{0.8} \quad (1)$$

The result of the correlation for Nusselt number (Nu = h D_H / k) gives the value of Nu = 84.19 for Reynolds number of the present study. The obtained value has been taken as reference for the smooth duct. The numerical results of various turbulence models at Re = 10000 have been compared with that of the aforementioned correlation (Goktepeli et al., 2020). The results from the independence test of turbulence models have been indicated in Table 1. The closest result to that of the reference correlation has been attained via k-ω Shear Stress Transport (SST) turbulence model.

Table 2. Nusselt numbers obtained for different grid numbers via k-ω SST turbulence model (Goktepeli et al., 2020)

Grid number	*Nu*
3 x 10⁵	*87.01*
4.3 x 10⁵	*86.46*
6.6 x 10⁵	*86.43*
8.6 x 10⁵	*86.52*
1.16 x 10⁶	*86.53*

Nusselt numbers have been obtained by employing k-ω SST turbulence model as shown in Table 2 for the numerical analyses with different grid numbers (Goktepeli et al., 2020). Although the numerical results were approximate for the considered grid numbers, the nearest result has been provided by using 6.6 x 10^5 elements based on that of the correlation.

Figure 3. The meshed model

The values for mesh quality are agreeable with the ones of the proposed ranges (Anonymous, 2009). Thinner grid elements have been intensified in the vicinity of the ribbed section to consider boundary layer. Total thickness inflation for the first ten layers and edge sizing has been implemented. A meshed flow domain including the detailed views of Fig. 3 was presented.

Once both appropriate grid structure and turbulence model were ascertained, all of the numerical simulations were conducted based on the results of the independence studies. Continuity and momentum equations have been solved. Reynolds-Averaged Navier-Stokes (RANS) equations are attained with the time-averaged versions of the aforementioned equations. For the incompressible flow, the continuity and the momentum equations were seen in Eqs. (2) and (3), respectively (Anonymous, 2009):

$$\frac{\partial \overline{u}_i}{\partial x_i} = 0 \quad (2)$$

$$\frac{\partial \overline{u}_i}{\partial t} + \frac{\partial \left(\overline{u}_i \overline{u}_j \right)}{\partial x_j} = -\frac{1}{\rho} \frac{\partial \overline{p}}{\partial x_i} - \frac{\partial \tau_{ij}}{\partial x_j} + \frac{\partial}{\partial x_j} \left(\nu \frac{\partial \overline{u}_i}{\partial x_j} \right) \quad (3)$$

Energy equation, also in Eq. (4), is solved for heat transfer cases (Anonymous, 2009):

$$\frac{\partial}{\partial t}(\rho E) + \frac{\partial}{\partial x_i}\left[u_i(\rho E + p)\right] = \frac{\partial}{\partial x_j}\left[\left(k + \frac{C_p \mu_t}{\mathrm{Pr}_t}\right)\frac{\partial T}{\partial x_j} + u_i\left(\tau_{ij}\right)_{eff}\right] + S_h \quad (4)$$

The terms are turbulent stresses included in the solution via turbulence modeling where Eqs. (5) and (6) are used (Anonymous, 2009):

$$\frac{\partial}{\partial t}(\rho k) + \frac{\partial}{\partial x_i}(\rho k u_i) = \frac{\partial}{\partial x_j}\left[\Gamma_k \frac{\partial k}{\partial x_j}\right] + \tilde{G}_k - Y_k + S_k \quad (5)$$

$$\frac{\partial}{\partial t}(\rho \omega) + \frac{\partial}{\partial x_i}(\rho \omega u_i) = \frac{\partial}{\partial x_j}\left[\Gamma_\omega \frac{\partial \omega}{\partial x_j}\right] + G_\omega - Y_\omega + D_\omega + S_\omega \quad (6)$$

Based on the equations, k and ω are turbulent kinetic energy and specific dissipation rate, respectively. What is more, $\tilde{G}_k$ is the generation of the turbulent kinetic energy resulting from the mean velocity gradients and the specific dissipation rate generation is given as G_ω. The effective diffusivity values for k and ω are Γ_k and Γ_ω, respectively. Furthermore, Y_k and Y_ω are dissipation of k and ω as a

result of turbulence. The cross-diffusion term is D_ω while S_k and S_ω are the user-defined source terms (Goktepeli et al., 2020).

For the simulations, the maximum number of iterations per time step was twenty for the time step of 0.0068 s. However, the iterations terminate for the analysis when the residuals of the equations are balanced to 10^{-8}. The dimensionless wall distance was $y^+ = u^* y/\nu \cong 1$ (Goktepeli et al., 2020).

RESULTS AND DISCUSSION

Heat transfer and fluid flow characteristics have been presented for Re = 10000 in Figs. 4–13 and Table 3 after conducting the numerical analyses. These aforementioned results have been discussed for relevant subheadings of temperature (T) contours, pressure (P) distributions, streamwise velocity components (u), streamline patterns (Ψ), normalized mean Nusselt numbers ($\overline{Nu}$) together with local Nusselt numbers (Nu), local pressure coefficients (C_p) and thermal performance factor (η) values. The top-down arrangement for the figures of temperature (T) contours, pressure (P) distributions, streamwise velocity components (u), streamline patterns (Ψ) is smooth channel, the ribbed channel with S' = 0.5 and h' = 0.1, the ribbed channel with S' = 0.5 and h' = 0.2, the ribbed channel with S' = 0.5 and h' = 0.3, the ribbed channel with S' = 0.75 and h' = 0.1, the ribbed channel with S' = 0.75 and h' = 0.2, the ribbed channel with S' = 0.75 and h' = 0.3, the ribbed channel with S' = 1 and h' = 0.1, the ribbed channel with S' = 1 and h' = 0.2 and the ribbed channel with S' = 1 and h' = 0.3.

Temperature Contours

Time-averaged results of temperature <T> distributions have been given based on the numerical analyses in Fig. 4. Fluid at 300 K has been supposed to enter the horizontal parallel plates of duct maintained at 400 K. The maximum and the minimum values of temperature contours were as 400 K and 300 K, respectively for the investigated problem. Due to the fact that the temperature distributions have been differently observed in terms of various types of the ducts, changes of the heat transfer characteristics are obviously sighted. Nonetheless, the ribbed ducts are more dominant over the smooth plates from the point of heat transfer. In the general sense, this situation is explained by temperature alterations seen in the vicinity of to the wall. Due to this reason, the channels with the ribs are very effective in terms of heat transfer when compared to the smooth duct. As a result of the interaction between fluid and solid regions, flow separation has been seen because of the first rib at the upstream. Another explanation on this case is the breaking down of both hydrodynamic and thermal boundary layers with

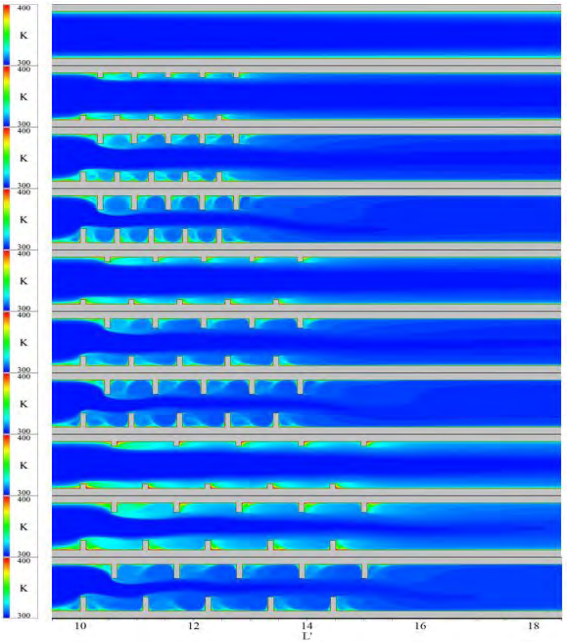

Figure 4. Temperature (T) contours at Re = 10000

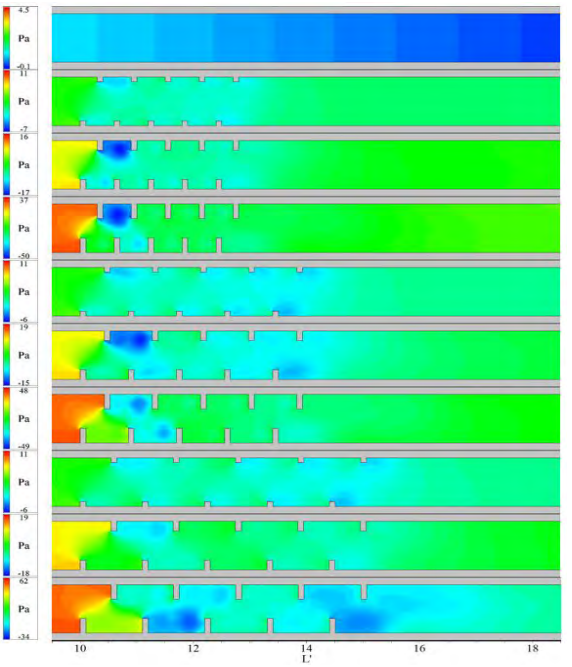

Figure 5. Pressure (P) distributions at Re = 10000

the effect of the ribs. Instantaneous changes in temperature values have been seen due to complex flow structure in these zones. Heat transfer has been substantially augmented as explained. It has been beheld for all cases including the ribbed channels. Increase of fluid temperature along the centerline has been occurred by virtue of the reduction of cross-section triggering the flow mixing. What is more, surface area for heat transfer has been become wider by the ribs. It is known that this circumstance positively affects heat transfer enhancement. Even

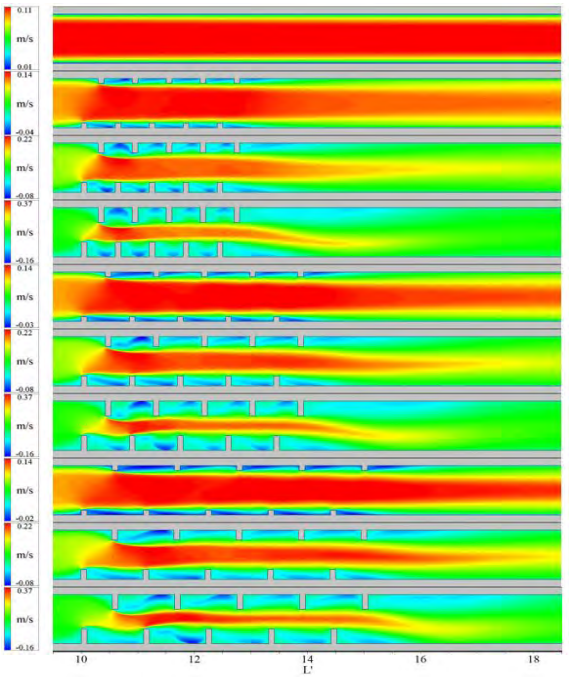

Figure 6. Streamwise velocity components (u) at Re = 10000

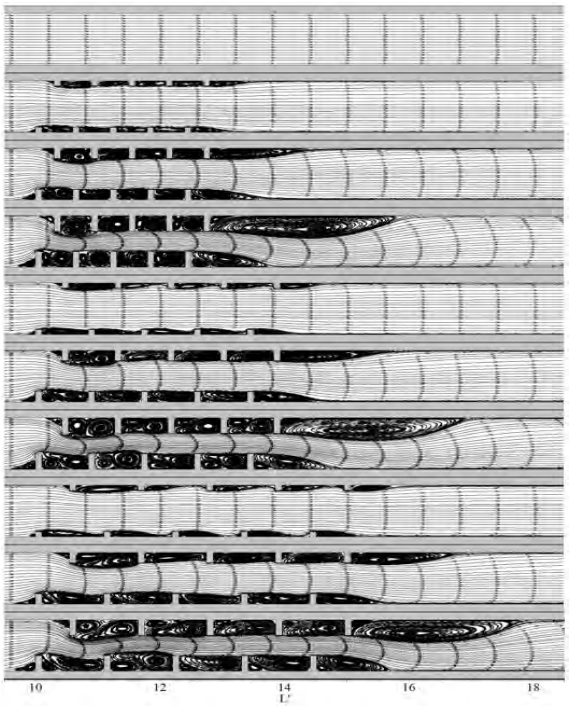

Figure 7. Streamline patterns (Ψ) at Re = 10000

though placing the longer rib to enhance the effect of flow separation, the rib height is limitative in terms of the margin of both plates. Another constraint to be born in mind is pressure drop for the design of the heat transfer system. In the present case, changing the distance between two successive ribs has been considered to augment the heat transfer. Based on the present results, heat transfer has been increased with the increment of the margin between the ribs owing to the fact that fluid flow simply steps in the gap to generate recirculation. It has been observed with temperature distributions presented in Fig. 4. Moreover, the contact zones between fluid and solid regions have been enlarged by ascending the margin thereafter the flow reattachment. For instance, it is difficult for fluid flow to move in the region covered by two ribs due to narrower spacing. It can be observed in Fig. 4 that only one circulation zone occurs when the ribs are closer enough to each other. While the distance is increased, two circulation zones can be observed and heat transfer coefficient is increased with this manner. As seen in Fig. 7, recirculating regions have also been observed via streamline patterns.

Pressure Distributions

Time-averaged results for pressure distributions have been indicated in Fig. 5. Pressure drop for the smooth duct was less when compared to the ribbed model as anticipated. There is gradual drop for pressure values through the smooth channel. Furthermore, pressure values have been increased by mounting the ribs on the plates. However, the effect of the rib spacing on pressure values is less than that of other parameters. For this reason, there is strong decrease in pressure values for all cases with the ribbed ducts. The section that rapid decrement of pressure values took place is broadly the wake region of the first rib on the upper plate. Especially, this is the minimum pressure region for S' = 0.5. When the rib spacing has been increased step by step, the secondary minimum pressure regions have been seen in the wakes of different ribs based on the position. After the second ribs, the increment of pressure values has been observed and the values approached to the average ones of the legend bar. Accordingly, transitional recovery for pressure values has been obtained due to the flow rate decrement resulting from the second ribs. The recovery in pressure values was earlier for S' = 0.5 and its trend was effectual up to the end of the ribbed section. However, pressure values decreased around the last rib of the lower plate. After passing the ribbed zone, average pressure values were dominant.

Streamwise Velocity Components

Time-averaged results of streamwise velocity components <u> have been presented in Fig. 6. The maximum values for the streamwise velocity components have been attained at the outside of boundary layer for the smooth duct. There is decrement in the velocity values for the regions affected by the boundary layer owing to no-slip condition on the plate. Rotational flow has not been obtained in the absence of the ribs. As can be seen from the graphics, the channel cross-section is downsized by the virtue of the ribs mounted on the

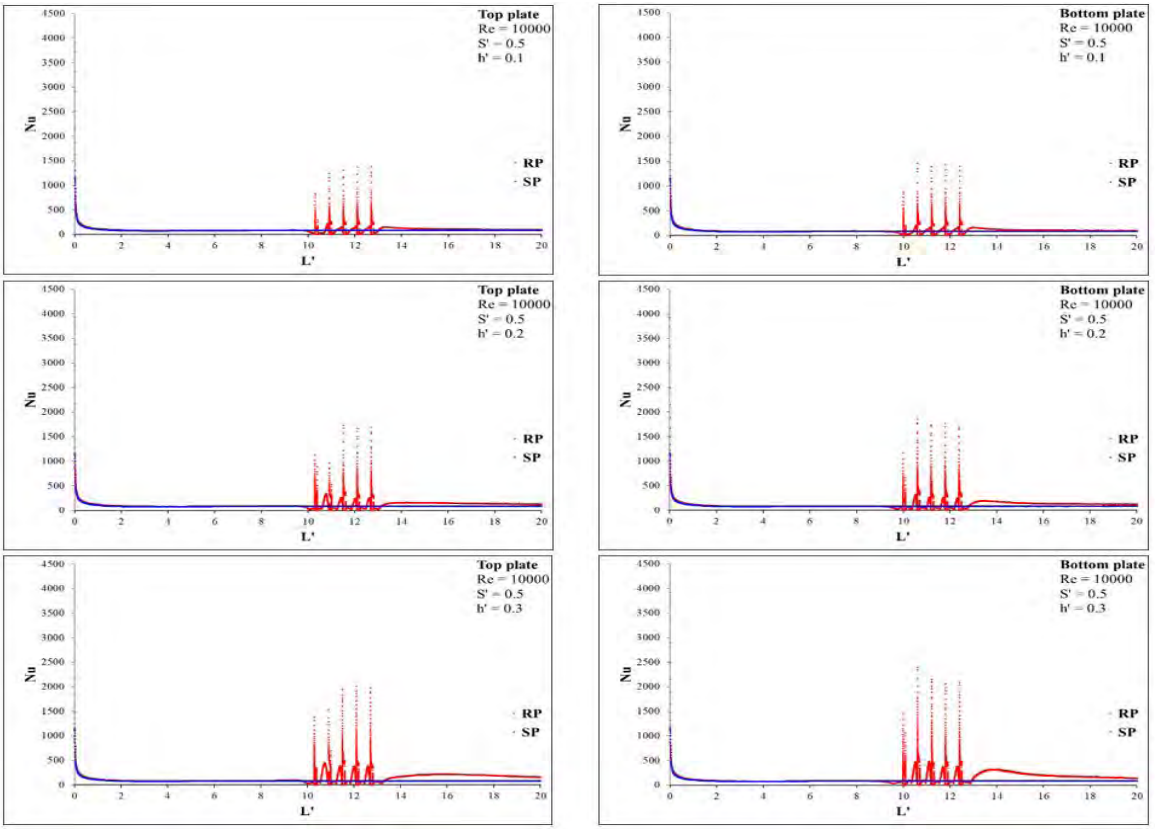

Figure 8. Local Nusselt numbers (Nu) through the channels for varying rib heights of S' = 0.5 at Re = 10000

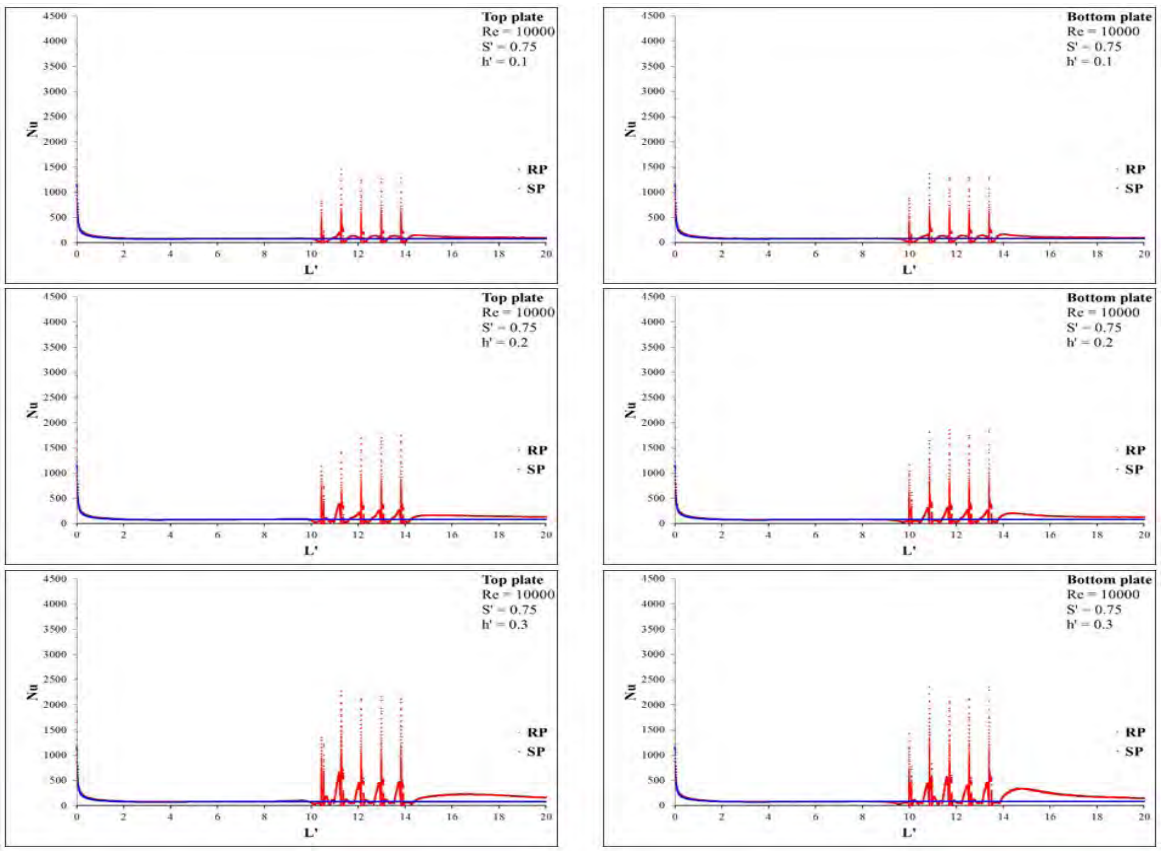

Figure 9. Local Nusselt numbers (Nu) through the channels for varying rib heights of S' = 0.75 at Re = 10000

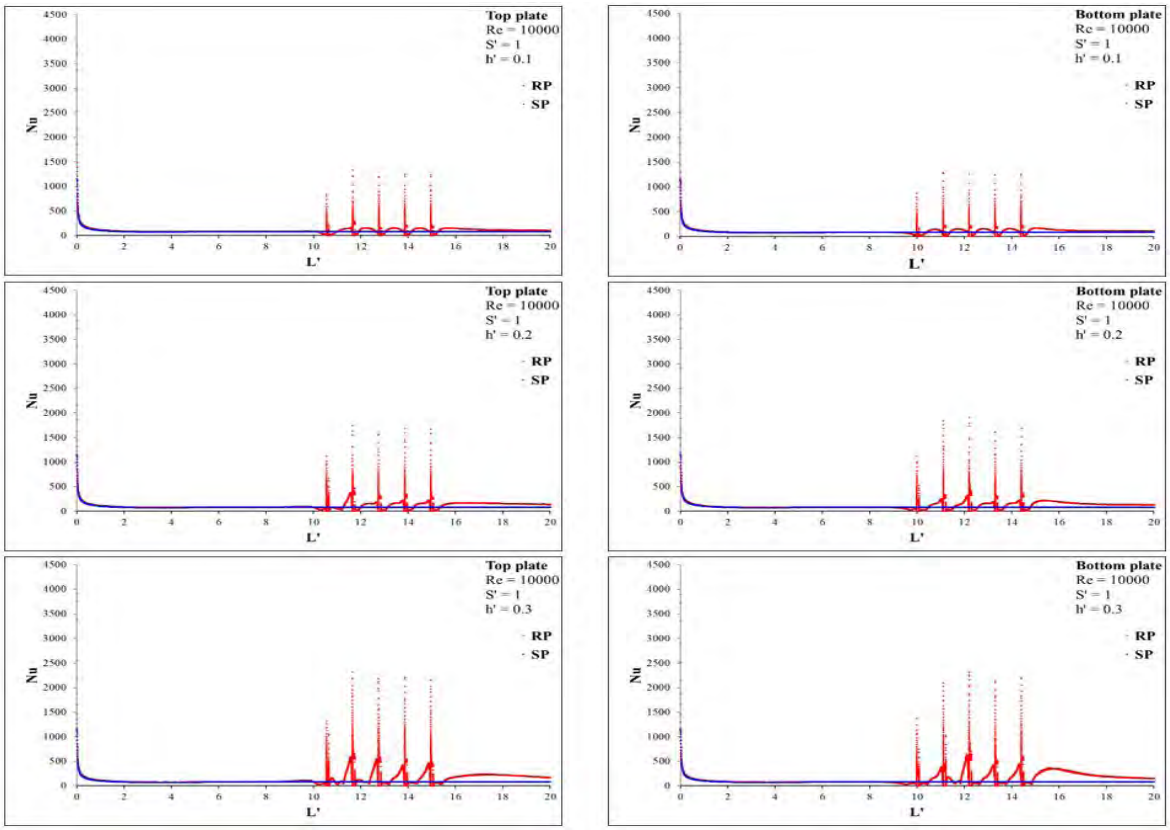

Figure 10. Local Nusselt numbers (Nu) through the channels for varying rib heights of S' = 1 at Re = 10000

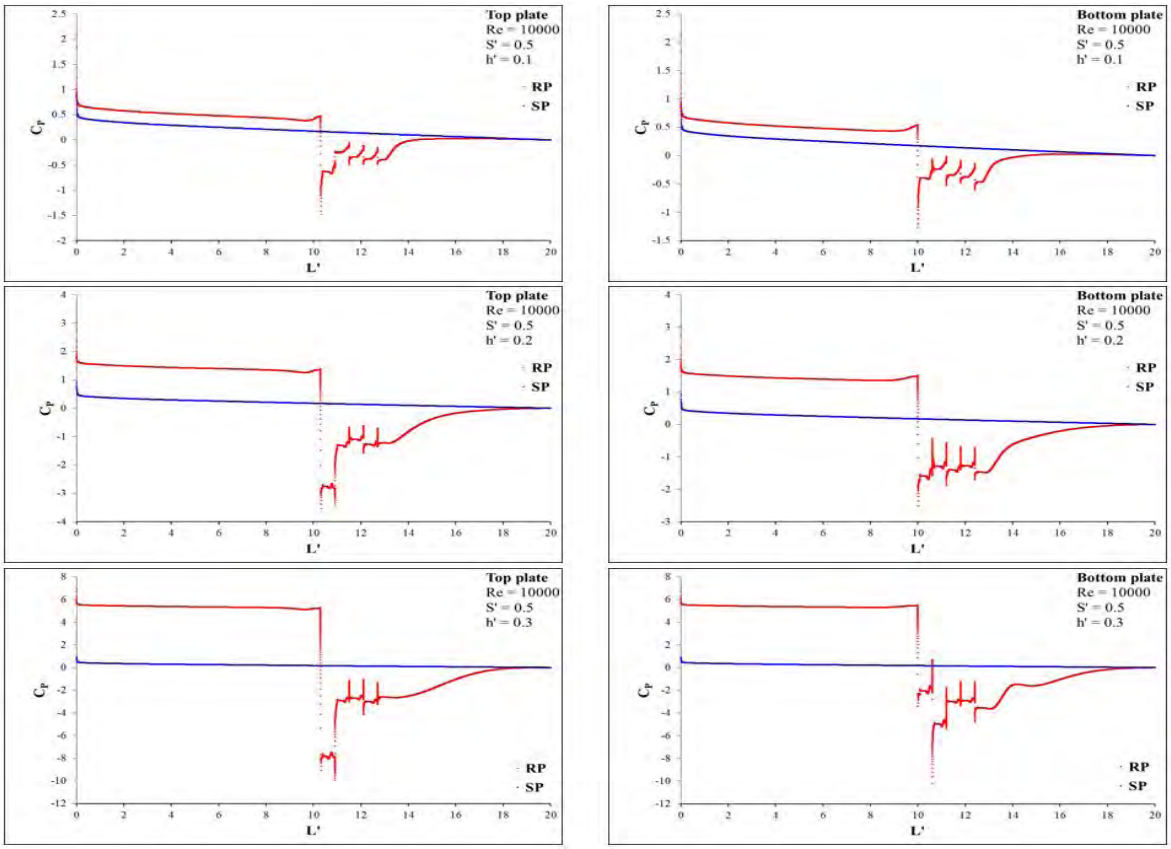

Figure 11. Local pressure coefficients (C_p) through the channels for varying rib heights of S' = 0.5 at Re=10000

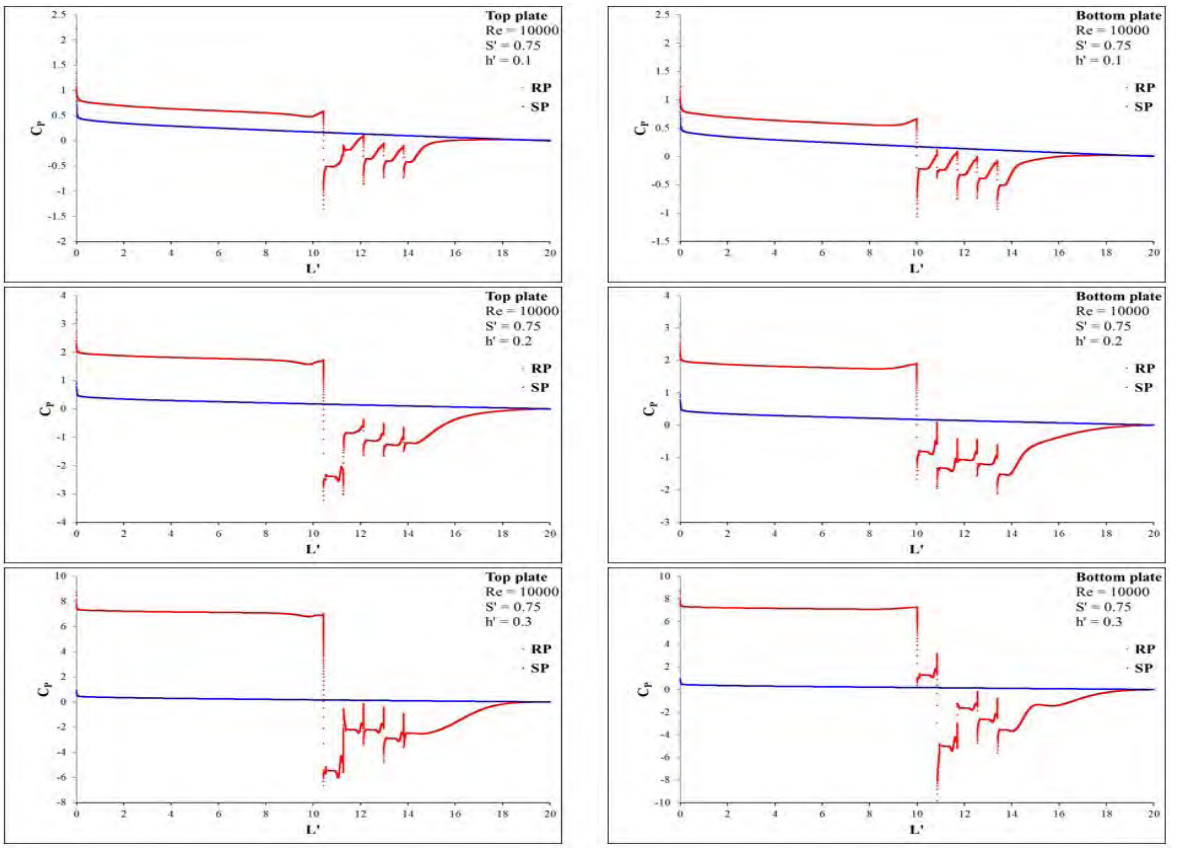

Figure 12. Local pressure coefficients (C_p) through the channels for varying rib heights of S' = 0.75 at Re = 10000

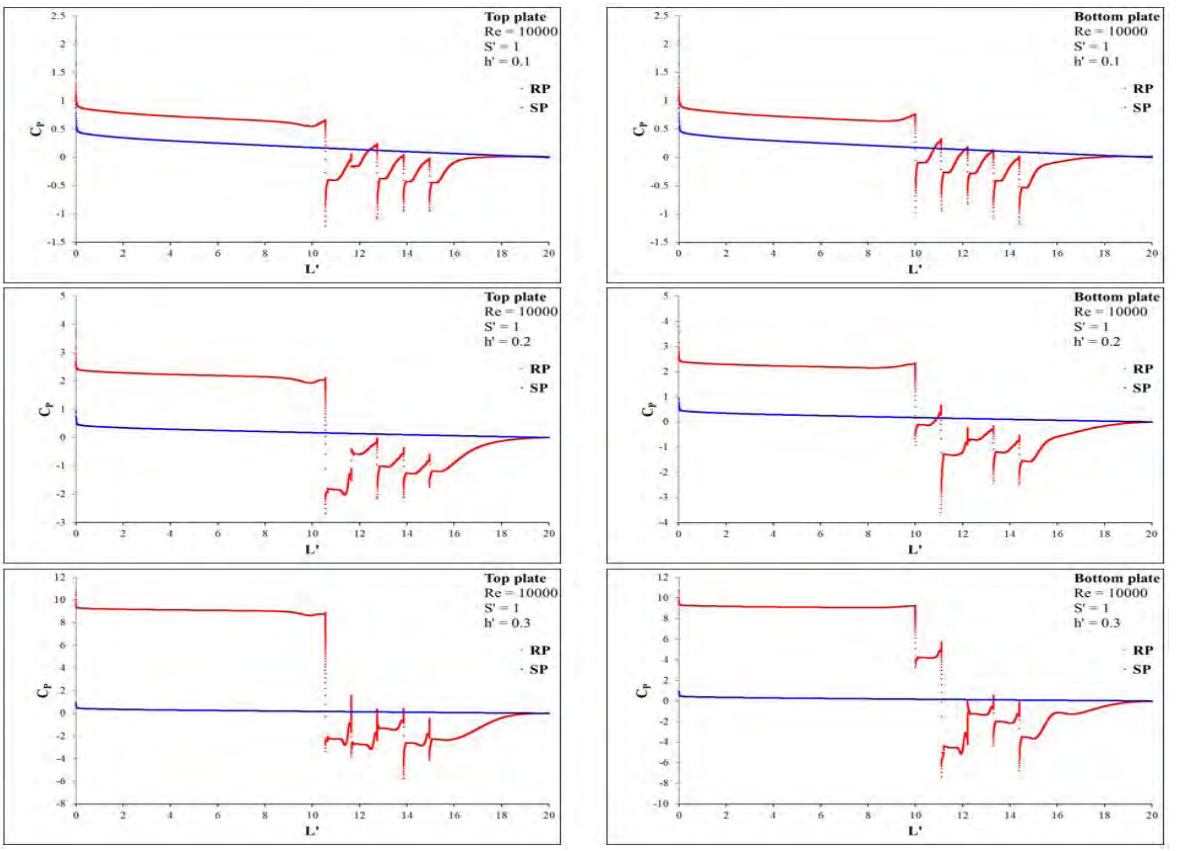

Figure 13. Local pressure coefficients (C_p) through the channels for varying rib heights of S' = 1 at Re = 10000

walls. Due to this reason, negative velocity components have been attained in the ribbed region. Thus, there is increase for the velocity values observed because of the decrement of the cross-sectional area in the duct. It is the result of the flow separation triggered by the first rib on both upper and lower walls. Asymmetrical flow structure has been obtained as a result of staggered arrangement. In case of the forward-facing step flow where after the flow separates from the walls, it reattaches to the upstream corner of the rib and it is again separated from that point (Goktepeli et al., 2021). In the regions where flow separated, the rotational flows have been seen at the upstream of the rib. This is the forward-facing step flow at the upstream of the rib, the cavity flow between the ribs and the backward-facing step flow at the downstream of the rib (Yemenici and Umur, 2016). When it comes to cavity flow, rotational flow that is more energetic between the first two ribs comparatively has lost its effect for the gap between the other ones. In terms of the most cases, the regions for the maximum velocity values obtained were formed by the first two ribs and the upper side of the centerline. Nevertheless, there is not much alteration for the velocity values while the spacing between the ribs is enlarged. The region of maximum streamwise velocity values observed was between the other ribs with respect to the increase of rib spacing.

Streamline Patterns

Time-averaged results of streamline patterns <Ψ> have been exhibited in Fig. 7. Uniform flow structure has been obtained without the additional elements diminishing the flow for the smooth channel. Chaotic flow structure has been considerably obtained in the existence of the ribs mounted on the walls of the duct. However, the width between the ribs has effect on complexness degree of flow field.

Rotational flow has been seen between first ribs in a row due to flow separation considerably affected by them. Since the leading element to distort the flow was the first rib, larger vortices have been attained in the wake of the first one for both plates. The separated flow produces a lower pressure region at the downstream of the first ribs as in Fig. 7. Periodical flow has been seen because of the rib arrangement and the intensity of eddies was less than the first ones. What is more, the required distance for the flow recovery does not vary with the rib spacing.

Local And Mean Nusselt Number Values

Nusselt number values through both ribbed and smooth channels have been given for the comparison in Figs 8-10. On the graphics, the abbreviations of "RP" and "SP" are for the ribbed and smooth channels, respectively. Nusselt number values have been presented for the overall duct length. Moreover, in Table 3, Nusselt numbers for the ribbed channels have been compared by using the values of the smooth plate.

As given in Figs. 8-10, Nusselt number values of both smooth and ribbed plates coincided for $0 \le L' \le 9$. The values of Nusselt numbers tend to increase suddenly after the first rib. The value around the first rib is relatively lower than those of the rest of the ribs. Nonetheless, the values have decreased between the successive ribs. The peak values due to each rib have increasing effect on the mean Nusselt number. Therefore, heat transfer has been augmented. After passing the fifth rib, the values of Nusselt numbers have sharply dropped and re-increased. Flow recovery has been observed in the vicinity of the outlet. This recovery delays owing to increasing all parameters. As clearly seen for all of the cases, the asymmetrical distributions have been observed because of the staggered arrangement. The minimum values have been seen at the reattachment points between the ribs.

Moreover, the mean Nusselt numbers of the ribbed ducts have also been compared with that of smooth channel in terms of normalized values. Heat transfer has been enhanced by mounting the ribs as can be seen in Table 3 where mean Nusselt numbers for the ribbed ducts against the value of the smooth plate have been given. Heat transfer increment varies based on the effect of the geometrical dimensions related with the ribs such as height, spacing etc. Nusselt numbers have been attained at higher values for increasing rib height and the highest increment has been observed when it is from h' = 0.2 to h' = 0.3, respectively. The relative change for the Nusselt number values are % 25 for S' = 0.5, % 28.3 for S' = 0.75 and % 29.4 for S' = 1 when the rib heights are increased from h' = 0.2 to h' = 0.3. In this study, another parameter enhancing the convective heat transfer is the rib spacing in terms of Nusselt number values. The spacing effect on Nusselt number values is clearly seen from S' = 0.5 to S' = 0.75 as can be seen in the chart. The relative changes for the Nusselt numbers are % 2.1 for h' = 0.1, % 2.3 for h' = 0.2 and % 4.6 for h' = 0.3 when the rib spacing values

Table 3. Normalization of mean Nusselt numbers ($\overline{Nu}$) at Re = 10000

Ribbed channels	*Re=10000*
S' = 0.5 and h' = 0.1	*1.198*
S' = 0.5 and h' = 0.2	*1.414*
S' = 0.5 and h' = 0.3	*1.775*
S' = 0.75 and h' = 0.1	*1.223*
S' = 0.75 and h' = 0.2	*1.446*
S' = 0.75 and h' = 0.3	*1.856*
S' = 1 and h' = 0.1	*1.229*
S' = 1 and h' = 0.2	*1.443*
S' = 1 and h' = 0.3	*1.867*

are increased from S' = 0.5 to S' = 0.75, respectively. However, these changes are relatively less than those of the rib height. In other words, the effect of the rib height is much more than that of the rib spacing in terms of Nusselt number values. The results show that the highest increase of Nusselt number has been obtained for the maximum rib height of h' = 0.3 and the maximum rib spacing of S' = 1 based on that of the smooth plate.

Local Pressure Coefficients

Local distributions of pressure coefficients have been given as presented in Figs. 11-13. Even though there is no rib mounted for $0 \leq L' \leq 9$, noteworthy difference between the pressure coefficients of both ribbed and smooth plates has been observed. Maximum pressure coefficient was at the duct inlet and the values started to decrease up to the duct outlet. The drop is nearly similar for both plates with $0 \leq L' \leq 9$. After the first rib, the local values have suddenly decreased. The initial point of the recuperation region for the pressure coefficients can be postponed with the increment of the rib height and the rib spacing. Enormous influence that increases the pressure coefficients is arisen from the increase of the rib height. It can be induced that the effect of the rib spacing on the pressure coefficients is relatively less.

Values For Thermal Performance Factor

Although the ratio of Nusselt numbers indicates that how much heat transfer enhancement is obtained, it is not enough for the system design since it does not include any pressure loss term that has to be considered for the envisagement. For this reason, the values for thermal performance factor (η) of the ribbed plates have been calculated. Here, $\eta = (Nu/Nu_0)(f/f_0)^{-1/3}$ states the optimum value with respect to the heat transfer augmentation over pressure loss. If the thermal performance factor is $\eta \geq 1$, it means that the ribbed duct can be proposed for increment of heat transfer as pressure drop for the system is tolerated. In the present study, h' = 0.1 with S' = 0.5 at Re = 10000 having η = 1.049 and h' = 0.1 with S' = 0.75 at Re = 10000 having η = 1.019 are the potential ribbed channels for the recommandation in terms of heat transfer enhancement.

CONCLUSION

Heat transfer and fluid flow characteristics for the plates have been considered via the staggered ribs at Re = 10000, in the present study. By keeping the rib width of w' = 0.1 constant, the rib height and the rib spacing have been respectively changed as $0.1 \leq h' \leq 0.3$ and $0.5 \leq S' \leq 1$. The results have been summarized as:

- More chaotic flow structure has been observed by using the ribs for the staggered arrangement. Therefore, heat transfer has been augmented as a result of increasing heat transfer coefficient due to the flow mixing.
- Increasing the height of the rib and the spacing between the ribs separately, has an increasing effect on Nusselt number. Here, the rib height is more dominant than the rib spacing in terms of heat transfer enhancement.
- Pressure drop has been observed owing to the increment of the rib height and the spacing between the ribs. However, as in Nusselt number, the rib height is more effective than the rib spacing when it comes to pressure loss.
- Since increasing the rib height and the rib spacing increases both heat transfer by convection and pressure drop, performance criterion has to be calculated for the optimization. To sum up, h' = 0.1 with S' = 0.5 having η = 1.049 and h' = 0.1 with S' = 0.75 having η = 1.019 have been advised since thermal performance factor values are $\eta \geq 1$, in the present study at Re = 10000.

ACKNOWLEDGMENTS

This study has been supported by Academic Staff Training Program (OYP) with the project number of 2018-OYP-046.

NOMENCLATURE

CFD	:	Computational Fluid Dynamics
C_p	:	Pressure coefficient
D_H	:	Hydraulic diameter [m]
D_ω	:	Cross-diffusion term
E	:	Energy [J]
f	:	Friction factor
G_k	:	Generation of turbulence kinetic energy
G_ω	:	Generation of dissipation rate
h	:	Height, rib height [m]
H	:	Distance between the plates [m]
k	:	Thermal conductivity coefficient [W/mK], turbulence kinetic energy [m2/s2]
L	:	Length [m]
Nu	:	Nusselt number
P	:	Pressure [Pa]
RANS	:	Reynolds-Averaged Navier-Stokes
Re	:	Reynolds number
RNG	:	Re-Normalization Group
RP	:	Ribbed plate
S	:	Rib spacing [m], user-defined source term
SP	:	Smooth plate
SST	:	Shear Stress Transport
t	:	Time [s]
T	:	Temperature [K]
u	:	Streamwise velocity component [m/s]
U_∞	:	Free-stream velocity [m/s]
w	:	Width, rib width [m]
y^+	:	Dimensionless wall distance
Y	:	Dissipation due to turbulence
Γ	:	Effective diffusivity
η	:	Thermal performance factor

μ	:	Dynamic viscosity [Pas]
ν	:	Kinematic viscosity [m²/s]
ρ	:	Density [kg/m³]
τ	:	Stress [Pa]
Ψ	:	Streamline pattern
ω	:	Specific dissipation rate

Supercript

'	:	Dimensionless

Subscript

0	:	Smooth plate

REFERENCES

1. Sundén B. Convective heat transfer and fluid flow physics in some ribbed ducts using liquid crystal thermography and PIV measuring techniques. Heat and Mass Transfer 47 (2011) 899-910.
2. Kashyap U, Das K, Debnath BK. Effect of surface modification of a rectangular vortex generator on heat transfer rate from a surface to fluid. International Journal of Thermal Sciences 127 (2018) 61-78.
3. Yang YT, Chen PJ. Numerical optimization of turbulent flow and heat transfer characteristics in a ribbed channel. Heat Transfer Engineering 36 (2015) 290-302.
4. Alfarawi S, Abdel-Moneim S, Bodalal A. Experimental investigations of heat transfer enhancement from rectangular duct roughened by hybrid ribs. International Journal of Thermal Sciences 118 (2017) 123-138.
5. Tiggelbeck S, Mitra NK, Fiebig M. Experimental investigations of heat transfer enhancement and flow losses in a channel with double rows of longitudinal vortex generators. International Journal of Heat and Mass Transfer 36 (1993) 2327-2337.
6. Abdollahi A, Shams M. Optimization of shape and angle of attack of winglet vortex generator in a rectangular channel for heat transfer enhancement. Applied Thermal Engineering 81 (2015) 376-387.
7. Kilicaslan I, Sarac HI. Enhancement of heat transfer in compact heat exchanger by different type of rib with holographic interferometry. Experimental Thermal and Fluid Science 17 (1998) 339-346.
8. Sripattanapipat S, Promvonge P. Numerical analysis of laminar heat transfer in a channel with diamond-shaped baffles. International Communications in Heat and Mass Transfer 36 (2009) 32-38.
9. Manca O, Nardini S, Ricci D. Numerical analysis of water forced convection in channels with differently shaped transverse ribs. Journal of Applied Mathematics 2011 (2011) 323485.
10. Wongcharee K, Changcharoen W, Eiamsa-Ard S. Numerical investigation of flow friction and heat transfer in a channel with various shaped ribs mounted on two opposite ribbed walls. International Journal of Chemical Reactor Engineering 9 (2011).
11. Ahmed M, Yusoff M, Shuaib N. Effects of geometrical parameters on the flow and heat transfer characteristics in trapezoidal-corrugated channel using nanofluid. International Communications in Heat and Mass Transfer 42 (2013) 69-74.
12. Aslan E, Taymaz I, Islamoglu Y. Finite volume simulation for convective heat transfer in wavy channels. Heat and Mass Transfer 52 (2016) 483-497.
13. Moon MA, Park MJ, Kim KY. Evaluation of heat transfer performances of various rib shapes. International Journal of Heat and Mass Transfer 71 (2014) 275-284.
14. Kaewkohkiat Y, Promvonge P, Eiamsa-Ard S. Turbulent periodic flow and heat transfer in a rectangular channel with detached V-baffles. Journal of Engineering Thermophysics 26 (2017) 542-552.
15. Patankar S, Liu C, Sparrow E. Fully developed flow and heat transfer in ducts having streamwise-periodic variations of cross-sectional area. Journal of Heat Transfer 99 (1977) 180-186.
16. Webb B, Ramadhyani S. Conjugate heat transfer in a channel with staggered ribs. International Journal of Heat and Mass Transfer 28 (1985) 1679-1687.
17. Mayle RE. Pressure loss and heat transfer in channels roughened on two opposed walls. Journal of Turbomachinery 113 (1991) 60-66.
18. Liu H, Wang J. Numerical investigation on synthetical performances of fluid flow and heat transfer of semiattached rib-channels. International Journal of Heat and Mass Transfer 54 (2011) 575-583.
19. Desrues T, Marty P, Fourmigué J. Numerical prediction of heat transfer and pressure drop in three-dimensional channels with alternated opposed ribs. Applied Thermal Engineering 45 (2012) 52-63.
20. Xie G, Li S, Zhang W, Sunden B. Computational Fluid Dynamics modeling flow field and side-wall heat transfer in rectangular rib-roughened passages. Journal of Energy Resources Technology 135 (2013) 042001.
21. Marocco L, Franco A. Direct Numerical Simulation and RANS comparison of turbulent convective heat transfer in a staggered ribbed channel with high blockage. Journal of Heat Transfer 139 (2017) 021701.
22. Promvonge P, Thianpong C. Thermal performance assessment of turbulent channel flows over different shaped ribs. International Communications in Heat and Mass Transfer 35 (2008) 1327-1334.
23. Skullong S, Thianpong C, Promvonge P. Effects of rib size and arrangement on forced convective heat transfer in a solar air heater channel. Heat and Mass Transfer 51 (2015) 1475-1485.
24. Vanaki SM, Mohammed H. Numerical study of nanofluid forced convection flow in channels using different shaped transverse ribs. International Communications in Heat and Mass Transfer 67 (2015) 176-188.
25. Yang W, Xue S, He Y, Li W. Experimental study on the heat transfer characteristics of high blockage ribs channel. Experimental Thermal and Fluid Science 83 (2017) 248-259.
26. Cengel Y, Cimbala JM. Fluid mechanics fundamentals and applications. International Edition, McGraw Hill Publication, 185201, 2006.
27. Goktepeli I, Atmaca U, Cakan A. Investigation of heat transfer augmentation between the ribbed plates via Taguchi approach and Computational Fluid Dynamics. Journal of Thermal Science 29 (2020) 647-666.
28. Matsubara K, Ohta H, Miura T. Entrance region heat transfer in a channel with a ribbed wall. Journal of Heat Transfer 138 (2016) 122001.
29. Anonymous. ANSYS-Fluent 12.0 Theory Guide. ANSYS Inc (2009).
30. Goktepeli I, Atmaca U, Yagmur S. Visualization of flow characteristics between the ribbed plates via Particle Image Velocimetry. Thermal Science 25 (2021) 171-179.
31. Yemenici O, Umur H. Experimental aspects of heat transfer enhancement over various flow surfaces. Heat Transfer Engineering 37 (2016) 435-442.

Hittite Journal of Science and Engineering, 2021, 8 (1) 19–26
ISSN NUMBER: 2148–4171
DOI: 10.17350/HJSE19030000208

Investigation of Tomato, Quince and Grapefruit Waste; Compositions and Functional Properties

Zeynep Aksit[1] **Huseyin Genccelep**[2]
[1]Erzincan Binali Yildirim University, Department of Food Engineering, Erzincan, Turkey
[2]Ondokuz Mayis University, Department of Food Engineering, Samsun, Turkey

ABSTRACT

The food industry constantly growing with increasing population and food diversity. In addition to production, the formation of food waste is also increasing. These wastes cause environmental pollution, economical problems and the loss of valuable chemical components. Tomato is used for tomato paste, sauce and other food production; especially the skin and seed part of tomato is waste. Grapefruit and quince have a significant amount of waste, especially in the beverage industry. The reuse of these wastes can reduce the exposure of solid waste, the environmental problem and the recovery of the bioactive components. In this study, some physicochemical, functional and thermal properties of quince, grapefruit and tomato waste were determined and their reuse potential was revealed. All three samples showed high hydration properties. According to the dietary fiber analysis, TDF of quince, grapefruit and tomato were 87.90%, 90.34%, and 63.76% respectively. DTG and TGA chromatograms were obtained for the thermal decomposition of the samples. Tomato waste signaled lycopene and its derivatives as distinct from the other samples in the FT-IR spectrum. Based on the results of the study; the use of these wastes in many food products as hydrocolloid, filler, fat replacer is possible, also cost reduction may be possible with the recovery of these samples.

Keywords: Food waste, Tomato, Quince, Grapefruit, Dietary fiber, DTG, FT-IR

Article History:
Received: 2020/09/18
Accepted: 2021/01/17
Online: 2021/03/31

***Correspondence to**: Zeynep Akşit*
zeynep.aksit@erzincan.edu.tr
Phone: +90 446 226 6666,
Fax: +90 446 266 6665.

INTRODUCTION

In food factories, large quantities of food wastes are produced as a result of processing. Food waste causes adverse environmental problems including food shortages, prevention of food availability and releasing greenhouse gases. Therefore, the use of wastes in the production of new products has great importance in terms of human health, environmental pollution and the national economy [1-3]. These wastes include bioactive compounds such as polyphenols and essential oils along with dietary fibers that can be returned as valuable products that provide economic benefits for the food, cosmetic and pharmaceutical industries. Because consumers prefer natural and fiber-rich supplements; they are very valuable products for the food industry [4]. Dietary fibers include cellulose, lignin, hemicellulose, pectic substances, gums and other carbohydrates [5]. The insoluble fraction of dietary fiber is associated with bowel regulation, whereas the soluble fraction is associated with lower cholesterol levels and absorption of intestinal glucose [6]. In recent years, the food industry has focused on waste product evaluation, both to prevent the loss of these valuable substances and to prevent environmental problems caused by these wastes.

Quince fruit is difficult to consume due to its low moisture content, strong acidity, woody flesh, high amount of stone cells and astringent taste due to lignum development [7]. The high amount of lignin in the fruits limits their use in the food industry. The tendency of the quince to rot and turn to brown is a limiting factor in the long-term storage of this fruit [8]. Many studies have shown that quince jam and quince by-products are a good and inexpensive source for phenolic acids, antioxidants, and flavonoids [9].

Citrus processing, unlike other fruits; causes a small amount of the product but a significant amount of by-products during processing. The orange juice industry uses approximately 50% of the fruit and the re-

maining 50% waste part consists of shells, seeds, and albedo [10, 11]. Citrus processing waste is a source of fiber, pectin, seed oil, essences, D-limonene, ethanol, ascorbic acid, soluble sugars, organic acids, amino acids, proteins, minerals, vitamins and flavonoids. They are generally used as a pectin source, animal feed, vinegar, molasses, fertilizer and citrus flour. However, apart from these limited uses, pulp waste is considered garbage and discarded [10, 11, 13].

Tomato products rich in phytochemicals and flavonoids, so it is named as functional food and tomato processing waste is called as secondary raw material [14, 15]. Tomato pulp; contains the skin, broken seeds and fruit flesh remaining from tomato juice extraction [16].

Within the scope of this study, the residual waste material from quince, grapefruit and tomato processing was obtained and the pulps were dried and ground. Various physical, chemical, and thermal analyses were performed to determine composition analysis and functional properties. The characteristics of these three different waste products were determined and their reuse potential was investigated. It is aimed to reduce environmental pollution, to recover valuable components, to produce cheap and natural additives and to increase an option for product diversity.

MATERIAL AND METHODS

Material

Quince fruit was purchased from local market in Gümüşhane, Turkey. Quince waste obtained similar to quince juice processing factory; quince fruit pressed in the fruit juicer, the remaining solid waste washed several times under the tap water to reduce the sugar content, then kept in a hot water at 60°C for 3 minutes to reduce enzymatic browning [17, 18] and dried at 40°C in the oven for 24 hours. Grapefruit fruit was purchased from a local market in Gümüşhane, Turkey. Grapefruit waste is obtained as follows; the orange part of the grapefruit peels (the flavedo layer) was peeled off and the rest of the fruit was pressed in the juicer and the pulp portion was collected in the flask, then dried in a 40°C oven for 24 hours. Tomato waste was purchased from Limkon Gıda Company (Adana, Turkey), the remaining part of the tomato paste production. Tomato waste was dried outdoor under the sun in Adana, at 38°C air temperature. All dried samples were milled and sieved through a 750 µ sieve and kept at 4°C in a dark bottle until analyses. Fig. 1. represents quince, grapefruit, and tomato waste samples.

Methods

The moisture content, ash, pH, crude protein, crude oil analyses were done as proximate analysis; water binding capacity (WBC), oil binding capacity (OBC), swelling capacity (SC) were done as hydration analyses. Water solubility index, dietary fiber analysis, thermogravimetric analyzes and FT-IR analyses of samples were also performed.

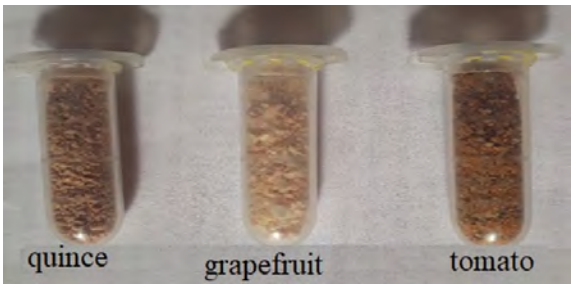

Figure 1. The image of the samples obtained.

pH and Proximate Analysis

The ground samples were diluted with distilled water (1/10; w/v) and the pH values were measured by immersing the pH meter (Hanna Instruments HI2211) probe.

The obtained by-products were analyzed for proximate composition. Moisture, protein, fat, and ash analysis was carried out according to the AOAC standards. Moisture content was determined by drying samples at 105±1°C till reaching constant weights [19], crude protein content was determined by the Kjeldahl method, a factor of 6.25 was used for conversion of nitrogen to crude protein [20], fat content analyzed [21], and ash analysis done with burning samples at 550°C till white-grey color obtained [22].

Water Binding Capacity (WBC)

In order to determine the WBC of samples; 1 g of powder sample (m_1) was placed in a centrifuge tube (m_2). 20 g of water was added to 1 g powder sample at room temperature to dissolve the powder. The tube vortexed for 2 min then centrifuged for 20 minutes at 6000 rpm at 4°C. The clear supernatant was discarded and the remaining residue (m_3) was weighed [23].

$$WBC = \left(m_3 - m_2\right)/m_1 \quad (1)$$

Oil Binding Capacity (OBC)

In order to determine the OBC of samples; 1 g of grounded sample (m_1) was placed in the tared centrifuge tube and 20 g oil (corn oil ρ: 0.9208 g/cm3) (m_2) was added on. The vortexed tube was centrifuged at 4°C for 20 minutes at 6000 rpm. Then the supernatant was discarded and the remaining residue (m_3) was weighed [23].

$$OBC = \left(m_3 - m_2\right)/m_1 \quad (2)$$

Swelling Capacity (SC)

For SC analysis; firstly 1 g of powdered sample (m) was placed in the cylinder and the occupied volume (V_1) was

measured. Then, 10 mL of water was added and agitation was carried out until a homogenous dispersion was obtained. The resulting dispersion is incubated for 24 hours at 25°C to allow the sample to fully bind the water. After 24 hours, the volume (V_2) of the wetted powder was measured and recorded.

$$SC = (V_2 - V_1)/m \quad (3)$$

SC is swelling of 1g sample with water and increased volume is expressed in mL [24].

Dietary Fiber Analysis

Total dietary fiber (TDF) and insoluble dietary fiber (IDF) contents of samples were determined by following AOAC-991.43 [25] and AACC-32-07 [26] standard methods and using a dietary fiber assay kit. Milled and weighed samples were transferred to beakers and they have first incubated with the heat resistant α-amylase enzyme at 95-100°C to provide hydrolysis of starch to dextrins, then incubated with protease enzyme at 60°C and finally amyloglucosidase enzyme was completely hydrolyzed to glucose by dextrins. Obtained extracts were treated with ethanol to precipitate the soluble dietary fiber, filtered through Gooch crucibles (40-60 µm pores) and the weight of the dried sediment was recorded. Total dietary fiber amounts were calculated by deducting the amount of protein and ash from the sediment weight. Insoluble dietary fiber contents of the samples were also determined enzymatically-gravimetrically by modifying the precipitation and leaching steps applied in total dietary fiber analysis as recommended by these standard methods.

Water Solubility Index (WSI)

WSI was performed with a small modification in the method indicated by Yousif et al. [27]. 1% aqueous solutions of the samples were taken into falcon tubes (S_1) and shook in a shaking water bath for 1 hour at a constant speed. The study was carried out at 10°C, 20°C, 30°C, 40°C, 50°C, 60°C and 70°C. The resulting mixture was centrifuged at 3000 g for 10 minutes. Then the supernatant was poured in a tared drying flask and dried at 105 °C for 18 hours and measured (S_2).

$$WSI = S_2/S_1 \times 100 \quad (4)$$

TGA & DTG Analysis

Thermal gravimetric analysis (TGA) was performed on a Perkin Elmer TGA7 analyzer and calibrated with calcium oxalate. 10 mg samples were used, and the test was carried out at a temperature range between 35-500°C and a heating rate of 10°C/min under a nitrogen atmosphere (nitrogen concentration 99.9%). Derivative thermogravimetry (DTG) was obtained to determine the maximum weight loss rate.

FT-IR Analysis

Fourier-transform infrared spectroscopy (FT-IR) analysis was done by weighing 5 mg of samples and mixing with 100 mg KBr. IR spectra were recorded between 4000-400 cm^{-1} under a 10-ton press at room temperature in Jasco 430 FT-IR spectrophotometer.

Statistical Analysis

SPSS V.22 packet program was used for statistical analyses. Duncan's new multiple range tests ($p<0.05$) was used to detect the differences among treatment means.

RESULTS AND DISCUSSION

pH and Proximate Analysis

The results of the pH and proximate analyses are shown in Table 1. Ash %, crude protein % and fat % composition were given in wet basis. The lowest pH value was determined in the grapefruit waste as 4.15. The pH of quince waste was 4.64 and the pH of tomato waste was 6.73. The pH value of fresh grapefruit fruit is reported to be around 2.8-3.1 [28]. A researcher reported that quince fruit pH value was between 3.30-3.40 and the quince juice obtained from these fruits have the same pH value [29], and another researcher group reported that the pH value of the tomato juices was between 4.21-4.57 according to the growing conditions [30]. The high pH values of fresh fruits and vegetables can be attributed to the relationship between pH and acidity. Since some of the organic acids were removed with the removal of fruit and vegetable juice, the pH of the waste was higher than the fresh state in our results.

The moisture content of the samples was; 4.8%, 6.67%, 7.4% for quince, grapefruit and tomato wastes respectively.

Table 1. pH, proximate and hydration properties analysis results

		Quince	Grapefruit	Tomato
pH		4.64±0.12^b	4.15±0.06^c	6.73±0.05^a
Moisture %		4.84±0.09^c	6.67±0.12^b	7.40±0.18^a
Ash %		0.98±0.02^c	1.76±0.02^b	5.11±0.01^a
Crude Protein %		1.41±0.41^c	3.28±0.17^b	13.60±0.43^a
Crude oil %		5.91±0.23^c	13.17±0.82^a	10.18±0.71^b
WBC (g/g)		6.41±0.18^b	13.09±0.01^a	6.62±0.36^b
OBC (g/g)		2.93±0.03^c	4.11±0.13^a	3.47±0.02^b
SC (mL/g)		2.70±0.14^b	5.85±0.21^a	2.00±0.2^{Bc}
Dietary Fiber	TDF	87.90±0.99^a	90.34±1.21^a	63.76±2.18^b
	SDF	5.22±0.29^c	7.03±0.25^a	6.10±0.23^b
	IDF	82.68±1.46^b	83.31±1.05^b	57.66±1.62^a

** Values are represented as mean ± standard deviation and different lowercase indicates significant differences in the same line ($p < 0.05$)*

Food wastes have high water content (80%) and it is stated that the moisture content should be reduced to around 7% to facilitate processing in the food industry and to obtain high dietary fiber-containing powder [10]. The ash contents were calculated as 0.98%, 1.76% and 5.11% in quince, grapefruit and tomato pulp, respectively. Ash content of tomato wastes was higher since samples taken from the tomato paste factory as a processing residue and this waste contains tomato stems, bunch and stalk. Crude protein amounts of the straws were determined as 1.41%, 3.28% and 13.60% for quince, grapefruit and tomato pulp, respectively. The percent of crude oil was determined as 5.91%, 13.17% and 10.18% in the same order. Dried and ground waste consists of different ratios of protein, lipid, ash, and fiber according to the type of harvested tomatoes [16]. Fresh fruit and vegetables have low percentages of protein, oil and ash than products and waste parts. All waste samples in our study have a higher amount of protein, oil and ash than the fresh state [31]. During processing (pressing, washing, peeling, heat treatment etc.) most components of fruit/vegetables are removed such as juice, skin (especially for citrus fruits) sugar, some other carbohydrates and micro components. This increases the protein, fat and ash ratio in the total mass.

WBC, OBC and SC Analysis

WBC, OBC, and SC analysis give information about the hydration properties and hence the functional properties of the substances. The hydration properties of the dietary fiber indicate the ability to absorb water in the fiber matrix. Fibers with potent hydration properties can increase faces weight, decrease the nutrient absorption rate from the intestine and increase the viscosity of foods in which it is added. Dietary fibers with high WBC can be used as functional components to prevent water release and to modify the viscosity and texture of some formulated foods. Dietary fibers with high OBC allow stabilization of high-fat food products and emulsions, prevent aroma migration and reduce fat loss during cooking [4, 14, 32].

WBC is defined as the amount of water held by a 1 g dry sample under specific conditions. According to the results of WBC, 1g quince waste bound 6.41 g water, grapefruit waste bound 13.09 g water and tomato pulp bound 6.62 g water. Although quince and grapefruit wastes have closer TDF amount, grapefruit showed nearly two times WBC and OBC capacity than quince and tomato wastes. One of the reasons is; soluble part of the fiber is higher in the grapefruit sample; the other result may cause by grapefruit albedo content and structure of other components. The hydration properties of dietary fibers are related to the chemical structure of the polysaccharides in their compositions and other factors such as porosity, particle size, ionic form, pH, temperature, ionic strength, type of ions in solution and stresses on the fibers. Water retention of dietary fiber is closely related to the source of dietary fiber [4].

OBC is expressed as the weight of g of oil bound by 1 g of sample. According to the results of the OBC analysis; 1 gram of quince waste bound 2.93 g oil, the grapefruit pulp bound 4.11 g oil, and the tomato pulp bound 3.47 g oil. Grapefruit pulp has the highest WBC and OBC. Grapefruit TDF is attractive since it exhibited higher soluble/insoluble DF in lowering the absorption of lipids [33]. Quince and tomato samples have similar WBC and OBC values, only the quince sample was slightly higher. OBC of fibers is important in food applications; for example, the ability to increase the amount of feces by absorbing or binding bile acids is associated with plasma reduction and is effective in preventing fat loss during cooking. OBC depends on the overall density, thickness, surface properties of the fibers and hydrophobic nature of the fiber particle [14]. Insoluble fibers can bind up to 5 times their weight [32].

SC is the occupied volume of the known fiber weight under certain conditions. According to the results of the analysis, samples have a swelling capacity of 2.7 mL/g, 5.85 mL/g and 2.0 mL/g for quince, grapefruit, and tomato respectively. High SC is related to the amount of insoluble dietary fiber and is associated with a low amount of soluble fiber [14]. As shown in the dietary fiber content results; the insoluble fiber content of the grapefruit pulp is very high and it is expected that the SC is high. In the same table, the lowest amount of fiber in the insoluble fiber content is tomato waste, and this sample also has the lowest SC value. In a study, WBC of dietary fiber obtained from the orange juice is determined as 7.3 g/g and OBC value 1.27 g/g [34]. A researcher studied the tomato peel fiber and reported that the WBC was 6.76 g/g, OBC was 1.46 g/g and the SC was 0.11 mL/g [14].

Dietary Fiber Analysis

According to the results of the dietary fiber analysis, the grapefruit sample has the highest TDF at 90.34%. The IDF ratio of this sample was determined as 83.31%. The hydration properties of dietary fibers such as swelling and water binding capacity are related to IDF (32), so the grapefruit waste sample has the highest SC and WHC. TDF amount of quince waste was determined as 87.90% and IDF was 82.68%. While tomato pulp has the lowest TDF ratio (63.76%) compared to other types of pulp, it has also the lowest IDF ratio (57.66%). The dietary fiber contents of the samples are shown in Table 1.

Thomas and Thibault [35]. reported that quince fruit contains 28-38% fiber due to its genotype. In a study, researchers determined the total fiber content of dried and ground orange juice by-products as 63.6% and the amount of soluble fiber as 17.4% [36]. Navarro-González et al., analy-

zed tomato skin fiber and they found that the total dietary fiber amount was 84.16% and the amount of insoluble fiber as 71.82% [14]. Since the amount of fiber is higher in the skin, their TDF results higher than TDF of our tomato sample. The high content of cellulose and hemicellulose in vegetable skins increased the total and insoluble fiber ratio in their sample. Savadkoohi et al. reported that the total fiber content of tomato pulp residue from tomato paste manufacturing was about 40%. Studies show that there are differences between the total fiber and soluble, insoluble fiber fractions of fruits, vegetables, and their residue [16]. These differences are thought to be caused by modifications in cell wall polysaccharides which may have both nutritional and functional effects [37].

Water Solubility Index (WSI)

Solubility is an important quality parameter and affects the functional properties of the powder in solid food systems, relates to the structure of polysaccharides; in the spine or the side chains regularly (insoluble) or irregular (soluble) settlements are effective. The presence of a substituent such as COOH or SO_4^{2-} groups and increasing temperature increases the solubility [4]

According to the WSI analysis (shown in table 2); the solubility of samples was increased as the temperature increases for all three types of samples. The soluble fraction of the total dietary fiber is effective in the water solubility properties of the pulps. Grapefruit pulp with high soluble fiber content was more dissolved than other pulps. The tomato pulp with the lowest soluble pulp was identified as the least soluble pulp type. The water solubility of the fibers depends on the SDF amount [32, 38]. Moreover, due to the positive effect of the temperature on the solubility, the solubility was increased by increasing the applied temperature for all samples.

TGA and DTG Analysis

Thermal analysis of foods gives information about food nature and modification during food processing. TGA analysis of quince, grapefruit and tomato waste are given in Fig. 2. In this analysis, the thermal behavior and degradation of the samples are revealed, DTG curves are given in Fig. 3. to see results better.

There was no significant weight loss at initial temperatures, all three samples started to lose weight after approximately 200°C. Negligible weight losses observed at temperatures below 200°C are attributed to the removal of moisture and the onset of hydrolysis in polysaccharides [39]. All three samples have high fiber content and major components of crude fiber are cellulose, hemicellulose and lignin [40]. Generally, biomass pyrolysis is specifying these three main components. Lignocellulosic biomass is believed to be stable up to 200°C [41].

The quince pulp showed a large peak with a maximum decomposition point of 345°C adjacents to an unclear peak around 200°C to 310°C. Cellulose has been reported to have higher thermal stability than hemicellulose and lignin, and lignin degradation begins at relatively low temperatures and progresses over a wide temperature range [42]. Thus, the peak onset was estimated to indicate degradation of the lignocellulosic structure, including hemicellulose, and the maximum point of the peak indicated cellulose. It is reported that the maximum decomposition temperature is higher in quince lignin samples in which sugar and phenolic compounds are removed, leading to more stable lignin structures after pretreatment [43].

Grapefruit pulp yielded two peaks that can be acceptable in a relatively narrow temperature range between 240°C

Table 2. WSI of samples

Temperature	*Quince (%)*	*Grapefruit (%)*	*Tomato (%)*
10°C	9.2 ± 1.70^{abE}	10.9 ± 0.42^{aC}	7.2 ± 0.28^{bC}
20°C	11.8 ± 1.41^{aDE}	10.7 ± 0.99^{abC}	7.6 ± 0.28^{bC}
30°C	12.5 ± 0.14^{aD}	10.9 ± 1.56^{abC}	7.7 ± 0.85^{bC}
40°C	25.0 ± 1.13^{aC}	21.4 ± 3.96^{abB}	15.0 ± 1.13^{bB}
50°C	28.9 ± 1.27^{aB}	25.6 ± 0.85^{aB}	15.2 ± 1.41^{bB}
60°C	31.6 ± 0.57^{aB}	37.0 ± 4.24^{aA}	17.0 ± 0.57^{bAB}
70°C	36.1 ± 1.56^{bA}	41.9 ± 0.71^{aA}	18.4 ± 1.98^{cA}

** Values are represented as mean ± standard deviation and different lowercase indicates significant differences in the same line, uppercases in the same column indicate a significant difference (p<0.05)*

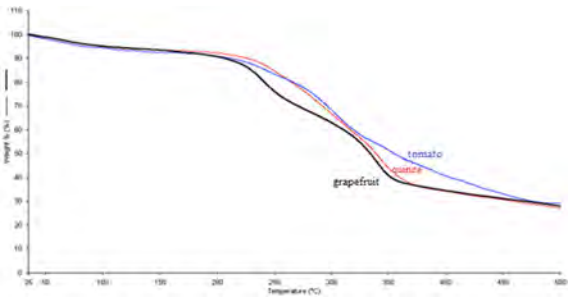

Figure 2. TGA analysis of samples

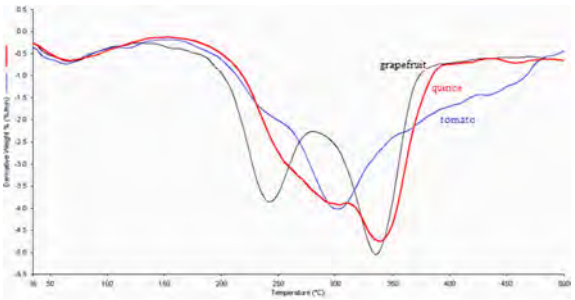

Figure 3. DTG analysis of samples

and 340°C. It was estimated that the first peak was hemicellulose and the second peak was cellulose, as hemicelluloses showed the least thermal stability in cellulosic compounds due to the presence of acetyl groups [42] while hemicelluloses typically decompose in the range of 160-360°C, cellulose degrades at a higher temperature; 240-390°C [39]. In a study on orange waste, thermal decomposition was reported to occur in two stages; first hemicelluloses decompose between 125°C and 250°C, second cellulose degradation between 250°C and 360°C was reported. It has been noted that simultaneous lignin decomposition is also present in the same temperature range [44].

The tomato pulp contains a high proportion of polysaccharides such as fiber and pectin [16]. Tomato waste yielded a wide peak starting at around 200°C peakings at 300°C and continuing to 500°C. It is estimated that this peak formed over a wide temperature range is lignin which forms an important part of the tomato content but also contains lignin as well as cellulose and hemicellulose. There is a general idea that thermal decomposition peaks partially overlap hemicellulose, cellulose, and lignin [42]. For thermal decomposition analysis of tomato waste, it is reported that the DTG curves have a large number of peaks, indicating a quite complex pyrolysis. The complex thermal behavior of tomato samples can be illustrated by complex chemical composition characterized by the presence of various macro and micro components. The second and third peaks have been reported to results of thermal degradation of hemicelluloses and cellulose [39, 45].

FT-IR Analysis

IR spectra are a spectroscopic technique that provides information about the molecules or functional groups carried by molecules in a pure or mixed analyte. FT-IR spectra of quince, grapefruit and tomato pulp are given in Fig. 4. In the fingerprint region (500-1500 cm^{-1}, specific for each item) there are differences in signal strength and observed signals. The range of 1600-1700 cm^{-1} is carbonyl bands; the signal of C=C containing molecules in the samples. Especially in the spectrum of tomato waste at 1627 cm^{-1}, the signal is more severe compared to other samples and it can be explained by conjugated C=C bonds of lycopene and its derivatives in tomato waste. 1550-1650 cm^{-1} si gnals indicate free carboxyl groups and 1730-1745 cm^{-1} signals indicate esterified carboxyl groups. The signals observed in the range of 1700-1800 cm^{-1} for all three samples indicate the presence of molecules carrying the C=O functional group (phenolics, terpenoids, steroids, organic acids, etc., bearing the carboxylic acid or carbonyl group). In a study on pectin isolated from grapefruit peels; it was reported that all pectin samples produced absorptions at 2930 cm^{-1} corresponded to the C-H stretching of the -CH, $-CH_2$ and $-CH_3$ groups [46]. In a study on pectin isolated from tomato waste, FT-IR analysis showed a strong OH band due to the presence of carboxylic acids in the range of 3300-2500 cm^{-1} [47].

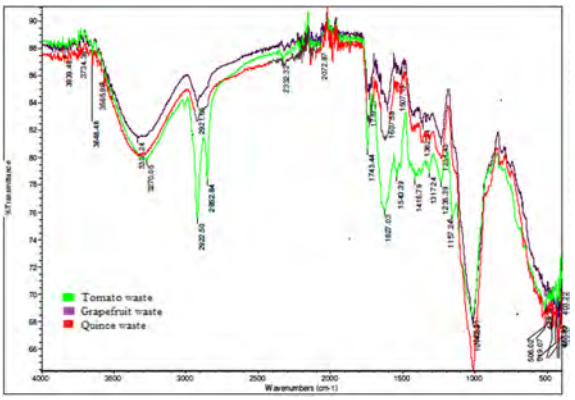

Figure 4. FT-IR chromatogram of samples

CONCLUSION

All over the world, food waste is increasing as the food industry develops. These wastes cause environmental pollution and economic problems as well as the loss of valuable food components. A large portion of these losses are fruit and vegetable wastes and contain a significant amount of valuable components. These by-products are rich in dietary fiber content has many benefits to human health. In this study; by-products of quince, grapefruit and tomato processing were evaluated and their contents and functional properties were determined. The lowest moisture content, ash, protein and fat content were determined in quince waste. The moisture, ash and protein content of tomato waste is higher than other pulp types. Concerning this result, the TDF amount of tomato waste is lower than other wastes. Quince, grapefruit and tomato wastes have high hydration properties, in terms of WBC, OBC and SC and also all of them have high dietary fiber content. Grapefruit waste has higher TDF, SDF, and IDF, so this sample showed higher hydration properties than other samples, since its high albedo content. The use of such samples instead of other hydrocolloids in food formulations will be more economical due to waste product evaluation and is a natural supplement that will increase the reliability of the product and reduce the environmental problem of the operators. Also, high dietary fiber contents of these samples employ fat-reduced, sugar-reduced, functional products. Their use in the food industry such as dairy products, meat products, emulsions, etc. as hydrocolloid, filler, fat replacer is possible and has many advantages.

ACKNOWLEDGEMENT

There is no funder, researchers have done this work with their own means.

References

1. Yağcı S, Altan A, Göğüş F, Maskan M. Gıda atıklarının alternatif kullanım alanları. Türkiye 9 Gıda Kongresi. 2006:499–502.
2. Jin Q, Yang L, Poe N, Huang H. Integrated processing of plant-derived waste to produce value-added products based on the biorefinery concept. Trends in Food Science & Technology. 2018.
3. Salihoglu G, Salihoglu NK, Ucaroglu S, Banar M. Food loss and waste management in Turkey. Bioresource technology. 2017.
4. Elleuch M, Bedigian D, Roiseux O, Besbes S, Blecker C, Attia H. Dietary fibre and fibre-rich by-products of food processing: Characterisation, technological functionality and commercial applications: A review. Food chemistry. 2011;124(2):411–21.
5. Köksel H, Özboy Ö. Besinsel lif analiz yöntemleri. Gıda/ The Journal of Food. 1993;18(1).
6. Mehta N, Ahlawat S, Sharma D, Dabur R. Novel trends in development of dietary fiber rich meat products–a critical review. Journal of food science and technology. 2015;52(2):633–47.
7. Wojdyło A, Teleszko M, Oszmiański J. Antioxidant property and storage stability of quince juice phenolic compounds. Food chemistry. 2014;152:261–70.
8. Yin H-S, Liu H-M, Liu Y-L. Structural Characterization of lignin in fruits and stalks of Chinese Quince. Molecules. 2017;22(6):890.
9. Jouki M, Yazdi FT, Mortazavi SA, Koocheki A. Physical, barrier and antioxidant properties of a novel plasticized edible film from quince seed mucilage. Int J Biol Macromol. 2013;62:500–7.
10. Fernandez-Lopez J, Fernandez-Gines J, Aleson-Carbonell L, Sendra E, Sayas-Barbera E, Perez-Alvarez J. Application of functional citrus by-products to meat products. Trends in Food Science & Technology. 2004;15(3–4):176–85.
11. FernandezńLopez J, SendrańNadal E, Navarro C, Sayas E, ViudańMartos M, Alvarez JAP. Storage stability of a high dietary fibre powder from orange byńproducts. International journal of food science & technology. 2009;44(4):748–56.
12. Yoshida Y, Ueda M. Citrus juice waste as a potential source of dietary fiber. Journal of the Japanese Society for Horticultural Science. 1984;53(3):354–61.
13. Lario Y, Sendra E, Garcıa-Pérez J, Fuentes C, Sayas-Barberá E, Fernández-López J, et al. Preparation of high dietary fiber powder from lemon juice by-products. Innovative Food Science & Emerging Technologies. 2004;5(1):113–7.
14. Navarro-González I, García-Valverde V, García-Alonso J, Periago MJ. Chemical profile, functional and antioxidant properties of tomato peel fiber. Food Res Int. 2011;44(5):1528–35.
15. Sönmez K, Ellialtıoğlu ŞŞ. Domates, karotenoidler ve bunları etkileyen faktörler üzerine bir inceleme. Derim. 2014;31(2):107–30.
16. Savadkoohi S, Hoogenkamp H, Shamsi K, Farahnaky A. Color, sensory and textural attributes of beef frankfurter, beef ham and meat-free sausage containing tomato pomace. Meat Sci. 2014;97(4):410–8.
17. Moon KM, Kwon E-B, Lee B, Kim CY. Recent trends in controlling the enzymatic browning of fruit and vegetable products. Molecules. 2020;25(12):2754.
18. Kumara B, Wijewardane R, Samarasinghe Y. The Effect of Anti-Browning Treatments for Fresh-Cut Guava Slices in Prevention of Browning during Dehydration. 2021.
19. AOAC. Official method of analysis Proximate Analysis and Calculations Moisture. Method 934.01. Association of Official Analytical Communities2006.
20. AOAC. Official method of analysis Proximate Analysis and Calculations Total Nitrogen or Crude Protein. Method 990.03. Association of Official Analytical communities2006.
21. AOAC. Official method of analysis Proximate Analysis and Calculations Crude Fat. Method 920.39. association of Official Analytical communities2006.
22. AOAC. Official method of analysis Proximate Analysis and Calculations Ash. Method 942.05. Association of Official Analytical communities2006.
23. Gençcelep H, Sarıcaoğlu FT, Anıl M, Ağar B, Turhan S. The effect of starch modification and concentration on steady-state and dynamic rheology of meat emulsions. Food Hydrocolloid. 2015;48:135–48.
24. Lecumberri E, Mateos R, Izquierdo-Pulido M, Rupérez P, Goya L, Bravo L. Dietary fibre composition, antioxidant capacity and physico-chemical properties of a fibre-rich product from cocoa (Theobroma cacao L.). Food Chemistry. 2007;104(3):948–54.
25. AOAC. AOAC Official Method. Association of Official Agricultural Chemists, by the United States Department of Agriculture. 2000.
26. AACC. Aapproved Methods of the American Association of Cereal Chemists. 2004;11th edition.
27. Yousif E, Gadallah M, Sorour AM. Physico-chemical and rheological properties of modified corn starches and its effect on noodle quality. Annals of Agricultural Sciences. 2012;57(1):19–27.
28. Aylangan A, Başbayraktar V, Çetinkaya N, Denli E, Erçin D, Erel Y, et al. Narenciye grubu meyvelerde karantina amaçlı ışınlamanın gıda kalitesi ve hijyeni üzerine etkisinin araştırılması. Türkiye Atom Enerjisi Kurumu, Teknik rapor. 2010;TAEK TR-2010-2.
29. Güven S. Ayva Suyu ve Konsantratı Üzerinde bir Araştırma. Gıda/The Journal of Food. 1982;7(6).
30. Şahin Ü, Özdeniz A, Zülkadir A, Alan R. Sera koşullarında damla sulama yöntemi ile sulanan domates (Lycopersicon esculentum Mill.) bitkisinde farklı yetiştirme ortamlarının verim, kalite ve bitki gelişmesine olan etkileri. Of Agriculture and Forestry. 1998;22:71–9.
31. http://www.turkomp.gov.tr/food [Internet]. Turkomp. 2021.
32. Burdurlu HS, Karadeniz F. Gıdalarda diyet lifinin önemi. Gıda Mühendisliği Dergisi. 2003;7(15):18–25.
33. Khalil MN, Farghal HH, Farag MA. Outgoing and potential trends of composition, health benefits, juice production and waste management of the multi-faceted Grapefruit Citrus ń paradisi: A comprehensive review for maximizing its value. Critical Reviews in Food Science and Nutrition. 2020:1–22.
34. Grigelmo-Miguel N, Martin-Belloso O. Characterization of dietary fiber from orange juice extraction. Food Res Int. 1998;31(5):355–61.
35. Thomas M, Thibault J-F. Cell-wall polysaccharides in the fruits of Japanese quince (Chaenomeles japonica): extraction and preliminary characterisation. Carbohyd Polym. 2002;49(3):345–55.
36. de Moraes Crizel T, Jablonski A, de Oliveira Rios A, Rech

R, Flores SH. Dietary fiber from orange byproducts as a potential fat replacer. LWT—Food Science and Technology. 2013;53(1):9–14.
37. Tosh SM, Yada S. Dietary fibres in pulse seeds and fractions: Characterization, functional attributes, and applications. Food Res Int. 2010;43(2):450–60.
38. Gan J, Peng G, Liu S, Hu X, Wang X, Guo S, et al. Comparison of structural, functional and in vitro digestion properties of bread incorporated with grapefruit peel soluble dietary fibers prepared by three microwave–assisted modifications. Food & Function. 2020;11(7):6458–66.
39. Brachi P, Miccio F, Miccio M, Ruoppolo G. Pseudo–component thermal decomposition kinetics of tomato peels via isoconversional methods. Fuel Processing Technology. 2016;154:243–50.
40. Monday R, Ephraim V, Julius N, Olaitan R, Idowu B. Effects of inclusion of processed grapefruit pulp on wheat flour biscuit. Journal of Food Technology. 2020;7(1):69–77.
41. Özsin G, Pütün AE. Kinetics and evolved gas analysis for pyrolysis of food processing wastes using TGA/MS/FT–IR. Waste Management. 2017;64:315–26.
42. Sebio–Puñal T, Naya S, López–Beceiro J, Tarrío–Saavedra J, Artiaga R. Thermogravimetric analysis of wood, holocellulose, and lignin from five wood species. J Therm Anal Calorim. 2012;109(3):1163–7.
43. Qin Z, Zhang Z–G, Liu H–M, Qin G–Y, Wang X–D. Acetic acid lignins from Chinese quince fruit (Chaenomeles sinensis): effect of pretreatment on their structural features and antioxidant activities. RSC Advances. 2018;8(44):24923–31.
44. Lopez–Velazquez M, Santes V, Balmaseda J, Torres–Garcia E. Pyrolysis of orange waste: a thermo–kinetic study. Journal of Analytical and Applied Pyrolysis. 2013;99:170–7.
45. Mangut V, Sabio E, Gañán J, González J, Ramiro A, González C, et al. Thermogravimetric study of the pyrolysis of biomass residues from tomato processing industry. Fuel Processing Technology. 2006;87(2):109–15.
46. Wang W, Wu X, Chantapakul T, Wang D, Zhang S, Ma X, et al. Acoustic cavitation assisted extraction of pectin from waste grapefruit peels: A green two–stage approach and its general mechanism. Food Res Int. 2017;102:101–10.
47. Grassino AN, Halambek J, Djakovic S, Brncic SR, Dent M, Grabaric Z. Utilization of tomato peel waste from canning factory as a potential source for pectin production and application as tin corrosion inhibitor. Food Hydrocolloid. 2016;52:265–74.

Hittite Journal of Science and Engineering, 2021, 8 (1) 27–33
ISSN NUMBER: 2148–4171
DOI: 10.17350/HJSE19030000209

Corrosion Behavior of Graphene Nanoplatelet-Coated TiB_2 Reinforced AZ91 Magnesium Matrix Semi-Ceramic Hybrid Composites

Engin Cevik, Murat Gundogan, Alper Incesu, Muhammet Emre Turan
Karabuk University, Department of Metallurgical and Materials Engineering, Karabuk, Turkey

ABSTRACT

In this study; Hybrid composites containing different proportions of TiB_2 and graphene were produced using the pressure infiltration method. Inert SF6 gas is used to prevent oxidation in the productions. While 8 bar infiltration pressure was provided by argon gas, the infiltration temperature was chosen as 800°C. The corrosion behaviors of the composite materials were examined. Corrosion resistance was determined by potentiodynamic and immersion corrosion testing in 3.5% NaCl solution. In addition, SEM examinations were conducted to understand the corrosion mechanisms. At the end of the measurements, the highest porosity was measured as %4,7 in composite containing 1% graphene compared to pure matrix and composite containing only TiB2. The added reinforcement (TiB2 and Graphene) elements cause decreases in corrosion resistance. The highest corrosion resistance was achieved in AZ91 alloys.

Article History:
Received: 2020/09/26
Accepted: 2021/02/10
Online: 2021/03/31

***Correspondence to**: Engin Cevik, Karabuk University, Metallurgical and Materials Engineering, 78000, Karabük, TURKEY*
E-Mail: engincevik@karabuk.edu.tr

Keywords:
Graphene, AZ91, TiB_2, Magnesium matrix composites, Corrosion.

INTRODUCTION

Recent environmental protection policies focus on the need to reduce the weight of vehicles in order to increase fuel efficiency and reduce the impact of greenhouse gases emission [1]. Magnesium stands out as the structural metal in cases where weight reduction is important for materials used in industry and vehicles [2]. Low density, good strength to weight ratio, better heat dissipation, acceptable damping capacity, machinability, and recyclability make magnesium a much more attractive structural metal compared to steel and aluminum [2–4]. Despite all these superior properties, high corrosion rate in aggressive environments, relatively low absolute strength, and elastic modulus when compared to other metallic structural materials are the most important unfavorable properties of magnesium alloys [2,5–7].

One way to produce high strength, corrosion-resistant magnesium alloys is the production of Mg-based composites by the addition of reinforcement particles such as ceramics [7]. Reinforcement of Mg matrix composites (MMCs) with suitable ceramic particles such as SiC, TiC, and TiB_2 can exhibit high specific strength and acceptable corrosion resistance when the correct combination of reinforcement and a light metal matrix is used [8]. Properties of magnesium matrix such as corrosion resistance, wear resistance, hardness can be developed with Ti-based ceramic particles (TiC, TiAlC, and TiB_2 reinforcement [8–10]. For magnesium matrix composites, TiB_2 is a highly compatible reinforcing element because the crystal structures of the two are compatible with each other as a hexagonal closed pack (HCP).

Another method to increase strength and corrosion resistance is the addition small amount of nano-sized particles with high surface area (such as carbon nanotube and graphene) to the magnesium matrix also causes significant increases in mechanical properties and corrosion resistance of composite [11–14]. Say et al. [15] determined that AZ61 and AZ91 matrix composites reinforced with lower CNTs (0.1 wt.% or 0.2 wt.%) and non-reinforced alloy had better corrosion resistance than composites reinforced with higher CNTs (0.5 wt.%). Similarly, Munir et al. [16] reported that Mg–Graphene nanoplatelets (GNP) composites were reinforced with 0.1 wt.% GNP showed the best corrosion resistance in the same corrosion environment as compared to the pure Mg.

Table 1. Chemical composition of AZ91 (wt %).

Alloy	Mg	Al	Fe	Mn	Ni	Zn	COST-231 Hata
AZ91	89,9	9	0,005	0,33	0,002	0,7	-23,7

In this study, graphene nanoplatelet-coated TiB_2 was added to AZ91 magnesium alloy to see the effect of both TiB_2 ceramic particles and high surface area graphene on the corrosion properties of AZ91 matrix composites. Four different AZ91 matrix composites containing graphene and TiB_2 in different ratios were produced by the pressure infiltration method for the first time to the best of our knowledge. Corrosion characteristics of produced composites were investigated comparatively.

MATERIAL AND METHODS

High purity (99,9 %) graphene nanoplates and TiB_2 particles (99,95 % purity) were used as reinforcement materials in this study and commercial AZ91 alloy, the chemical composition of which is given in Table 1, was used as the matrix element. The first stage is the preparation of reinforcement materials. At this stage, the graphene doping process to TiB2 particles with an average particle size of 45 microns was performed using the vacuum distillation method.

Graphene nano-plates were added into ethyl alcohol in the proportions given in Table 2 and the graphene-ethanol suspension was formed by mixing in the ultrasonic bath. After that, TiB_2 particles were added in determined proportions (Table 2) and mixed during 15 minutes. Then, the alcohol in the suspension evaporated from the vacuum distillation at 200°C on the magnetic stirrer. As a result, TiB_2 particles containing three different ratios of graphene were produced.

Table 2. Volume (%) contents of the produced samples.

Composites	Volume Fraction (%)		
	TiB_2	GNP	AZ91
s1	0	0	100
S2	50	0	50
s3	49,75	0,25	50
s4	49,5	0,5	50
s5	49	1	50

The second stage is the preparation of preforms. 7 mm inner diameter and 350 mm length 316L quality stainless tubes, which are shown in Fig. 1, are used as preform holders. The end of the stainless tube is covered with an alumina filter with 85% porosity. Preforms with a length of Ø7x50 mm were prepared by hand vibrating in a stainless tube so that the reinforcement ratio was 50%. The preform was covered

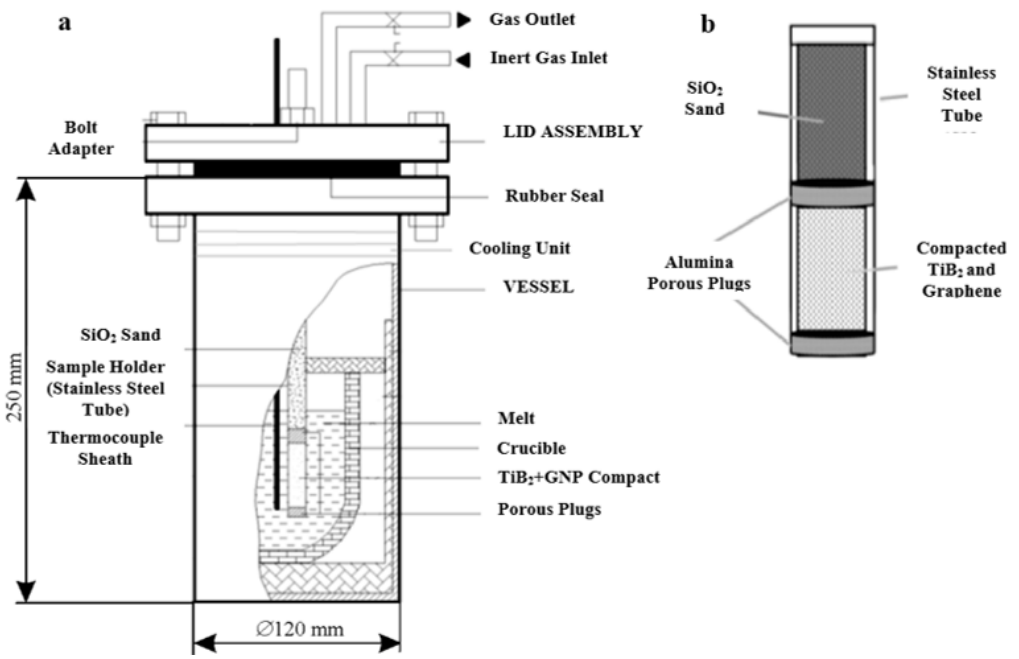

Figure 1. Schematic view of the assembly (a) diagram of the stainless steel tube specimen holder (b).

with an alumina filter and the remaining part of the tube was filled with silica cast sand in order to provide the homogeneous distribution of particles during infiltration.

Finally, the AZ91 alloy we prepared in a 600 gr capacity crucible was placed in the assembly and the cover of the assembly was closed using a plastic gasket. Later, the furnace was raised to 800°C, which is determined as the infiltration temperature, and kept for 1 hour in order to ensure complete melting. Sf6 gas was passed through the assembly to provide an inert gas environment for production.

The preform in a stainless tube was immersed in the melt and kept for 2 minutes for the liquid metal to reach its temperature. Finally, 8 bar infiltration pressure was applied with argon gas and left for 2 minutes, then argon gas was released from the unit. After the composites were produced, they were removed from the infiltration unit. The stainless tubes were cleaned from the surface with a lathe and the composites were obtained.

In order to bring the produced composite materials to the desired dimensions, they were cut with a diamond disc cutting device. The grinding process was applied with an automatic machine from coarse to fine (240-1200 mesh SiC) grits and then the polishing process was completed with 3 µm and 0.3 µm alumina.

SEM images were taken on the Carl Zeiss Ultra Plus Gemini Fesem device. XRD analysis of prepared composite samples was performed at 40 kV generator voltage, 30 mA current in the range of 20° -90°, and with a scanning step of 0.02.

Experimental density measurement was carried out according to the Archimedes principle. The theoretical density was measured by the mixture principle and % porosity amounts were determined by both of using these data.

Two different corrosion tests were applied to composite specimens, namely potentiodynamic and immersion types of corrosion. A potentiodynamic polarization test was carried out in PARSTAT 4000 device in a 3.5% NaCl solution. The composite specimens prepared were molded in bakelite with open front and back for holding. Thanks to the holder prepared before, the samples were placed in the device and the tests were carried out. A pair of graphite rods were used as counter electrodes and a saturated calomel electrode (SCE) was used as a reference electrode for free corrosion potential measurements. Tests were carried out at room temperature. To determine the open circuit (OC) value in the tests, -400 mV was applied to the samples for 900 seconds by 1 mV/s scan rate. As a result of the tests, the corrosion rate in mm/year was calculated using Faraday's law with the following formula;

$$CR = 3,27x10^{-3}\, x\, I_{corr}\, x(EW) / d \quad (1)$$

CR: corrosion rate (mm/year),
I_{corr}: corrosion current density (µA/cm^2),
EW: equivalent weight (gr) and
d: density (gr/cm^3).

Composite samples prepared for immersion tests were first weighed with precision scales. Then, the polymer net was dipped into the mixture prepared with distilled water containing 3.5% NaCl in a glass jar at room temperature. The composite samples were taken out of the glass jar in 3,6,12,24 hours and cleaned for 5 minutes with the help of distilled water, and then weighed with a precision scale after cleaning with alcohol and drying. After weighing, the samples were put back into the polymer net and immersed in the solution in the glass jar and the measurements were made again at the specified hours. At the end of 24 hours, surface images were taken from the samples with an EDS attached to an SEM microscope. At the end of the test, corrosion behavior was determined depending on the amount of graphene added, taking into account the weight loss.

RESULTS AND DISCUSSION

Doped graphene nanoplatelets to TiB_2 particles with Van Der Waals bonds was achieved with the vacuum distillation process. SEM photographs of TiB_2 particles that do not contain graphene and 1% graphene doped TiB_2 reinforcement are shown in Fig. 2. Although it is seen in partial agglomerations, it can be said that graphene nanoplatelets are attached successfully to the surface of the TiB_2 particle.

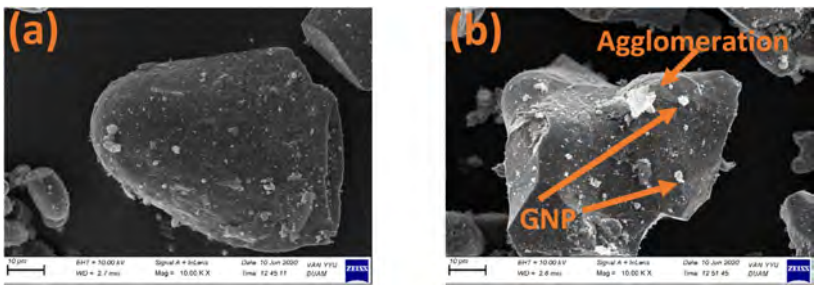

Figure 2. SEM images of GNP added TiB_2 powders a) 0% and b) 1%.

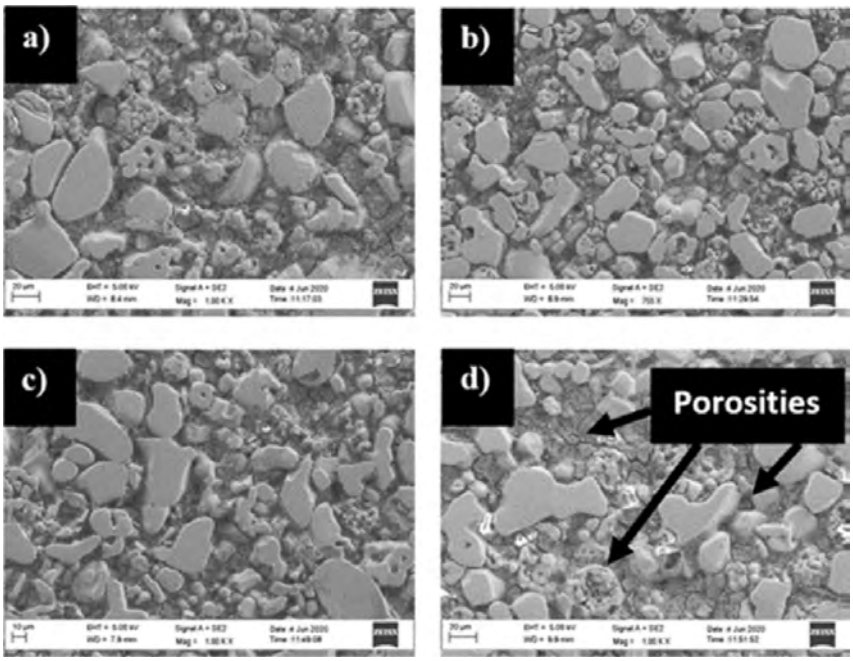

Figure 3. a) AZ91+TiB_2, b) 0.25% GNP+AZ91+TiB_2 c) 0.5% GNP+AZ91+TiB_2 and d) 1% GNP+AZ91+TiB_2.

The microstructure images of the produced hybrid composites are given in Fig. 3. Unlike other composite production methods, the pressure infiltration method makes it possible to produce with high reinforcement elements [17]. For example, while the powder metallurgy production method can reach a maximum of 30% by volume, it is observed that agglomeration in the structure increases and porosity reaches unacceptable levels at higher reinforcement rates [18]. When hybrid composites produced with 50% particle reinforcement are evaluated fabricated by pressure infiltration method, it can be deduced that homogeneous particle distribution is achieved successfully in all graphene ratios. However, as the proportion of graphene in the structure increased, the amount of porosity increased by 5% compared to non-graphene reinforced composites due to the adverse effect of wettability between the reinforcement and the matrix (Table 3) [19-20].

With liquid metal infiltration, it has been observed that liquid metal diffusion occurs even between particles that are very close to each other. This result shows that the infiltration process is successful despite the very high reinforcement content and that the strong interaction between the reinforcement and matrix can be fully achieved. However, micro-cracks can be attributed to the differences in the cooling rate between the reinforcement and the matrix materials are occurred.

Table 3. Density and porosity results of produced samples.

Sample Code	*Theoretical Density*	*Actual Density*	*Porosity*
S2	*3,165*	*3,035*	*4,10742*
S3	*3,159*	*3,012*	*4,65337*
S4	*3,153*	*3,005*	*4,69394*
S5	*3,148*	*3,00001*	*4,70108*

Fig. 4 shows the XRD analyzes made on the composite samples. When X-ray diffractions are analyzed, the $Al_{12}Mg_{17}$ compound is detected in the matrix element [8]. In the produced composites, the TiB_2 phase is observed in addition to the magnesium and $Al_{12}Mg_{17}$ phases. Furthermore, there is no extra peak and this situation shows that no phase formation occurs during the production phase due to the interaction of the reinforcement and the matrix.

The corrosive properties of the composites were investigated in a 3.5% NaCl solution. The potentiodynamic po-

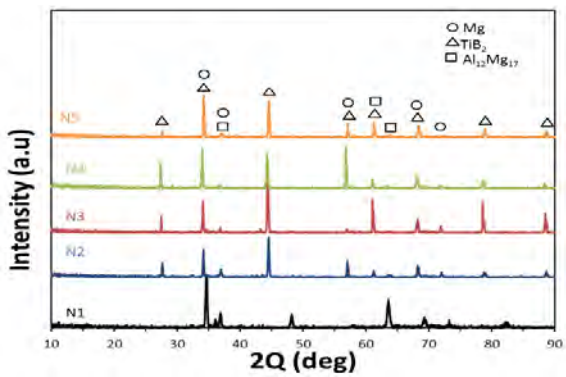

Figure 4. XRD analysis results of fabricated composites.

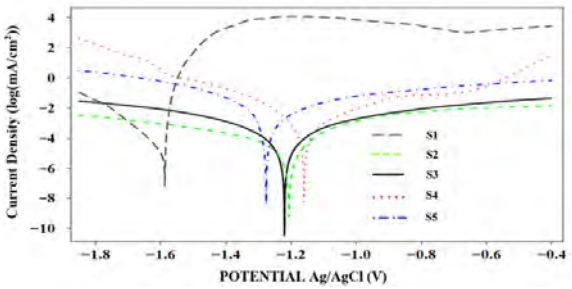

Figure 5. Potentiodynamic polarization test charts.

larization test was performed separately in the anodic and cathodic regions (Scanning Interval: -0.4 V vs. Ag / AgCl to -1.85 V vs. Ag / AgCl) and the results are shown in Fig. 5.

Composites with TiB_2 reinforced AZ91 matrix exhibits higher I_{corr} values than an unreinforced alloy (Table 4). This can be attributed to the galvanic coupling between the reinforcement phase and the magnesium matrix. The matrix element acts as the anode while the reinforcing element acts as the cathode. For this reason, a very rapid reaction occurs in the first place and this process continues until the anode is exhausted. The fact that the reinforcement phase did not pass into the solution but settled to the bottom during the experiment.

Corrosion (E_{corr}) values were obtained at the end of the 15 min. open circuit test. Corrosion rates which are calculated with Faraday's law of produced samples are presented in Table 4.

Considering the corrosion rate (CR) and icorr (CCD) values given in Table 4, the lowest corrosion rate is observed in the S1 coded sample. The highest corrosion rate can be seen in the sample coded S5. As a result of the analysis made on Tafel curves, the ceramic reinforcement made dramatically reduces the corrosion resistance of the metal matrix. Reinforcement materials such as SiC, TiB_2 are known as inert materials because they act as inert electrodes. When a metal of sufficient conductivity forms a galvanic couple, it leads to the formation of a corroded surface very quickly [21].

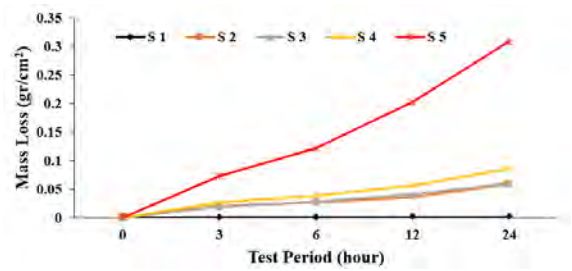

Figure 6. Immersion corrosion results in 3.5% NaCl.

The galvanic coupling formed between TiB2 reinforcement and the AZ91 matrix increased significantly with the addition of graphene to the structure and accelerated the corrosion of the matrix. As it is known, potentiodynamic tests are generally performed in very short periods. In order to support these results, immersion corrosion tests were carried out in the same environment.

The results of the immersion corrosion test conducted for 24 hours support the potentiostat tests. As shown in Fig. 6, it has been observed that all composite types exhibit lower corrosion resistance compared to the AZ91 matrix. However, the most noteworthy part here is the great decrease in corrosion resistance after the addition of graphene. This decrease reached its maximum levels with the addition of 1% graphene. This is due to the galvanic coupling that occurs between the matrix and the reinforcement. On the other hand, it is thought that increasing porosity amounts with the addition of graphene have a negative effect on corrosion resistance and increase crevice corrosion [22,23,24].

When immersion test results are evaluated, remarkable detail is that the slopes of the mass loss-time graph of magnesium matrix composites consist of two different regions. Namely, an increase is observed in the slope of the graphs after the first 6 hours in all samples. The reason for this can be thought to be the corrosive solution moves into the sample and increases the corrosion rate.

TiB_2 particles, which remain stable with the dissolution of the matrix element, separate from the structure and collapse to the bottom when they are disconnected from the matrix, which causes the loss of mass to increase more than expected [23].

Table 4. Potentiodynamic polarization test results.

Specimen	*Surface Area (cm^2)*	*CC (μA)*	*CCD (μA / cm^2)*	*CR (mm / year)*	*E_{corr} (V)*
S1	*0.283*	*2.10*	*7.42*	*0.16*	*-1.59*
S2	*0.283*	*9.14*	*32.30*	*0.40*	*-1.21*
S3	*0.283*	*19.87*	*70.21*	*0.88*	*-1.02*
S4	*0.283*	*36.94*	*130.53*	*1.63*	*-1.16*
S5	*0.283*	*80.43*	*284.20*	*3.55*	*-1.28*

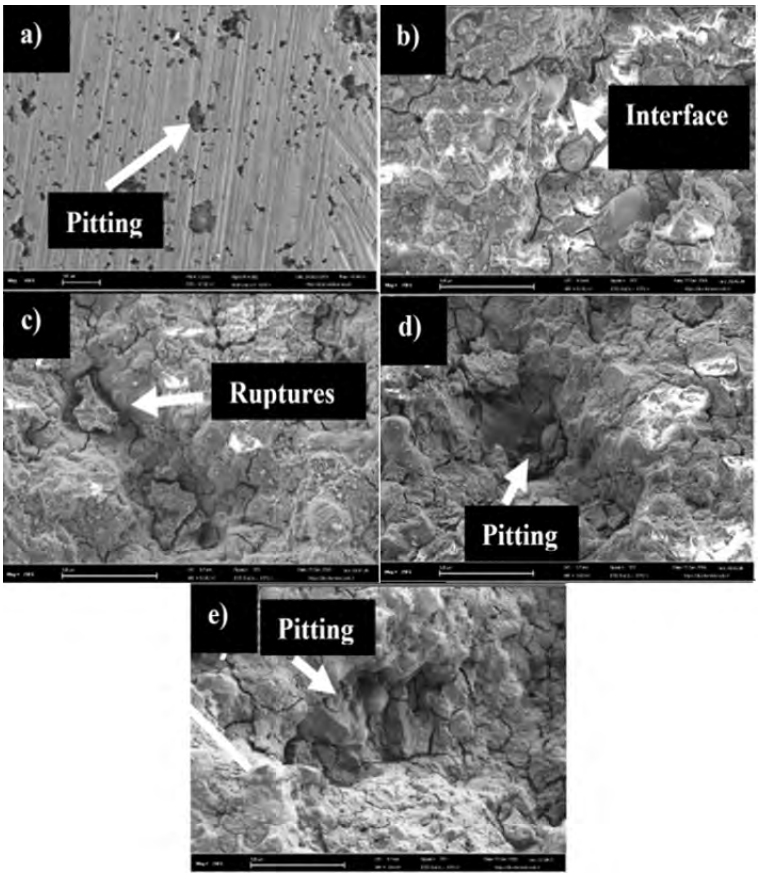

Figure 7. SEM analysis a) AZ91, b) AZ91+TiB_2, c) AZ91+TiB_2+%0,25 GNP, d) AZ91+TiB_2 +%0,5 GNP, e) AZ91+TiB_2 +%1 GNP after immersion tests.

In Fig. 7, corroded surface photographs of the examined composite materials are shown. When SEM photographs of the corroded surface are examined, it can be seen that the aggressive solution environment where the pitting potential increases with the addition of both TiB_2 and graphene causes higher mass loss. Corrosion that started at the matrix and reinforcement interface resulted in the dissolution of the surrounding matrix element by the TiB_2 particles acting as cathodes and the particles detached from the structure during the experiment.

CONCLUSION

In this study, different ratios of graphene and TiB_2 reinforced composite materials with the AZ91 matrix were produced by the pressure infiltration method. Corrosion tests were carried out for all samples produced. As a result of this study;

a) As a result of the metallographic examination, it was observed that the TiB2 reinforcement element was homogeneously distributed in composite reinforcement materials.

b) According to the density measurement, the porosity ratio increased with the increasing graphene ratio.

c) When potentiodynamic and immersion corrosion tests are examined, it has been that the corrosion resistance decreases as the reinforcement element increases. Generally, the corrosion mechanism in the structure has been determined as pitting and crevice corrosion.

ACKNOWLEDGMENT

This study was supported by the Scientific Research Projects Coordination Unit of Karabuk University within the scope of the project numbered KBÜ-BAP-18-YL-110.

References

1. Ramalingam VV, Ramasamy P, Kovukkal MD, Myilsamy G. Research and development in magnesium alloys for industrial and biomedical applications: a review. Met. Mater. Int. (2019) 1–22.
2. Mingo B, Arrabal R, Mohedano M, Pardo A, Matykina E. Corrosion, and wear of PEO coated AZ91/SiC composites. Surf. Coat. Technol. 309 (2017) 1023–1032.
3. Luo AA. Materials comparison and potential applications of magnesium in automobiles. in: Essent. Read. Magnes. Technol., Springer, pp. 25–34, 2016.
4. Wang XM, Wang XJ, Hu XS, Wu K, Zheng MY, Processing, microstructure, and mechanical properties of Ti6Al4V particles-reinforced Mg matrix composites. Acta Metall. Sin. Engl. Lett. 29 (2016) 940–950.
5. Razavi M, Fathi MH, Meratian M. Microstructure, mechanical

properties, and bio-corrosion evaluation of biodegradable AZ91-FA nanocomposites for biomedical applications. Mater. Sci. Eng. A. 527 (2010) 6938–6944.
6. Razavi M, Fathi M, Savabi O, Razavi SM, Heidari F, Manshaei M, Vashaee D, Tayebi L. In vivo study of nanostructured diopside (CaMgSi2O6) coating on magnesium alloy as biodegradable orthopedic implants. Appl. Surf. Sci. 313 (2014) 60–66.
7. Song J, She J, Chen D, Pan F. Latest research advances on magnesium and magnesium alloys worldwide. J. Magnes. Alloys. (2020).
8. Gobara M, Shamekh M, Akid R, Improving the corrosion resistance of AZ91D magnesium alloy through reinforcement with titanium carbides and borides. J. Magnes. Alloys. 3 (2015) 112–120.
9. Jiang QC, Li XL, Wang HY. Fabrication of TiC particulate reinforced magnesium matrix composites. Scr. Mater. 48 (2003) 713–717.
10. Sahoo BN, Panigrahi SK. Synthesis, characterization, and mechanical properties of in-situ (TiC-TiB2) reinforced magnesium matrix composite. Mater. Des. 109 (2016) 300–313.
11. Du X, Du W, Wang Z, Liu K, Li S. Ultra-high strengthening efficiency of graphene nanoplatelets reinforced magnesium matrix composites. Mater. Sci. Eng. A. 711 (2018) 633–642.
12. Xiang SL, Gupta M, Wang XJ, Wang LD, Hu XS, Wu K. Enhanced overall strength and ductility of magnesium matrix composites by low content of graphene nanoplatelets. Compos. Part Appl. Sci. Manuf. 100 (2017) 183–193.
13. Rashad M, Pan F, Hu H, Asif M, Hussain S, She J. Enhanced tensile properties of magnesium composites reinforced with graphene nanoplatelets. Mater. Sci. Eng. A. 630 (2015) 36–44.
14. Turan ME, Sun Y, Akgul Y. Mechanical, tribological and corrosion properties of fullerene reinforced magnesium matrix composites fabricated by semi powder metallurgy. J. Alloys Compd. 740 (2018) 1149–1158.
15. Say Y, Guler O, Dikici B. Carbon nanotube (CNT) reinforced magnesium matrix composites: The effect of CNT ratio on their mechanical and corrosive properties. Mater. Sci. Eng. A. (2020) 139636.
16. Munir K, Wen C, Li Y. Graphene nanoplatelets-reinforced magnesium metal matrix nanocomposites with superior mechanical and corrosion performance for biomedical applications. J. Magnes. Alloys. (2020).
17. Candan E, Ahlatci H, Cimenoglu H. Abrasive wear behaviour of Al–SiC composites produced by pressure infiltration technique. Wear. 247 (2001) 133-138.
18. Aydın F, Sun Y, Ahlatci H, Turen Y. Investigation of Microstructure, Mechanical and Wear Behaviour of B4C Particulate Reinforced Magnesium Matrix Composites by Powder Metallurgy. Trans. Indian Inst. Met. 71 (2018) 873-882.
19. Kavımani V , Prakashi KS and Thankachan T. Investigation of graphene-reinforced magnesium metal matrix composites processed through a solvent-based powder metallurgy route. Department of Mechanical Engineering, Anna University Regional Campus, Coimbatore 641 046, India, 2019.
20. Sun X, Li C, Dai X, Zhao L, Li B, Wang H, Liang C, Li H, Fan J. Microstructures and properties of graphene-nanoplatelet-reinforced magnesium-matrix composites fabricated by an in situ reaction process, J.Alloys Compd. 835 (2020) 155125.
21. Zakaria, HM. Microstructural and corrosion behavior of Al/SiC metal matrix composites. Ain Shams Engineering Journal. 5 (2014) 831-838.
22. Turhan MC, Li Q, Jha H, Singer RF, Virtanen S. Corrosion behavior of multiwall carbon nanotube/magnesium composites in 3.5% NaCl. Electrochşimica Acta. 56 (2011) 7141-7148.
23. Turan ME, Sun Y, Akgul Y, Turen Y, Ahlatci H.The effect of GNPs on wear and corrosion behaviors of pure magnesium. J.Alloys Compd. 724 (2020) 14-23.
24. Rashad M, Fusheng Pan F, Asif M, Chen X. Corrosion behavior of magnesium-graphene composites in sodium chloride solutions. J. Magnes. Alloys. 5 (2017) 271-276.

Hittite Journal of Science and Engineering, 2021, 8 (1) 35–40
ISSN NUMBER: 2148–4171
DOI: 10.17350/HJSE19030000210

Surface Acoustic Wave Induced Heat Knockdown of Caenorhabditis Elegans

Adem Ozcelik
Aydin Adnan Menderes University, Department of Mechanical Engineering, Aydın, Turkey

ABSTRACT

Model organisms such as Caenorhabditis elegans are commonly used in discovering the underlying mechanisms of human diseases. The field of microfluidics enables a plethora of tools for better studying these organisms. In this research, an effective and simple approach is demonstrated for thermally induced knockdown of Caenorhabditis elegans model organisms. To achieve this, surface acoustic waves are coupled to the fluid medium inside a microfluidic channel. Without active cooling, two pairs of propagating surface acoustic waves induce very rapid heating of the enclose fluid. By controlling the input power of the acoustic waves, temperature of the fluid is precisely adjusted, and induced reversible knockdown of Caenorhabditis elegans samples. Effective temperature window of acoustically induced thermal knockdown is characterized, and the tolerable number of knockdown and wake up cycles is studied. Viability of the Caenorhabditis elegans organisms is also evaluated after increasing numbers of knockdown cycles. Overall, a simple and effective method of worm immobilization method is demonstrated using acoustic waves in microfluidics.

Keywords:
C. elegans, Immobilization, Microfluidics, Surface acoustic waves, Thermoacoustics

Article History:
Received: 2020/10/04
Accepted: 2021/02/04
Online: 2021/03/31

***Correspondence to**: Adem Özçelik*
Department of Mechanical Engineering,
Aydın Adnan Menderes University,
Aydın, Turkey
Tel: +90 5350465266
Fax: +90 2562136686
E-Mail:aozcelik@adu.edu.tr

INTRODUCTION

Caenorhabditis elegans (C. elegans) is a versatile model organism used for studying various human diseases due to its easy maintenance, adequate complexity in terms of biological functionality, and short life cycle allowing observation of its entire developmental cycle in a week [1,2]. Because of its small size, which is around 1 mm in adulthood, microfluidic platforms have been widely adopted for studying C. elegans [3,4]. Microfluidics is a relatively new field which is targeting miniaturization of bioanalysis, chemical synthesis, sample processing, and disease diagnostics [5–9]. For C. elegans related research, microfluidics provides small and well-controlled micro environments enabling convenient microscopic investigation [10,11]. However, in order to precisely image cellular and subcellular structures of these organisms, they are required to be immobilized during optical imaging.

There are three general approaches for steadily observing and imaging the cellular details of this organism which are chemically, physically and thermally induced immobilization [12,13]. In chemical immobilization, various chemicals including levamisole and sodium azide are used to sedate the worms similar to the anesthetics administer in surgical procedures [14]. Even though, chemical immobilization works quickly and effectively, their biological effects on the worm metabolism is not clear [15]. For biological research in which no foreign biochemical interference is desired, administering these chemicals is not suitable. The second approach is physical immobilization through restricting the motion of the worms by using various microfluidic methods [3]. One of these methods is using thin membrane based suction to physically immobilize a worm inside a microfluidic channel [16]. These methods generally require complex microfluidic device fabrication which is not available in many laboratories in low-budget institutions. Microfluidic immobilization also imposes a predefined geometry which can obstruct clear manipulation and/or observation of the worms. Finally, thermal worm immobilization can be applied either by heating or cooling the worms to specific temperatures to minimize their metabolic activity or induce thermal shock, respectively [17]. In cooling approach, worms take a curled shape minimizing their body length which renders detailed microscopic imaging more challenging. For the temperature induced heat shock worms are immobilized in a temperature controlled environment. In one example, a laser is applied to induce rapid temperature increase inside a multi-layered fluidic device [18]. This

method proves effective worm immobilization, but device fabrication and operation are complicated due to the required multi-layer conductive channels and application of lasers. In addition, application of a single laser spot makes this method low throughput. Considering the challenges and disadvantages of the existing worm immobilization methods, there is still a need for a simpler and more practical method that can provide effective and high throughput worm immobilization.

In this work, a standing surface acoustic wave (SSAW)-based microfluidic method is demonstrated for inducing controllable heat knockdown of C. elegans worms. Acoustic methods enable a versatile platform in many fields [19,20]. The method presented in this work relies on acoustically generated rapid temperature increase inside a microfluidic channel. C. elegans worms are repeatedly induced into recoverable heat shocks, and their endurances and recovering periods are characterized. Overall, as a potential method for worm researchers, a SSAW-based method is applied in C. elegans immobilization for the first time in literature.

MATERIAL AND METHODS

Device fabrication is completed in two steps. In the first step, interdigitated transducers (IDTs) are patterned on a lithium niobate ($LiNbO_3$) piezoelectric wafer which is a transparent, 128° Y-cut piezoelectric crystal. Standard photolithography is applied to fabricate the gold electrodes of the IDTs. For this, initially a positive photoresist (Megaposit™ SPR™220) is spin-coated on the $LiNbO_3$ wafer. Then, a photomask with the desired electrode pattern is used to expose the photoresist, and subsequently developed in the resist developer. Afterwards, 5 nm of chromium and 200 nm of gold layers are coated on top of the patterned wafer via vacuum thermal evaporation. Finally, coated wafer is incubated in acetone for overnight to liftoff the gold layers coated on the remaining photoresist regions. General steps of IDT fabrication are shown in Fig 1. The design of the IDTs includes 50 μm wide electrodes separated by 50 μm distance. The design of the IDTs is chosen to be straight to uniformly cover the width of the microfluidic channel. The wavelength of the SAWs corresponds to four times the width of the electrodes of IDTs. Using the speed of sound in 128° Y-cut LiNbO3 at room temperature (3980 m/s) and the wave frequency conversion equation ($f=v/\lambda$, where f is the frequency, v is the speed of sound and λ is the wavelength), we can find the resonance frequency of the fabricated IDTs for 50 μm electrodes to be around 20 MHz.

In the second step, a microfluidic channel is fabricated via soft lithography process. Soft lithography refers to a precise replica molding method. For this step, a master mold containing the positive features of the microfluidic channel is fabricated through photolithography and deep reactive ion etching (DRIE) processes [21]. Briefly, a silicon wafer is spin coated with the positive photoresist, and exposed with a photomask. Then developed and bake at 90 °C for about 20 minutes. The silicon wafer now contains photoresist coated regions where microfluidic channel features are located. The rest of the silicon wafer surface is just bare silicon. DRIE process is applied to this wafer to etch the non-resist coated regions to a depth of 100 micrometers which defines the microfluidic channel height. 100-micrometer channel height is chosen to allow unrestricted infusion of larger worms into the fluidic channel preventing potential device clogging. DRIE etched wafer is then washed with acetone to clear to rest of the resist covering the un-etched regions.

Once the silicon master mold is fabricated, a mixture of Polydimethylsiloxane (PDMS) is poured on top of the mold surface. After curing at 60 °C for around 2 hours, the liquid PDMS solidifies and forms a transparent elastomer. The microfluidic channels are peeled and cut to smaller devices. Then, inlets and outlets of the PDMS device is punched to enable polyethylene tube and thermocouple insertion. The port for the thermocouple probe is made slightly smaller than the actual thermocouple tip to avoid any potential leakage. Finally, the PDMS device is bonded to LiNbO3 using plasma activation of both surfaces, and overnight baking at 60°C.

The SSAW-based microfluidic device is driven by an arbitrary signal generator (AFG1062, Tektronix). The imaging of the worms is performed using an inverted microscope equipped with a high definition camera (OX.2053-PLPH, Euromex). Wild type C. elegans worms are grown in agar medium at 20 °C, and Escherichia coli (OP50) is used as the nutrition source [11]. Worms are collected in an M9 buffer solution for conducting the microfluidic experiments. Worms are delivered into the microfluidic device through a custom designed automated syringe pump. Temperature inside the channel is measured by a fine tip temperature probe (TJ Probe, Omega).

To evaluate the viability of the worms after each knockdown cycle, the worms within the active acoustic treatment region are collected in a fresh M9 solution. To avoid collecting non-treated worms, inlet and outlet tubing of the device are replaced with the new tubes in each cycle. Then, 20 μM propidium iodide solution is added to 200 μL worm solution. After the staining, the worms are collected in a petri dish containing agar plate. The collected worms are observed for motility, and propidium iodide stain. The scoring of the live and dead worms is completed under the microscope.

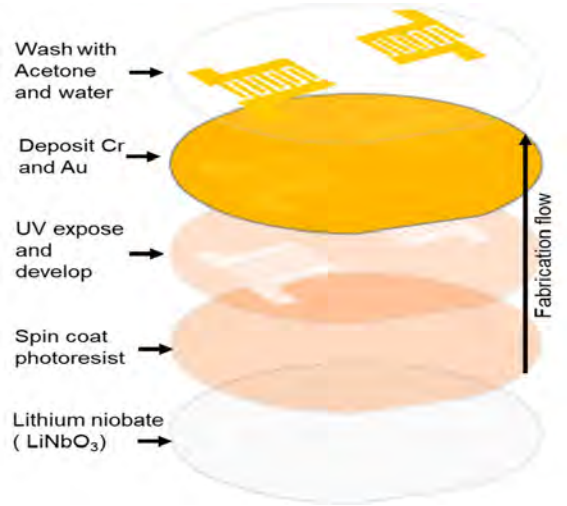

Figure 1. Fabrication of IDTs on a lithium niobate substrate. First, a positive photoresist is spin-coated on the lithium niobate wafer. Second, the coated surface of the wafer is UV exposed through a photomask with the desired IDT patterns, and the wafer is developed. Then 5 nm chromium and 200 nm gold is deposited on the lithium niobate surface.

RESULTS AND DISCUSSION

The schematic model and the actual standing surface acoustic wave-based microfluidic device are shown in Fig. 2. The microfluidic channel is designed to have curved inner surfaces to prevent microbubble trapping inside the channel. The inlet in the center area of the microfluidic channel is used to insert the temperature probe into the device. The two symmetrically fabricated IDTs are used to generate two travelling surface acoustic waves in opposite directions, and form standing waves inside the fluidic channel. The aim of using the SSAWs in this device is to amplify and provide evenly distributed thermoacoustic effects of the acoustic waves within the fluid volume inside the microfluidic channel. The tip of temperature probe tightly fits in the center inlet providing liquid tight connection. It is also important to note that the tip of the temperature probe is not touching to the lithium niobate surface to prevent additional heating that may be transferred through solid surfaces.

The correlation between the applied voltage and the medium temperature inside the microfluidic device is observed to be linear, and is given in Fig. 3. Here, the measurements are taken after the inner temperature is stabilized at a given applied voltage value. The experiments are repeated for 6 times for each voltage value to obtain adequate statistical data. Average value of the temperature readings from different experiments are plotted along with the standard deviations. The data in Fig. 3 is collected using a 20 MHz SSAW device. One can also use a higher or lower resonant frequency device to induce a gradual temperature increase inside a microfluidic channel. The only difference between these devices would be the required applied voltage to reach the same temperature.

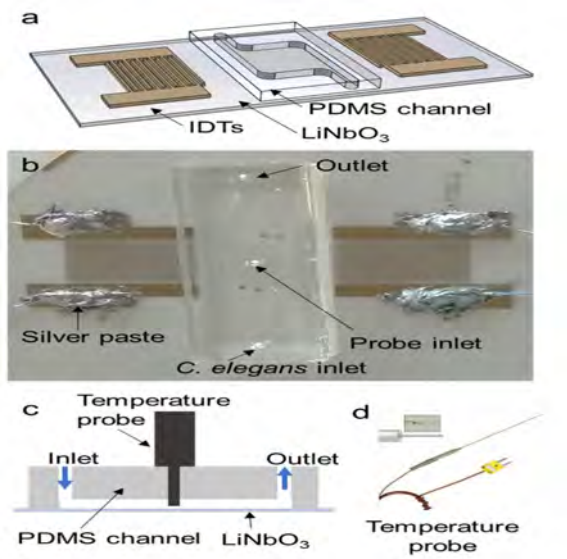

Figure 2. General overview of the device. a) Schematic and b) actual standing surface acoustic wave device. c) side view of the microfluidic device demonstrating the inlets and the outlets. d) picture of the fine tip temperature probe. The tip of the probe has a 0.5 mm diameter and 2.4 mm length.

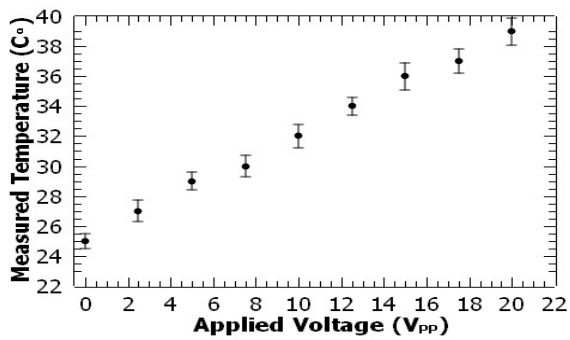

Figure 3. Experimental relationship between the applied voltage to the IDTs and the measured temperature inside the microfluidic channel. Experiments are started at room temperature. A linear relationship is observed between the applied voltage and the temperature. The error bars represent the standard deviation of 6 different measurements at each voltage value.

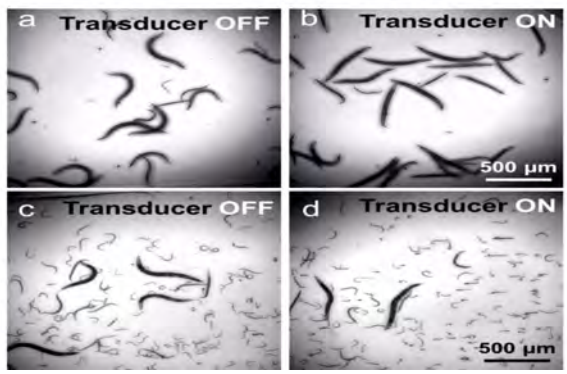

Figure 4. Experimental observation of C. elegans worm behavior under the effect of temperature rise in the presence of acoustic waves. a) Low and c) high concentrations of C. elegans are shown to be in their natural swimming body postures without any acoustic treatment. b) and d) When the acoustic waves are applied with 15 VPP, worms are immobilized with the effect of the heat shock, and their body posture becomes more elongated.

An example C. elegans treatment experiment is demonstrated in Fig. 4. Both low concertation adult populations (Figs. 4a and b) and high concentration mixed development stage worms (Figs. c and d) are shown to be effectively immobilized by application of 15 VPP input voltage. In both cases, when the transducer is off, worms exhibit natural swimming body postures with curved shapes. In the M9 buffer, which is a liqud medium, C. elegans worms perform swimming motion via body undulations unlike crawling motion they do in more viscous and granular agar medium. Once the transducer is turned on, acoustic waves induce a rapid heating and subsequent temperature rise inside the fluidic chamber. C. elegans worms go through a thermal shock demonstrating seizure like body motions for few seconds and finally are knockdown. After heat induced knowckdown (Figs. 4b and d) body posture of the worms become more elongated similar to chemical immobilization. No observable difference is recorded in the thermal immobilization behavior of different developmental stage worms.

To better elucidate the effect acoustically generated heat on worm knockdown, the effective temperature window that worms goes through knockdown and become immobilized is studied. For these experiments, fresh batches of worm populations are introduced into the microfluidic chamber before each temperature setting. As seen in Fig. 3, the temperate of the fluid medium can be adjusted from 25 °C to 39 °C by adjusting he applied voltage from 3 Vpp to 20 Vpp. Starting from the room temperature and going up to 39°C, different worm batches are exposed to acoustically generated heat, and the state of the worms are studied from their physical movements. Results of these experiments are given in Fig. 5. As observed from the figure, below 32 °C, worms do not exhibit heat knockdown. Starting from 32 °C, worms start to go through the seizures and eventual knockdown. 35 °C is found to be an effective temperature for rapid knockdown of worms. Above 37 °C, the effects of the temperature become detrimental to the worm biology, and worms die after the seizures. In Fig. 5, a knockdown window is demonstrated.

The C. elegans worms are heavily dependent on the environmental conditions including temperature fluctuations. Under the detrimental temperatures such as 38 °C and above, the neural circuitry of the worm turns off to protect the animal to a certain degree. The temperature window that is demonstrated in Fig. 5 outlines the range of temperatures where C. elegans can shut down some of its neural activity and receive no damage. Within this range of temperature, the worms can wake up once the excessive temperature is removed. The microfluidic environment enables very rapid heating of the worm medium, and similarly heat dissipation due to the small volumes of fluids. Acoustic waves can induce instantaneous temperature increase within the domain of the fluid media that the Rayleigh waves of the SAWs leak into.

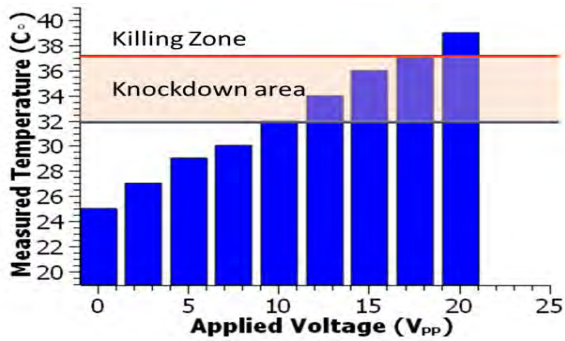

Figure 5. Demonstration of effective temperature window for worm immobilization. An interval between 32 °C and 37 °C is identified to induce heat knockdown of worms. Mixed population worm samples are used in these experiments.

In Fig. 6, the time required for knockdown and wake up of the C. elegans is demonstrated. Here, each experiment is conducted at 35 °C. The quantification of the experiments is done by observation of complete knockdown and revival of the worm population exposed to the thermal treatment. For each worm sample in the microfluidic device, 10 cycles of rapid temperature increase and decrease are applied. In total 20 batches of worms are used, and each batch is cycled 10 times. Error bars are calculated from the standard deviation of the 20 different experiments for each cycle order. From this data set shown in Fig. 6, it is observed that within the first 4 cycles, the time required for the knockdown and wake up is fairly constant and less than 10 seconds for each. However, starting from the fifth cycle, wake up times are gradually increasing. This indicates that subsequent cycling of the same worms (continuous knockdown and wake up) adversely affect the worm physiology and require longer durations for wake up. Nevertheless, within the first five cycles, the required time for thermal immobilization and recovery is quite fast, and reasonable for the 6^{th}, 7^{th}, and 8^{th} cycles which are under 100 seconds. Considering the chemical immobilization of C. elegans which require minutes for the knockdown and wake up, the acoustically induced heat knockdown is more effective in terms of time requirements.

In worm experimentation using microfluidic channels, knockdown of worms several times can be a reasonable demand. According to Fig. 6, standing surface acoustic wave-based method can provide up to 8 immobilization cycling safely. In addition, when a continuous duration of immobilization is required for C. elegans operations and imaging, the knockdown induced temperature can be sustained for the entire duration of the study. After the operation is completed, induced elevated temperature can be removed by turning off the acoustic field.

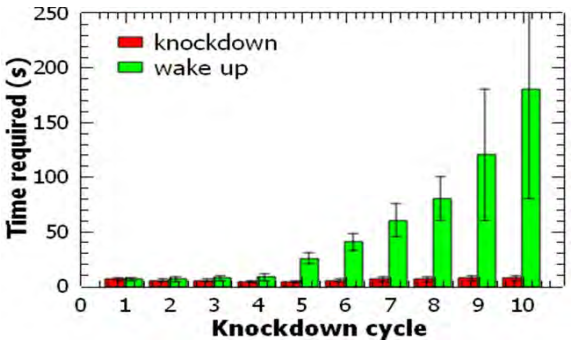

Figure 6. Demonstration of the time requirement for knockdown and wakeup after repeated cycles. After the first 4 cycles, it takes longer for the worm to recover from the effect of the knockdown. Each cycle is repeated 20 times for different batches of worms. Error bars represent the standard deviation of 20 data points for each cycle. Mixed population worm samples are used in these experiments.

After measuring the time required for the thermal immobilization of the worms, it is also important to study the detrimental effects of the knockdown and wake up cycles on worm biology. For this, the rate of viability is characterized after cycling the worms. Individual worms are counted to score the dead and live worms after each knockdown and wake up. In Fig. 7, the results of the scoring are given. According to the graph, worm viability is in the range of 95% within the first 4 cycles. In the 5th and 6th cycles, the viability drops to around 85%. After the 10th cycle, the worm viability becomes 50%. Compare to the other worm immobilization methods including chemical and thermal, acoustically induced method enables both a high throughput and rapid immobilization method. For instance, using the method presented in this study (which can also be referred as the thermoacoustic method), worm immobilization can be applied anytime within he microfluidic channel whereas chemical treatment of the worms requires the administration of the chemical agents and certain time to allow sedation resulting in worm immobilization.

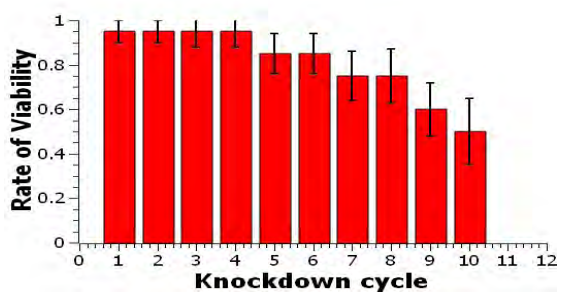

Figure 7. Demonstration of the effect of repeated knockdown cycles on worm viability. As a general trend, viability drops with the repeated number of cycles. Error bars are obtained from standard deviation of three different experiments for each cycle. Mixed population worm samples are used in these experiments.

Furthermore, with the acoustic method, the active region of the SSAW field, can be divided into smaller sections by fabricating smaller pairs of IDTs. This way, only a selected group of worms can be treated and immobilized. Thanks to the rapid heat dissipation occurring in the microfluidics, the induced temperature rise can be contained only within the active acoustic field.

CONCLUSION

Herein, a new method of C. elegans immobilization is demonstrated using a standing surface acoustic wave-based microfluidic device. Thermoacoustically induced rapid temperature rises are applied inside a microfluidic channel to temporarily immobilize worm samples. The time required for immobilization is found to be much smaller compared to the chemical methods. The acoustic method is also more advantages compared to the laser-driven thermal methods due to the high throughput and device simplicity enabled by the surface acoustic wave device. Overall, the method presented in this work can be a valuable tool for worm researchers due to its simplicity, versatility and adoptability into microfluidic platforms.

ACKNOWLEDGEMENTS

This research was supported by Adın Adnan Menderes University Research Fund. Project Number: MF-20002.

REFERENCES

1. Kaletta, T., Hengartner, M.O. Finding function in novel targets: C. elegans as a model organism. Nature Reviews. Drug Discovery. 5(5) (2006) 387–98. doi: 10.1038/nrd2031.
2. Rohde, C.B., Zeng, F., Gonzalez-Rubio, R., Angel, M., Yanik, M.F. Microfluidic system for on-chip high-throughput whole-animal sorting and screening at subcellular resolution. Proceedings of the National Academy of Sciences of the United States of America. 104(35) (2007) 13891–5. doi: 10.1073/pnas.0706513104.
3. Gilleland, C.L., Rohde, C.B., Zeng, F., Yanik, M.F. Microfluidic immobilization of physiologically active Caenorhabditis elegans. Nature Protocols. 5(12) (2010) 1888–902. doi: 10.1038/nprot.2010.143.
4. Cáceres, I. de C., Valmas, N., Hilliard, M.A., Lu, H. Laterally orienting C. elegans using geometry at microscale for high-throughput visual screens in neurodegeneration and neuronal development studies. PLoS ONE. 7(4) (2012) e35037. doi: 10.1371/journal.pone.0035037.
5. Tosun, E., Ozgur, T., Ozgur, C., Ozcanli, M., Serin, H., Aydin, K. Comparative analysis of various modelling techniques for emission prediction of diesel engine fueled by diesel fuel with nanoparticle additives. European Mechanical Science. 1(1) (2017) 15–23. doi: 10.26701/ems.320490.
6. Akmeşe, B., Asan, A. Optimization of the Schiff-Base Reaction of Acetylacetone with Biogenic Amines. Hittite Journal of Science and Engineering. 4(1) (2017) 79–83. doi: 10.17350/HJSE19030000052.
7. Erdoğan, B., Topuz, A., Engin, T., Baş, A., Yeter, A. Numerical and Experimental Investigation of the Effect on Heat Transfer of Nanofluid Usage in Mini/Micro Channels. Hittite Journal of

Science & Engineering. 5 (2018) doi: 10.17350/HJSE19030000113.

8. Orbay, S., Ozcelik, A., Bachman, H., Huang, T.J.T.J. Acoustic actuation of in situ fabricated artificial cilia. Journal of Micromechanics and Microengineering. 28(2) (2018) 025012. doi: 10.1088/1361-6439/aaa0ae.
9. Ayan, B., Ozcelik, A., Bachman, H., Tang, S.-Y.S.-Y., Xie, Y., Wu, M., et al. Acoustofluidic coating of particles and cells. Lab Chip. 16(22) (2016) 4366–72. doi: 10.1039/C6LC00951D.
10. Ozcelik, A., Nama, N., Huang, P.-H.H., Kaynak, M., McReynolds, M.R.M.R.M.R., Hanna-Rose, W., et al. Acoustofluidic Rotational Manipulation of Cells and Organisms Using Oscillating Solid Structures. Small. 12(37) (2016) 5120–5. doi: 10.1002/smll.201601760.
11. Ahmed, D., Ozcelik, A., Bojanala, N., Nama, N., Upadhyay, A., Chen, Y., et al. Rotational manipulation of single cells and organisms using acoustic waves. Nature Communications. 7 (2016) 1–11. doi: 10.1038/ncomms11085.
12. Gupta, B., Rezai, P. Microfluidic Approaches for Manipulating, Imaging, and Screening C. elegans. Micromachines. 7(7) (2016) 123. doi: 10.3390/mi7070123.
13. Ben-Yakar, A., Chronis, N., Lu, H. Microfluidics for the analysis of behavior, nerve regeneration, and neural cell biology in C. elegans. Current Opinion in Neurobiology. 19(5) (2009) 561–7. doi: 10.1016/j.conb.2009.10.010.
14. Cheng, C.M., LeDuc, P.R., Lin, Y.W. Localized bimodal response of neurite extensions and structural proteins in dorsal-root ganglion neurons with controlled polydimethylsiloxane substrate stiffness. Journal of Biomechanics. 44(5) (2011) 856–62. doi: 10.1016/j.jbiomech.2010.12.006.
15. Massie, M.R., Lapoczka, E.M., Boggs, K.D., Stine, K.E., White, G.E. Exposure to the metabolic inhibitor sodium azide induces stress protein expression and thermotolerance in the nematode Caenorhabditis elegans. Cell Stress & Chaperones. 8(1) (2003) 1. doi: 10.1379/1466-1268(2003)8<1:ETTMIS>2.0.CO;2.
16. Yanik, M.F., Cinar, H., Cinar, H.N., Chisholm, A.D., Jin, Y., Ben-Yakar, A. Neurosurgery: functional regeneration after laser axotomy. Nature. 432(7019) (2004) 822. doi: 10.1038/432822a.
17. Garrity, P.A., Goodman, M.B., Samuel, A.D., Sengupta, P. Running hot and cold: behavioral strategies, neural circuits, and the molecular machinery for thermotaxis in C. elegans and Drosophila. Genes & Development. 24(21) (2010) 2365–82. doi: 10.1101/gad.1953710.
18. Chuang, H.-S., Chen, H.-Y., Chen, C.-S., Chiu, W.-T. Immobilization of the nematode caenorhabditis elegans with addressable light-induced heat knockdown (ALINK). Lab on a Chip. 13(15) (2013) 2980. doi: 10.1039/c3lc50454a.
19. Zhang, P., Bachman, H., Ozcelik, A., Huang, T.J. Acoustic Microfluidics. Annual Review of Analytical Chemistry. 13(1) (2020) 17–43. doi: 10.1146/annurev-anchem-090919-102205.
20. Nawaz, A.A., Chen, Y., Nama, N., Nissly, R.H.R.H., Ren, L., Ozcelik, A., et al. Acoustofluidic Fluorescence Activated Cell Sorter. Analytical Chemistry. 87(24) (2015) 12051–8. doi: 10.1021/acs.analchem.5b02398.
21. Ozcelik, A., Ahmed, D., Xie, Y., Nama, N., Qu, Z., Nawaz, A.A.A.A., et al. An Acoustofluidic Micromixer via Bubble Inception and Cavitation from Microchannel Sidewalls. Analytical Chemistry. 86(10) (2014) 5083–8. doi: 10.1021/ac5007798.

Hittite Journal of Science and Engineering, 2021, 8 (1) 41–47
ISSN NUMBER: 2148–4171
DOI: 10.17350/HJSE19030000211

Investigation of Full-field and Mean-field Models for Pure Grain Growth Simulations

Betul Aktas[1] **Caner Simsir**[2]
[1]Tampere University, Department of Materials Science Engineering, Tampere, Finland
[2]Middle East Technical University, Department of Metallurgical and Materials Engineering, Ankara, Turkey

ABSTRACT

Mean-field approaches are commonly used in the simulation of grain growth in metals as they are easier to implement. However, mean-field models only track the evolution of average grain diameter as a function of temperature and time, while they neglect the effect of actual grain size distribution, which limits their applicability. Recently introduced full-field models of grain growth – either by level-set and phase field methods- allow to overcome the barriers of mean-field methods, but they are computationally much more demanding. In this article, the main goal is to investigate the applicability of both approaches for the pure grain growth in a solid with an initial Gaussian grain size distribution. The main idea is to keep the average grain size constant while altering the grain size distribution by modifying the standard deviation. DIGIMU software, which uses the level-set approach - is used for this purpose. The conclusion is that full-field models are beneficial to observe changes during grain growth; alternatively, mean-field models deduce approximately the same results as full-field models for a Gaussian distribution within a shorter time. However, it is found that mean-field models overlook certain important stages of the evolution of the microstructure, while full-field method captures all the details. Therefore, the model to investigate the grain growth mechanism should be selected accordingly.

Keywords: Grain growth, Mean-field models, Full-field models, Mean grain size

Article History:
Received: 2020/11/15
Accepted: 2021/03/15
Online: 2021/03/31

***Correspondence to**: Caner Şimşir,*
E-mail: csimsir@metu.edu.tr;
Phone: +90 (312) 210-2520;
Fax: +90 (312) 210-5918.

INTRODUCTION

Grain growth is a phenomenon during which the average grain size gets larger to decrease the total area of grain boundaries to decrease the total energy of the material. Before the grain growth, other mechanisms such as recovery or recrystallization take place to lower the energy; however, further energy decrease is achieved by grain growth at higher temperatures [1]. Change in the grain diameter has a significant effect on the processing and the design of the material due to the fact that material property is affected by grain size [2]. Experts from different backgrounds have studied the change in the material properties like mechanical [3], dielectric [4], and magnetic [5] as a function of grain size over the years. Therefore, much research is going on about the simulation of the growth processes. The easiest growth phenomenon is the pure or ideal grain growth, which does not include other factors such as recrystallization and grain boundary (Smith-Zener) pinning effect [6].

The kinetics of boundary migration must be well understood to study grain growth. Grain boundary migration occurs due to the curved surface of the grains under the existence of an internal pressure. In principle, the migration is towards the center of curvature of grain boundaries. This phenomenon enables the reduction in the overall inner interface and consequently minimizes the overall boundary energy [7]. The kinetics of normal grain growth is generally represented by Eq. (1)

$$\langle R\rangle^2 - \langle R\rangle_0^2 = k.t \quad (1)$$

where t is the time, $\langle R\rangle$ is the average grain radius at t, $\langle R\rangle_0$ is the initial value of $\langle R\rangle$ at t = 0, and k is the kinetic coefficient.

Mathematical models of grain growth allow us to perform simulations. There are many types of grain growth models; however, full-field and mean-field models are the most popular ones. Each model has some drawbacks and conditions that make it useful

for different applications. Mean-field models work with the average values of grain size and overlook the grain size distribution. It means that providing only the average grain sizes to the software is enough to obtain the final average grain sizes. However, full-field models focus on the grain size distribution; therefore, it requires a whole picture of the domain. In terms of reality, full-field methods include more information about the material than the mean-field methods. On the other hand, this high level of detailed information is accompanied by very high computational costs [8]. Calibration of numerical parameters, whose number is also increasing in a 3D study, is another difficult problem to deal with. Due to all these reasons, especially in the computation of 3D models, full-field models have issues waiting to be solved. Some recent progress addresses those issues to prevent obstacles in their industrial use [9] [10]. Furstoss et al. [11] provide a full-field method to simulate grain growth in multiphase materials. Their model can construct transient and steady-state structures based on the level-set approach. After using past experimental data to limit their full-field model, their analyses showed that experimental microstructure morphologies differ from simulated morphologies. Using mean-field and full-field models together, they could predict the mean grain size growth from an experimental peridotite structure.

MATERIAL AND METHODS

DIGIMU® is a software that enables the user to simulate different kinds of phenomena happening in the microstructure. In grain growth simulations, DIGIMU® uses Level Set functions inside the finite element computations. Grain boundaries, interfaces, are defined with the Level Set functions so that each function represents a grain boundary. Level Set function, ψ, can be named as a signed distance function, which is defined in Eq. (2) over a domain Ω. Ω has many sub-domains denoted by G. Distance is calculated as the Euclidean distance, Δ, to the interface, Γ, of sub-domains. In finite element mesh, ψ values are calculated for each node points, and depending on whether $\psi > 0$ or $\psi < 0$, the point is said to lay inside or outside, respectively. Interfaces are also defined by the level set functions in Eq. (3), where the distance to itself is defined as zero.

$$\psi(x,t) = \pm\Delta(x,\Gamma) \tag{2}$$

$$\Gamma(t) = \psi(x,t) = 0 \tag{3}$$

In terms of computational expenses, defining each grain boundary with a level set function is costly. In order to reduce the numerical cost, a coloring technique is used. In this way, grain boundaries that are represented with the same level set function define grains with same colors, only if they are not adjacent. In the end, computational costs are minimized due to the decrease in the total number of level set functions.

In order to determine the grain boundary velocity, $\vec{v}_c$, grain boundary mobility, M_b, should be calculated. Based on simulation time increments, the derivative of distance function, denoted by Δψ, is also used to calculate grain boundary velocity. The equations required to calculate those parameters are given in Eq. (4) and Eq. (5).

$$\vec{v}_c = -M_b \gamma_b \Delta\psi \vec{\nabla}\psi \tag{4}$$

$$M_b(T) = M_0 \exp\left(\frac{-Q_m}{RT}\right) \tag{5}$$

where Q_m is the constant activation energy, M_0 is the mobility pre-exponential factor; and γ_b is the grain boundary energy. Those parameters are material specific and can be found in the material file for Inconel 718, also tabulated in Table 1.

Table 1. Material data of INCONEL 718 for full-field grain growth simulation in DIGIMU. M_0 : mobility pre-exponential factor, Q_m : constant activation energy, γ_b : grain boundary energy (Data is taken from the DIGIMU 3.0 material library.)

M_o (mm⁴/Js)	Q_m (J/mol)	γ_b (J/mm²)
2.981×10^{15}	387000	6×10^{-7}

Mean-field and full-field approaches are investigated by performing two simulations using DIGIMU® 3.0. The main idea is to generate two initial polycrystals having different grain size distributions and the same mean grain size so that it is possible to observe differences between the approaches. Simulations are performed in three stages, pre-processing, computation, and post-processing.

It is known that δ phases precipitate at temperatures lower than 1050-1100 °C [12] and precipitates activate other mechanisms like Zener pinning during the grain growth. Therefore, 1100 °C is suitable as a heat treatment temperature to avoid precipitation since the aim is to demonstrate

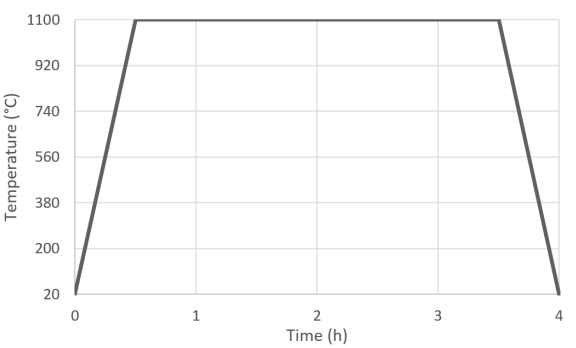

Figure 1. The thermal cycle of the simulations.

pure grain growth. Parameters are defined so that the process lasts 4 hours, a heating step of 1/2 hour between 20 °C and 1100 °C followed by a 3 hours step at this same temperature and then a 1/2 our cooling step between 1100 °C and 20°C. The thermal cycle of the process can be seen in Fig. 1.

Representative elementary volume (RVE) is defined as a square with dimensions 3 mm x 3mm in 2D. The software automatically generated 1139 sites (grains) in RVE. Standard deviations are determined as 5 μm and 15 μm to obtain dissimilar grain size distributions. The mean grain size is decided to be set as 50 μm because it is the typical value for this alloy, which is specified in AMS 5663[13]. The minimum and maximum grain sizes allowed in the initial polycrystals are given together with the above criteria in Table 2.

Table 2. The statistical data to form grain size distributions for each simulation. (GS: Grain Size)

	Min. G.S.	*Max. G.S.*	*Mean G.S*	*Standard Deviation*
Simulation 1	*5 μm*	*90 μm*	*50 μm*	*5 μm*
Simulation 2	*5 μm*	*90 μm*	*50 μm*	*15 μm*

After creating the project file and defining the simulation parameters, the project is launched to compute. Each of the simulations lasted approximately 150 minutes. Results are obtained as microstructural figures and as grain size distribution histograms.

RESULTS AND DISCUSSION

To investigate the grain boundary movement and the grain size alteration, frames at selected times are given in Fig. 2 and Fig. 3, which show distances to grain boundaries from the center of the grains for each simulation. Since distributions are different, starting microstructures are also different from each other. The grains in Simulation 1 when t = 0 s are smaller than in Simulation 2, which was expected before the simulation due to differences in the distributions.

By analyzing the reddish spots, it is easier to detect larger grains in Fig. 2 and Fig. 3. It is possible to visualize any desired grain size by changing the color threshold. It should be noted that the colorization of the grains is performed separately in Simulation 1 and 2. Therefore, the maximum values marked by red color are not the same. The distributions in final microstructures need to be investigated since it is not easy to say how they are different from each other, unlike in the initial microstructure. Therefore, histograms of the grain size distributions are required to be analyzed deeply.

In Fig. 4, progress in Simulation 1 is shown by grain size distributions. It is possible to track the behavior of the distributions during the simulation by making use of these histograms. Since we defined the initial distribution as a normal distribution, the initial histogram (t=0 s) is in a shape similar to a regular bell curve. However, as time passes, grain size distributions deviate from that shape because grains with different sizes are formed more likely than the initial condition.

It is not very easy to follow mean grain size from these histograms; therefore, mean grain sizes are provided on each figure, and it is concluded that mean grain size increases during the simulation as the grain sizes are increasing. Moreover, not only that the mean grain size increases, but also the grain size range enlarges. For instance, the histogram at t = 0 s shows that grain sizes are ranged from 37 μm to 68 μm; while the histogram at t = 14400 s shows the range is from 29 μm to 279 μm. Therefore, the probability of observing larger grains increases as time passes.

In Simulation 2, a similar change in the histograms is seen in Fig. 5. It starts with a normal distribution, deviates from bell-shaped as time passes. The range of the grain sizes again increases during the simulation. In the beginning, grain sizes are ranged from 16 μm to 83 μm. In the end, this range enlarges to 19 μm - 292 μm. Therefore, larger grains are likely to be found in the structure as time passes.

Initial distribution can be generated with higher non-uniformity in terms of grain size by keeping the mean grain size constant and increasing the standard deviation of the initial polycrystal grain size distribution, as concluded in Fig. 4 and Fig. 5. Even from the first step at t = 0s, grain sizes are allowed to exist in a broader range in Fig. 5 than that in Fig.4 (from 37 μm - 68 μm to 16 μm - 83 μm). Likewise, following the same trend, one can say that at t = 14400 s, the grain size allowance range would be higher in Fig. 5 than that in Fig.4. It can be confirmed with the increase in the range from 19 μm - 292 μm to 29 μm - 279 μm.

In order to track mean grain size during the simulation, all the frames were analyzed and Fig. 6 is obtained. The increase in mean grain size during the simulations was expected since grains are getting larger. The heat treatment cycle can also be seen on the same figure to track the relation between the temperature and growth. The increase in the temperature affects grain growth since the grain boundary mobility is affected by temperature. Up to around 1000 °C, average grain size is not changing because the temperature is not enough to activate grain growth. After that point on, grain growth accelerates and the average grain size visibly increases. At t = 12600 s, when the cooling starts, growth is completed because the grain boundary mobility is too low due to the absence of heat. The mean grain sizes at the end of each simulation are given in Table 3.

The main goal of these simulations is to determine

the differences between mean-field and full-field models by carrying out two full-field model based simulations. It can be easily seen in Fig. 6 that both simulations reached approximately the same mean grain size at the end (Table 3). The slight difference is calculated as 1.7 μm. Therefore, mean and full-field models reach similar results by means of average grain size. However, the paths that simulations followed are a bit more different from each other. The maximum difference in the mean grain sizes between the simulations reached at t = 4400 s, and the difference is 13.25 μm, which is a non-negligible difference. This difference can be calculated since the full-field approach provides the advantage of tracking mean grain size evolution throughout the simulation, unlike the mean-field approach. Even though mean field approach provides promising results for the final mean grain size, it cannot predict the grain size distribution and the evolution of mean grain size during the simulation. Therefore, a full-field approach should be used if the investigation aims to examine the structure of the material while the grain growth is operating. In other words, mean-field approaches can only provide final mean grain sizes, but it is not useful to determine the grain size distribution.

Table 3. Final mean grain size for each simulation and differences between mean grain sizes

	Simulation 1	*Simulation 2*
Final mean grain size	*130.4 μm*	*132.1 μm*
Final difference in the mean grain sizes	*1.7 μm*	
Maximum difference in the mean grain sizes	*13.25 μm*	

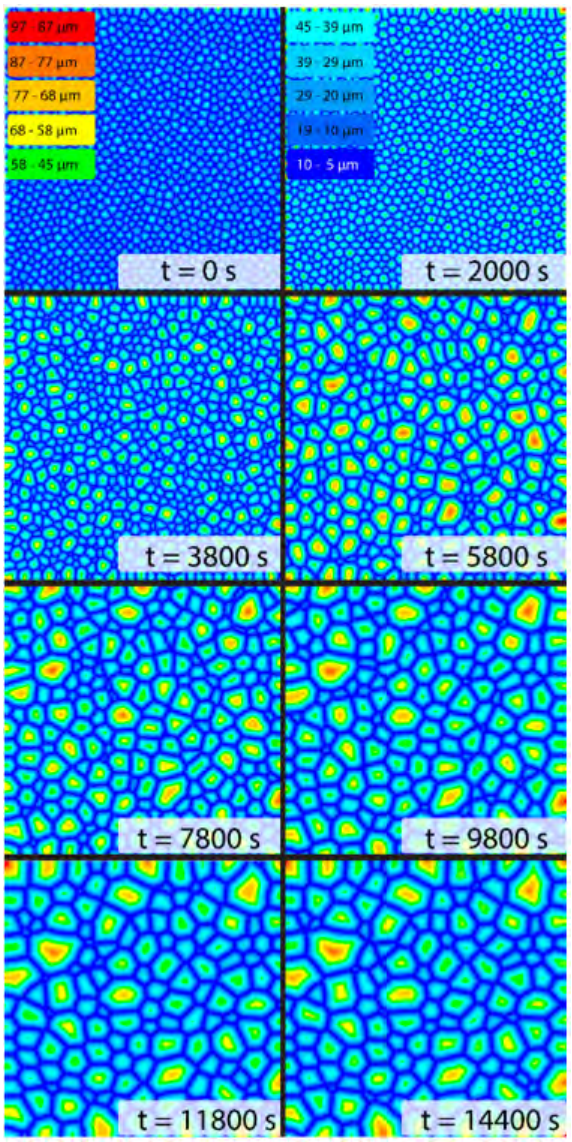

Figure 2. Distances to grain boundaries from the centers of the grains in Simulation 1.

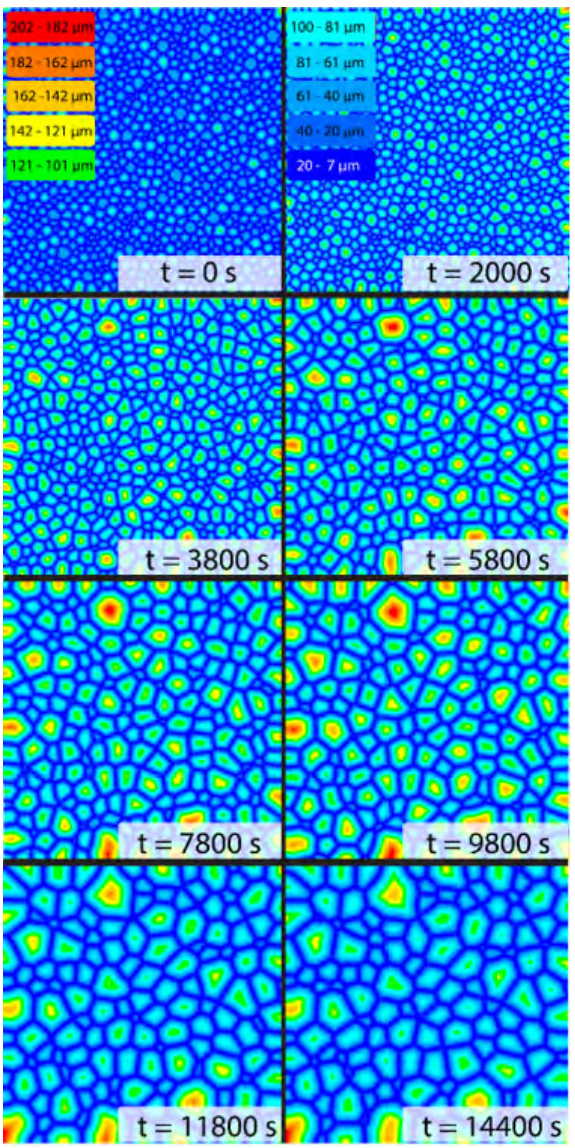

Figure 3. Distances to grain boundaries from the centers of the grains in Simulation 2.

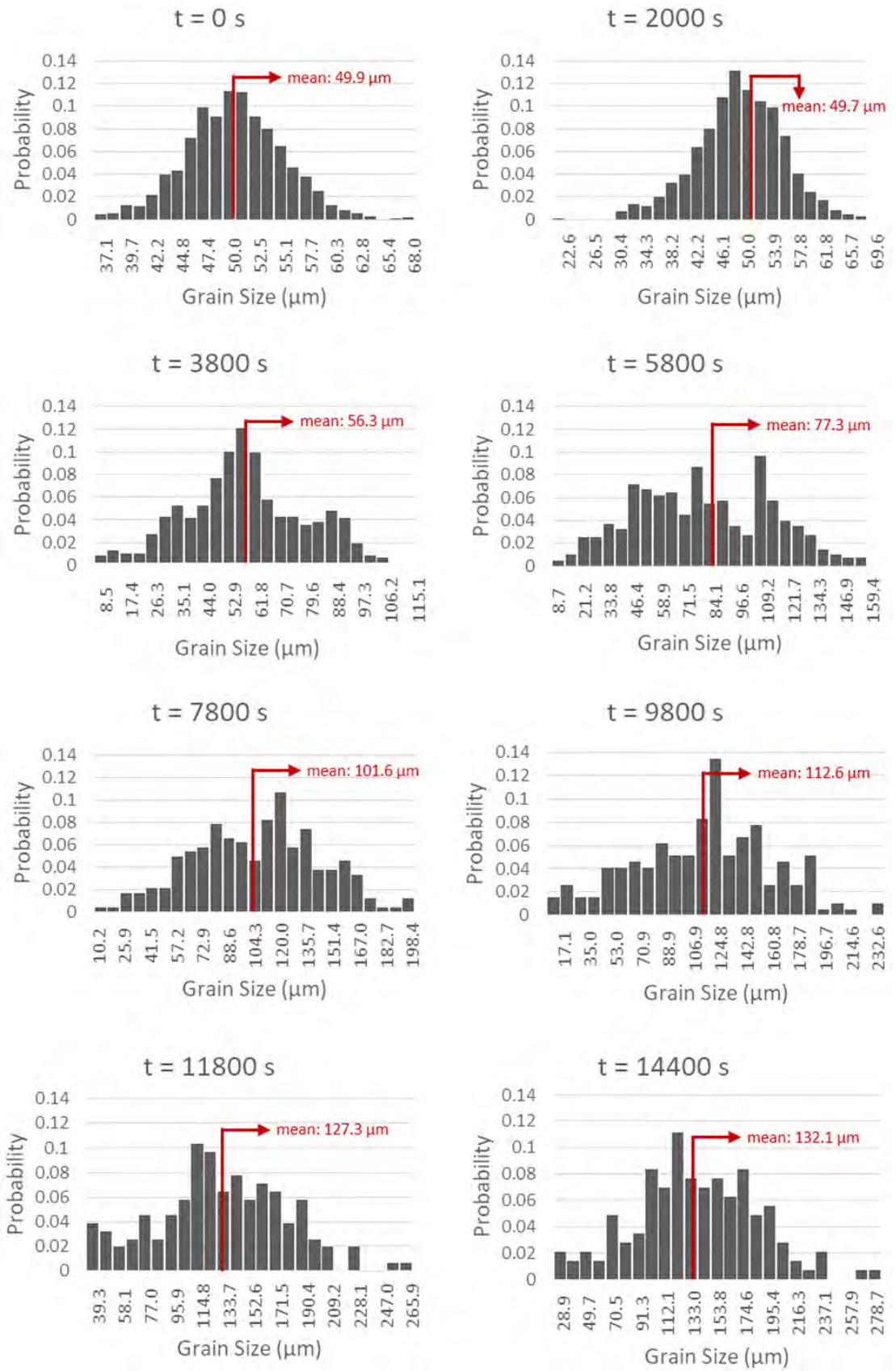

Figure 4. Grain size distribution throughout the Simulation 1.

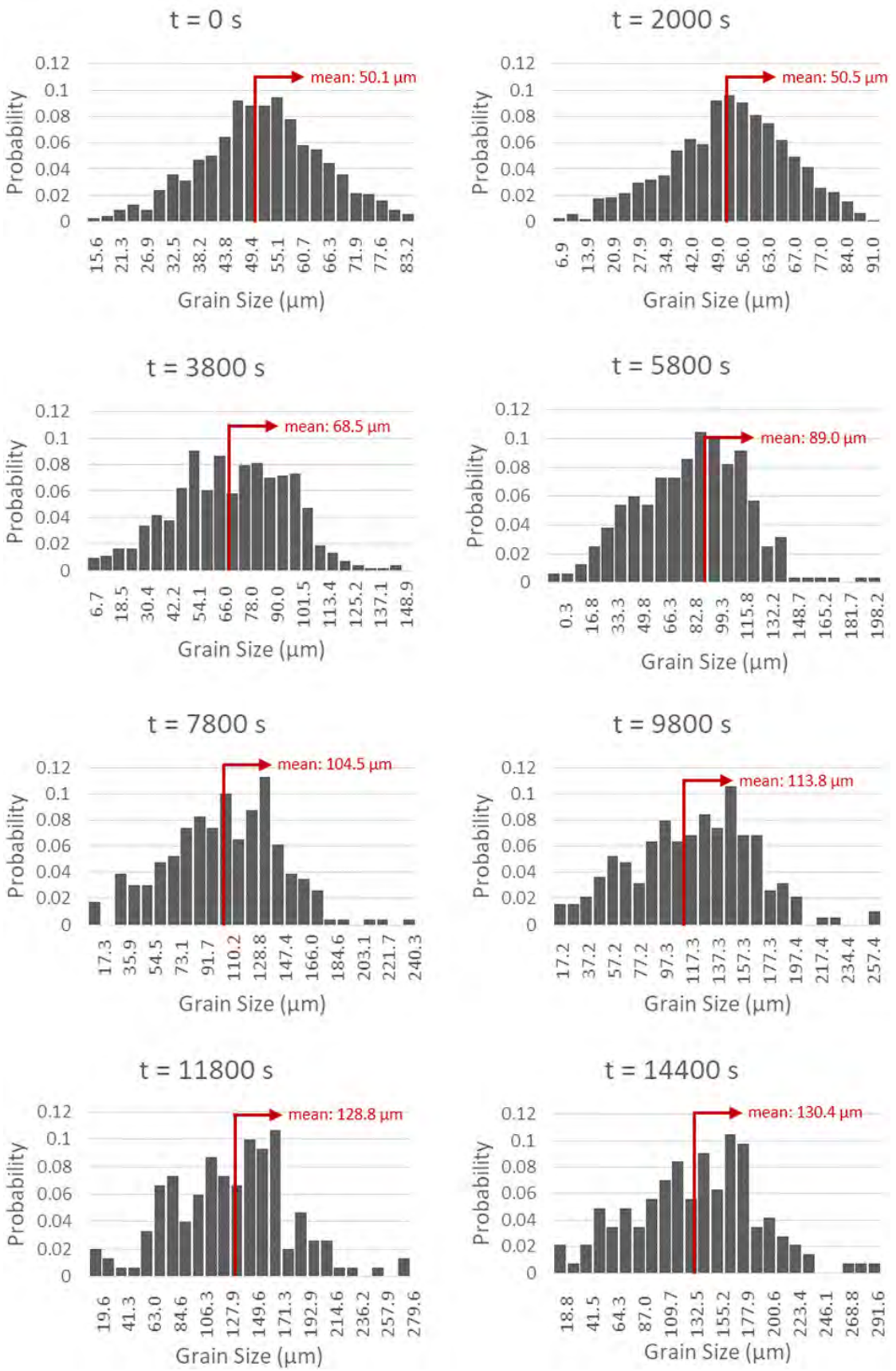

Figure 5. Grain size distribution throughout the Simulation 2.

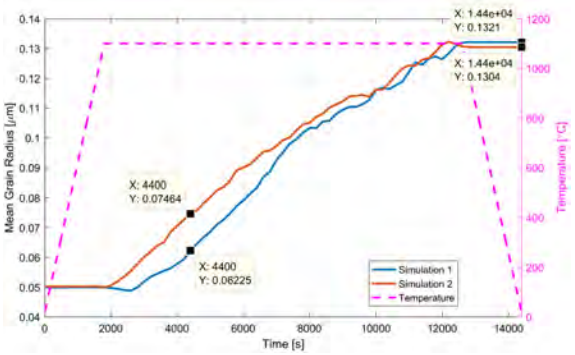

Figure 6. The change in the mean grain size during the simulations.

CONCLUSION

Investigation of the grain growth mechanism has been studied over the years due to the fact that change in the grain size has a huge impact on the material property. Some models relying on different backgrounds have been developed, such as mean-field and full-field models. Mean-field models give information about final mean grain size, whereas full-field models focus on the grain size distribution and the evolution of mean grain size as well. In this article, we examined the differences in those models for pure grain growth simulation by carrying out two simulations using DIGIMU® 3.0 software that works with the full-field approach. For two simulations, different grain size distributions were generated by keeping the mean grain size constant while changing the standard deviation. If we use the mean-field models instead, we could already expect that the final mean grain sizes will be the same since we provide equal initial mean grain sizes. However, we also provide the grain size distribution, which makes two microstructures differ from each other. Therefore, we could track the grain size distribution during the grain growth thanks to the full-field approach. The main idea is to check the reliability of the mean-field model by investigating it from a wider window. At the end of the simulations, we found the final mean grain sizes are slightly different from each other, which proves the mean-field models are reliable are applicable to yield similar results with a full-field model while providing lower time consumption. However, simulations are following different paths during grain growth. However, it should be noted that mean-field models won`t be applicable to multi-model grain size distributions and abnormal grain growth predictions. Therefore, the model should be selected according to the goal of the simulation.

ACKNOWLEDGEMENT

The author wish to thank Anıl Hatiboğlu (Middle East Technical University) for his enormous support on processing the simulation data.

References

1. Raabe, D. Recovery and Recrystallization: Phenomena, Physics, Models, Simulation, Editor(s): David E. Laughlin, Kazuhiro Hono, Physical Metallurgy (Fifth Edition), Elsevier, 2014, Pages 2291–2397, ISBN 9780444537706, https://doi.org/10.1016/B978-0-444-53770-6.00023-X.
2. Atkinson, H. V. (1988). Overview no. 65: Theories of normal grain growth in pure single phase systems. Acta Metallurgica, 36(3), 469–491. 3. Strunk JrW, White EB. The Elements of Style, fourth ed. Longman, New York, 2000.
3. Goussery, V., Bienvenu, Y., Forest, S., Gourgues, A., Colin, C., & Bartout, J. (2004). Grain size effects on the mechanical behavior of open–cell nickel foams. Advanced Engineering Materials, 6(6), 432–439. https://doi.org/10.1002/adem.200405153
4. Kahn, M. (1971). Influence of grain growth on dielectric properties of NB–doped BaTiO3. Journal of the American Ceramic Society, 54(9), 455–457. https://doi.org/10.1111/j.1151–2916.1971.tb12384.x
5. M.M. Syazwan, A.N. Hapishah, R.S. Azis, Z. Abbas, M.N. Hamidon, Grain growth effects on magnetic properties of Ni0.6Zn0.4Fe2O4 material prepared using mechanically alloyed nanoparticles, Results in Physics, Volume 9, 2018, Pages 842–850, ISSN 2211–3797, https://doi.org/10.1016/j.rinp.2018.03.054.
6. Miyoshi, E., Takaki, T., Ohno, M., Shibuta, Y., Sakane, S., Shimokawabe, T., & Aoki, T. (2017). Ultra–large–scale phase–field simulation study of ideal grain growth. NPJ Computational Materials, 3(1), 1–6
7. Kim, B. N., Hiraga, K., & Morita, K. (2003). Kinetics of normal grain growth depending on the size distribution of small grains. Materials transactions, 44(11), 2239–2244.
8. Maire, L., Scholtes, B., Moussa, C. et al. Improvement of 3D mean field models for capillarity–driven grain growth based on full field simulations. J Mater Sci 51, 10970–10981 (2016). https://doi.org/10.1007/s10853–016–0309–6
9. Scholtes, B., Settefrati, A., Bozzolo, N., Perchat, E., Chenot, J. L., & Bernacki, M. (2016, July). Large scale FE simulations of recrystallization and grain growth thanks to a level set approach, illustrations in context of industrial forming processes. NUMIFORM 2016: The 12th International Conference on Numerical Methods in Industrial Forming Processes, The Minerals, Metals & Materials Society, Troyes, France. (hal–01421648)
10. Scholtes, B., Shakoor, M., Settefrati, A., Bouchard, P., Bozzolo, N., & Bernacki, M. (2015). New finite element developments for the full field modeling of microstructural evolutions using the level–set method. Computational Materials Science, 109, 388–398. https://doi.org/10.1016/j.commatsci.2015.07.042
11. Furstoss, J., Bernacki, M., Petit, C., Fausty, J., Pino–Mu~noz, D., & Ganino, C. (2020). Full field and mean field modeling of grain growth in a multiphase material under dry conditions: application to peridotites. Journal of Geophysical Research: Solid Earth, e53942.
12. Mahadevan, S., Nalawade, S., Singh, J. B., Verma, A., Paul, B., & Ramaswamy, K. (2012). Evolution of δ Phase Microstructure in Alloy 718. Superalloy 718 and Derivatives, 737–750.
13. SAE International in United States, September 1965, [Aerospace Material Specification] AMS5663.

Hittite Journal of Science and Engineering, 2021, 8 (1) 49–53
ISSN NUMBER: 2148–4171
DOI: 10.17350/HJSE19030000212

Bioactivity Screening of Marine and Terrestrial Derived Fungi From Antarctica

Bulent Gozcelioglu
Scientific and Technological Research Institution of Turkey, Ankara, Turkey

ABSTRACT

The Antarctic region is situated in the Southern Hemisphere. The weather in Antarctica can often change dramatically in a short span of time. Due to these sudden changes the organisms and microorganisms which live in Antarctica produce unique metabolites to survive. In the present trial, the marine derived fungi from Antarctica's coast were researched for their antimicrobial activity. The disk diffusion technique was used to determined antimicrobial activity of isolated marine-derived fungi extracts. According to the obtained results the Penicillium chrysogenum and P. crustosum extracts were shown higher antibacterial against Gram positive and Gram negative rather than other extracts. In conclusion, marine derived fungi from Antarctica region produce the structurally novel and interesting bioactive compounds. Some of these fungi species such as Penicillium species are known to produce antimicrobial metabolites, the results obtained in this study also showed that Penicillium species show higher antimicrobial activity than the other species.

Keywords:
Antarctica, Antimicrobial activity, Live sources-derived fungi.

Article History:
Received: 2021/01/08
Accepted: 2021/03/08
Online: 2021/03/31

***Correspondence to**: Bulent Gozcelioglu, Scientific and Technological Research Institution of Turkey, 06420, Ankara, Turkey*
E-Mail: bulent.gozcelioglu@gmail.com

INTRODUCTION

Marine living organism as sponges, tunicates corals and algae are productive sources of biologically active compounds used in the cosmetic and pharmaceutical industries. In addition, marine microorganisms also are abundant microbial committee of marine ecosystem varying from coast to deep sea. The bioactive compounds which produce by marine derived microorganisms are still largely unexplored and unexploited [1]. Marine microorganisms have an enormous capacity to produce different metabolites to sense and respond to their stressful environment. Some of these metabolites used as a pharmaceutical agent in the intervention of various human diseases [2]. Marine microorganisms due to their spacious genetic, metabolite diversity and wide spectrum of bioactivities including antibacterial, antifungal [3], antidiabetic [4], anti-inflammatory [5], antiprotozoal [6], anti-tuberculosis [7], antiviral [8], antitumor, and cytotoxic activities [9] become an interesting source for researchers. In our on-going search for biologically active metabolites from marine microorganisms, some marine derived fungi were collected from oceans and regional seas around Antarctica. Marine microorganisms for surviving in the harsh environmental conditions of Antarctica must develop different strategy such as produce various metabolites which may have a bioactive potential [10]. In this study, nine marine derived fungi were isolated from different marine organisms. All isolated fungi were identified and tested for their antimicrobial activities.

MATERIALS AND METHODS

General

The sea salts were bought from Sigma Aldrich, sabouraud 4% dextrose agar (SDA), mullerhintonbroth, sabourauddextrose broth andethyl acetate was purchased from Merck. Nutrient agar was prepared from Oxide. Millipore Membrane Filter (MA 01730, USA). Biospeedy® Fungal Diversity Kit was prepared from Bioeksen Turkey.

Figure 1. The process of isolation and bioactivity screening of marine derived fungi.

Isolation of Marine-Derived Fung

Marine samples were collected oceans and regional seas around Antarctica in April 2018. Marine organisms were collected by scuba diving and then transferred to containers. The fungi isolation was process immediately to prevent the growth of bacteria in the culture medium. According to the Kjer et al. 2010, The samples were cut in 1 × 1 cm and was cleaned down 3 multiplication with sterile water to remove superficies residues and for sterilization it was dunked in EtOH 70% (Volume/Volume) for 60–120 seconds. Then the samples were dried and relocated to culture medium (SDA and artificial sea salt). The culture mediums were kept for 5-7 daylight in 25˚C. The fungi samples were stored at -70˚C for further analysis [11].

Identification of Fungi

Fungi strains were identified by DNA isolation using a fungi DNA isolation and PCR-based Biospeedy® fungi Diversity Kit. The sequences of the fungi amplicons were identified by the ABI Prism BigDye Terminator Cycle Sequencing Ready Reaction Kit using ABI Prism 377 DNA Sequencer [11, 12].

Preparation of fungi extracts

For preparative scale production of fungus extracts was carried out in 2 L erlenmeyer flasks contained sterilized rice and artificial sea salt medium, fungi strains were grown up in 4-6 weeks at 25˚C. The fungi strains were extracted by EtOAc by maceration, the obtained EtOAc extracts were dried under vacuum and kept at 4 ˚C until use [13].

Antimicrobial activity

The stock solutions of samples extract (100 µg/mL) were prepared in dimethyl sulphoxide. The solution was sterilized by Millipore Membrane Filter (0.22 µm pore size 47 mm diameter).

Staphylococcus epidermidis (ATCC 35984), *Bacillus subtilis* (ATCC 6633), *Bacillus cereus* (ATCC 14579) used as Gram-positive bacteria; *Escherichia coli* (ATCC 25922), *Proteus vulgaris* (ATCC 8427), and *Enterobacter aerogene* (ATCC 13048) used as Gram-negative bacteria strains. Furthermore, *Candida albicans* (ATCC 10231) and *Candida tropicalis* (ATCC 1308) used as yeast strains. All bacterial and yeast strains were employed for antimicrobial screening with taking CLSI recommendations into account by disk diffusion method for the antifungal and antibacterial activity of extracts [14]. The fresh grown bacteria and yeast strains were cultured in nutrient broth and sabouraud dextrose broth respectively. The culture mediums were set in a humid chamber and incubated at 35°C, 24 hours for the bacteria and at 30 °C, 48 hours for yeasts. Transfer growth into broth and incubate broth for 18-hour until the visible turbidity is equal to the 0.5 McFarland. Muller hinton agar was prepared and terile paper disks (6 mm) were set onto the inoculated agar surface and 50 µL (100 µg/mL) of each extract were added to the paper disk. The plates were incubated for 22 h at 37°C. The results were obtained by measuring the inhibition zone diameter.

RESULTS

Marine species which listed in Table 1 were collected from different coasts of Antarctica. Nine fungi species were isolated and identified from marine samples. All isolated fungi strains are shown in Table 1 and Fig. 2. The fungi strains were isolated from algae, lichen, sponge and sediment samples. All the samples were collected from Antarctica region.

The EtOAc extracts of the isolated fungi were prepared. The antimicrobial activity of fungi extracts was determined by disk diffusion assay. The results were obtained by measuring from the center of the extract disk to a point on the circumference of the zone where a distinct edge is present. Antimicrobial values are reported in millimeters and shown in Table 2, Fig. 3 and 4.

Table 1. UTM Coordinates of Point Transect Locations

Origin	*Fungi species*
Himantothallus grandifolius (Algae)	*Penicillium chrysogenum*
Desmarestia antarctica (Algae)	*Penicillium crustosum*
Gigartina skottsbergii (Algae)	*Cladosporium sp.*
Monostroma hariotii (Algae)	*Botrytis sp.*
Sediment	*Ulocladium microsporum*
Umbilicaria antarctica (Lichen)	*Alternaria alternata*
Anoxycalyx joubini (Sponge)	*Aspergillus awamori*
Usnea antarctica (Lichen)	*Alternaria malorum*
Usnea antarctica (Lichen)	*Cladosporium malorum*

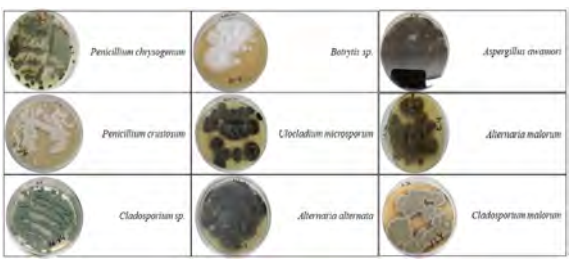

Figure 2. Obtained fungi strains from marine species

Table 2. Antimicrobial activity of fungal strains from marine species

Fungi \ Bacterial strains	Zone of inhibition (mm)					
	S. epidermidis	*B. cereus*	*B. subtilis*	*E. aerogenes*	*P. vulgaris*	*E. coli*
Penicillium chrysogenum	17	-	20	16	25	14
Penicillium crustosum	15	14	19	23	13	10
Cladosporium sp.	-	-	-	13	-	-
Botrytis sp.	-	-	-	-	-	-
Ulocladium microsporum	27	30	15	-	-	-
Alternaria alternata	11	10	-	12	-	-
Aspergillus awamori	16	-	20	-	-	-
Alternaria malorum	26	15	24	-	-	11
Cladosporium malorum	20	15	15	-	20	-

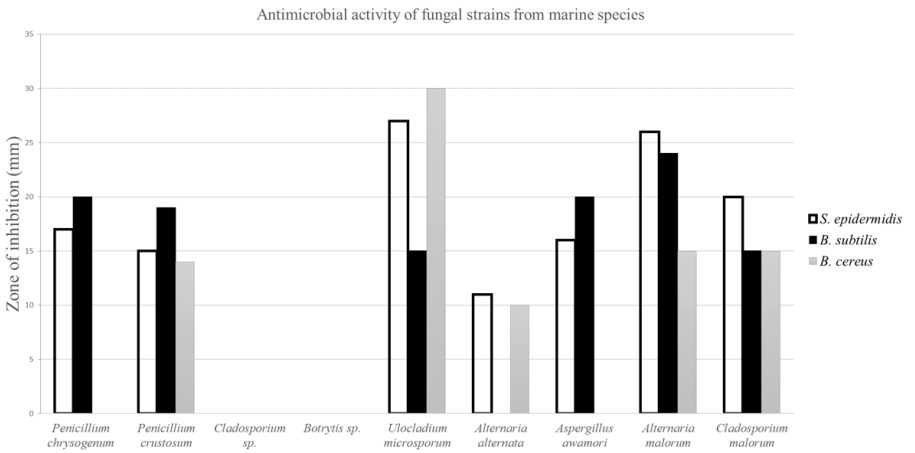

Figure 3. Antimicrobial activity of fungal strains against S. epidermidis, B. cereus, B. subtilis

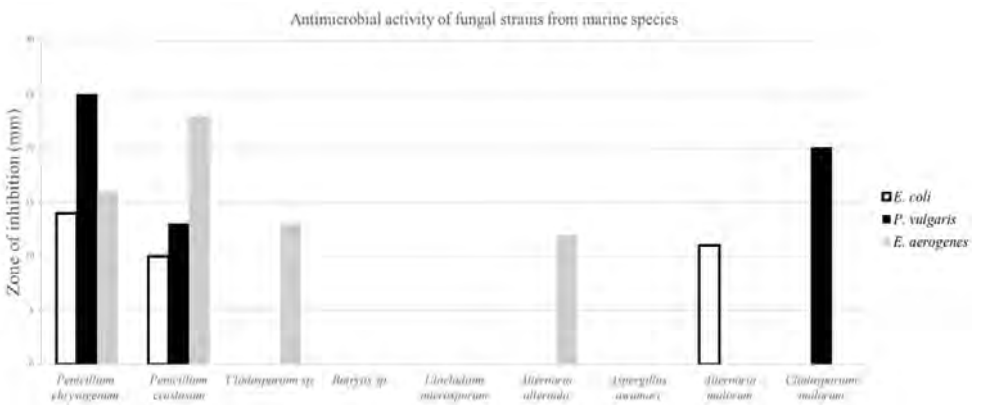

Figure 4. Antimicrobial activity of fungal strains against E.coli, P. vulgaris, E. aerogenes

DISCUSSION

Infectious diseases claim numerous lives worldwide every year, and many of these infections have been increased many-fold due to prolonged illness caused by widespread drug resistant pathogens. Every year, the drug-resistant pathogens are increasing, and finding new antimicrobial sources is considerable [15]. The study about marine organisms and marine derived microorganisms has been studied over the past few years. The marine derived microorganisms of Antarctica environments are an efficient field for unique bioactive secondary metabolites. Accor-

ding to the harsh condition of Antarctica, marine derived fungi from this region produce the structurally novel and interesting bioactive compounds. As previous studies, so many biologically active compounds were isolated from unicellular bacteria, actinomycetes, fungi, lichens, mosses, bryozoans, cnidarians, echinoderms, molluscs, sponges and tunicates which collected from Antarctica region. Some of the isolated compounds were shown different activity such as cytotoxic, antioxidant, antimicrobial, anti-angiogenesis, neuroprotective, NF-κB inhibitory, antiparasitic and antiviral activities [16]. In this study some marine derived fungi from Antarctica coasts were investigated for their antimicrobial potential. According to the obtained results some of these fungi extracts displayed significant antimicrobial activity. According to the antimicrobial results, none of the fungi extracts did show antifungal activity against *Candida albicans* and *Candida tropicalis*. Also, Botrytis sp. was not active against tested bacterial strains. *Penicillium crustosum* extract was active against all tested bacterial strains. Among all extracts *U. microsporum* extract was shown highest activity against Gram positive strains rather than other obtained extracts. *P. chrysogenum* and *P. crustosum* were shown highest activity against Gram negative strains rather than other obtained extracts. *Penicillium* species are known to produce antimicrobial metabolites in previous studies, and the results obtained in this study also showed that *Penicillium* species show higher antimicrobial activity [17, 18]. According to the previous studies and this work different fungi species show different antimicrobial activity, withal the same fungi species from different region also show dissimilar activity. This result is not uncommon, this steams from the secondary metabolites which produce by fungi. Numerous studies have shown that the Antarctic fungi have produced a wide range of bioactive metabolites and it is very important to discover these active metabolites and clear their activity [19, 20].

CONCLUSION

In conclusion, in this study, nine fungi were isolated from marine species collected from Antarctica coasts. This study is a preview study to discover more active fungi species and serves as a guide for future studies. Consequently, these extracts originated from the marine-derived fungi sources need further investigation with a view to identifying the active components that could be developed as potential drugs to be used against diseases threatening human health.

ACKNOWLEDGEMENT

I would like to thank Presidency of the Republic of Turkey, under the responsibility of the Ministry of Science, Industry, and Technology of the Republic of Turkey, in coordination with the Istanbul Technical University Polar Research and Application and Research Centre.

References

1. Corinaldesi C, Barone G, Marcellini F, Dell'Anno A, Danovaro R. Marine Microbial-Derived Molecules and Their Potential Use in Cosmeceutical and Cosmetic Products. Marine Drugs 15 (2017) 118- 139.
2. Tripathi VC, Horam S, Singh A, Lata M, Reddy TJ, Arockiaraj J. Pasupuleti M. The diskovery of antioxidants in marine microorganisms and their protective effects on the hepatic cells from chemical-induced oxidative stress. Free Radical Research 54 (2020)150–161.
3. Karpiński TM. Marine Macrolides with Antibacterial and/or Antifungal Activity. Marine Drugs 17 (2019) 241- 265.
4. El-Hady FKA, Abdel-Aziz MS, Abdou AM, Shaker KH, Ibrahim LS, El-Shahid ZA. In vitro Anti-diabetic and Cytotoxic Effect of the Coral Derived Fungus (Emericella unguis 8429) on Human Colon, Liver, Breast and Cervical carcinoma cell lines. International Journal of Pharmaceutical Sciences Review and Research 27 (2014) 296-301.
5. Xu J, Yi M, Ding L, He S. A Review of Anti-Inflammatory Compounds from Marine Fungi, 2000-2018. Marine Drugs 17 (2019) 636- 660.
6. Pontius A, Krick A, Kehraus S, Brun R, König GM. Antiprotozoal activities of heterocyclic-substituted xanthones from the marine-derived fungus Chaetomium sp. Journal of Natural Product 71 (2008)1579-1584.
7. Luo X, Zhou X, Lin X, Qin X, Zhang T, Wang J, Tu Z, Yang B, Liao S, Tian Y. Antituberculosis compounds from a deep-sea-derived fungus Aspergillus sp. Natural Product Research 31 (2017)1958-1962.
8. Moghadamtousi SZ, Nikzad S, Kadir HA, Abubakar S, Zandi K. Potential Antiviral Agents from Marine Fungi: An Overview. Marine Drugs13 (2015) 4520-4538.
9. Ramos AA, Preta-Sena M, Castro-Carvalho B, Dethoup T, Buttachon S, Kijjoa A, Rocha E. Potential of four marine-derived fungi extracts as anti-proliferative and cell death-inducing agents in seven human cancer cell lines. Asian Pacific Journal of Tropical Medicine 8(2015) 798-806.
10. Chavez R. Bioactive Compounds Produced by Antarctic Filamentous Fungi. Fungi of Antarctica (pp.265-283), 2019.
11. Gözcelioğlu B. Antioxidant and cytotoxic activity of three Turkish marine-derived fungi. Turkish Journal of Biochemistry. 44 (2019) 554–559.
12. Sun Y, Cai Y, Huse SM, Knight R, Farmerie WG, Mai V. A large-scale benchmark study of existing algorithms for taxonomy-independent microbial community analysis. Brief Bioinform.13 (2011) 107- 121.
13. Kjer J, Debbab A, Aly AH, Proksch P. Methods for isolation of marine-derived endophytic fungi and their bioactive secondary products. Nature Protocols 5 (2010) 479-490.
14. CLSI. Methods for Dilution Antimicrobial Susceptibilit Tests f or Bacteria That Grow Aerobically; Approved St andard 9th Edition. CLSI document M07-A9. Wayne, PA: Clinical and Laboratory Standards Institute; 2012.
15. Mondol MA, Shin HJ. Antibacterial and antiyeast compounds from marine-derived bacteria. Marine Drugs. 12(2014) 2913-2921.
16. Tian Y, Li YL, Zhao FC. Secondary Metabolites from Polar

Organisms. Marine Drugs. 15(2017) 28-58.
17. Yang MH, Li TX, Wang Y, Liu RH, Luo J, Kong LY. Antimicrobial metabolites from the plant endophytic fungus Penicillium sp. Fitoterapia. 116 (2017) 72–76.
18. Gharaei-Fathabad E, Tajick-Ghanbary MA, Shahrokhi N. Antimicrobial Properties of Penicillium Species Isolated from Agricultural Soils of Northern Iran. Research Journal of Toxins, 6 (2014) 1-7.
19. Henríquez M, Vergara K, Norambuena J, Beiza, A, Maza F, Ubilla P, Araya I, Cha´vez R, San-Martı´n A, Darias J, Darias M, Vaca, I. Diversity of cultivable fungi associated with Antarctic marine sponges and screening for their antimicrobial, antitumoral and antioxidant potential. World Journal of Microbiology and Biotechnology, 30(2013) 65–76.
20. Albores S, Sanguiñedo P, Held BH, Cerdeiras MP, Blanchette RA. Biodiversity and antimicrobial activity of Antarctic fungi from the Fildes Peninsula, King George Island. Sydowia 70 (2018) 185-191.

Hittite Journal of Science and Engineering, 2021, 8 (1) 55–62
ISSN NUMBER: 2148–4171
DOI: 10.17350/HJSE19030000213

Production of Value-Added Bioproducts Using a Modified Continuous Biofilm Reactor by *Citrobacter Freundii* DSM 15979

Mine Gungormusler
Izmir University of Economics, Department of Bioengineering, Izmir, Turkey
Izmir University of Economics, Department of Genetics and Bioengineering, Izmir, Turkey

ABSTRACT

The present paper reports the ability of Citrobacter freundii, strain DSM 15979, to produce value-added chemicals from biodiesel derived glycerol in a mesophilic modified continuous biofilm reactor operating under mesophilic continuous conditions at a specified hydraulic retention time (HRT). Increasing initial glycerol concentrations (G_{in}) (10 to 144 g/L) were tested in order to evaluate their effects on simultaneous production of value-added products with immobilized whole cells. Initial glycerol concentration was found to be a significant independent variable for the productions of 1,3-PDO, 2,3-BD, ethanol, acetic, succinic and lactic acids under different organic loading rates (OLR). The major end-products in the metabolic pathway were found to be 1,3-PDO and 2,3-BD. They reached maximum values of 26.1 g/L and 18.8 g/L at 92 g/L of initial crude glycerol feeding, which represents an OLR of 11.5 g/L.h. These results suggest that the formation of biofilms were beneficial for the utilization of high substrate concentrations, thus, the employment of immobilized cells of *C. freundii* DSM 15979 in a modified continuous biofilms reactor is favorable for mixed glycerol fermentations.

Keywords: Glycerol fermentation, Biofilm, *Citrobacter freundii*

Article History:
Received: 2020/12/30
Accepted: 2021/02/24
Online: 2021/03/31

Correspondence to: *Mine Güngörmüşler,*
E-mail: mine.gungormusler@ieu.edu.tr;
Phone: +90 232 488 8392

INTRODUCTION

Commodity chemicals are derived largely from raw materials based on fossil resources. The environmentally friendly biotechnological approaches potentially form same or functionally similar chemicals from sustainable materials. In addition, their effects on reduction in greenhouse gas emissions provide an additional advantage. Various industrial by-products and domestic waste materials can be used as raw materials to convert into value-added chemicals by means of fermentative pathways. Numerous studies reported the technical viability of valorization of biodiesel driven glycerol into 1,3-PDO, 2,3-BD, ethanol, butanol, H2, acetic acid, lactic acid and other organic acids (Fig. 1). The versatility of the final by-product of this conversion is due to the utilization of different metabolic pathways by numerous species including *Klebsiella pneumoniae* [1], *Citrobacter freundii* [2–6], *Pantoea agglomerans* [7], *Entrobacter aerogenes* [8], *Lactobacillus brevis* [9], *Lactobacillus diolivorans* [10], *Lactobacillus reuteri* [11], *Clostridium butyricum* [12], *Clostridium perfringens* [13], *Clostridium acetobutylicum* [14], *Clostridium pasteurianum* [15], and *Clostridium beijerinckii* [16]. The major end-products from the glycerol fermentation can be integrated to a wide variety of applications such as 1,3-PDO in the manufacturing of polyesters, polyethers, polyurethanes, polytrimethylene-terephthalate, textiles, carpets and plastics [17]; 2,3-BD in the manufacturing of printing inks, jet fuels, explosives, perfumes, foods, pharmaceuticals, and plasticizers [18], and acetic acid mainly as a solvent [19]. The beneficial properties of these chemicals characterize them as special commodity chemicals attributing important roles in industrial processes.

Glycerol can be metabolized by two main reactions including one reductive branch in which at first it is dehydrated to 3-hydroxypropionaldehyde and water, it is then reduced to 1,3-PDO under the utilization of the reducing power nicotinamide adenine dinucleotide (NADH) and an oxidative branch where the required reducing power is formed resulting in the formation of metabolites demonstrated in Fig. 1 [2, 20].

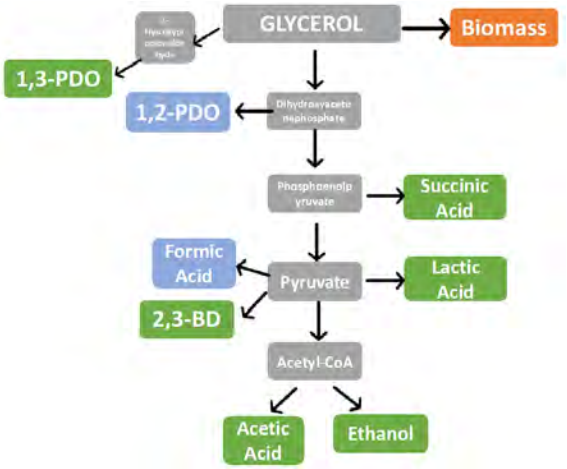

Figure 1. Main metabolites produced in the glycerol degradation pathways of Enterobacteriaceae, adapted from [2].

Several strategies have been employed for glycerol conversion with high yields of bioproducts [20] such as optimization of the fermentation medium [21] and operational parameters [22], employing different reactor configurations, applying fed-batch productions [23] to prevent the inhibitions of high initial substrate concentrations and end-products, and metabolic engineering [24]. Apart from these, one of the main approaches include increasing the final product concentrations with the help of high cell densities [25]. In this regard, immobilization is the key mode of action to enhance productivities. During this process microorganisms form biofilms without the involvement of chemicals and thick layers of cells are generated by either on attaching to materials or naturally on surfaces or they are entrapped [26]. In a study by Paranhos and Silva [27] a continuous anaerobic fluidized bed reactor (AFBR) was used to optimize the productions of H2, 1,3-PDO and propionic acid from crude glycerol with the formation of biofilms of mixed cultures indicating the effectiveness of immobilization on productivities [27]. Another report on the production similarly by the utilization of an anaerobic sludge also reported the ability of the microorganisms to stabilize under elevating OLR (25 to 62.5 g/L.d) with the help of granulation of cells [28].

As reported previously, several strains and isolates of *C. freundii* have been studied in the literature with different parameters. Whereas, the fluidized bed biofilm reactor was used for the first time in the literature with increasing crude glycerol concentrations in a chemostat providing the novelty of the work. The aim of the study was to investigate the effectiveness of the utilization of a modified fluidized bed biofilm reactor (MCBR) to produce value-added biochemicals from crude glycerol by *C. freundii* DSM 15979. Accordingly, the effects of glycerol concentration feed on the crude glycerol driven productions of 1,3-PDO, 2,3-BD, lactic and acetic acids and the influence of the OLR in the MCBR by *C. freundii* DSM 15979 was comparatively studied for the first time in the literature. The results of the present study reports the advantages of the formation of biofilms to enhance the yields of final products at increasing OLRs.

MATERIAL AND METHODS

Experimental Set-up and Biofilm Reactor Conditions

A Pyrex® glass bioreactor (Corning Inc., USA) was employed for the fluidized bed biofilm reactor studies. The bioreactor had the following specifications: 15 cm height with an i.d. of 10 cm and 8 outlets for feed and gas connections. The total volume and working volume of the of the bioreactor were 1000 mL and 320 mL, respectively. Ceramic supports were added to the bioreactor as the immobilization material. The ceramic supports were decontaminated by distilled water followed by an overnight drying procedure at 105°C, prior to application.

The temperature in the bioreactor was kept at 30°C using a hot plate magnetic stirrer (MR Hei-Standard, Heidolph, Germany) and monitored by an external thermal probe (EKT Hei-Con, Heidolph, Germany). One peristaltic pump for inlet feeding and one peristaltic pump for effluent collection were employed during production (WM 400, Watson Marlow Fluid Technology Group, USA). The pump was calibrated using silicon tubing and distilled water using a mass based method. 10 different levels and 2 different directions in the pump were measured twice (60 to 120 seconds) with distilled water. Accordingly, mass of each level was recorded to calculate the calibration coefficient of the pump in regards to the set level. pH was monitored at each sampling point, and accordingly, adjusted to 6.5 to 7.0 with the manual addition of NaOH (2M) when necessary during fermentation. Samples were taken from the effluent to be analyzed for residual glycerol, 2,3-BD, ethanol, 1,3-PDO, acetic, lactic and succinic acids.

Substrate Preparation and Application

The substrate used in this study was crude glycerol obtained from biodiesel production from a factory in Torbalı (Izmir, Turkey) in 10 L plastic containers. The composition of crude glycerol used was provided from the company as 54.35% glycerol (w/v), 34.81% water, 6.52% fat and ester, < 1%methanol (ppm), 3.53% NaOH, and 0.64% NaCl.

Glycerol determination in biodiesel waste was done by High Pressure Liquid Chromatography (HPLC). It was found to be 50% (w/v), the rest of the content were soap, trace amount of mixed salts and caustic. The initial content of glycerol in biodiesel waste was 80%. This amount was diluted using distilled water for a final concentration of 50% (500 g/L) in order to keep the waste product liquified. The above mentioned solution was diluted to required concentration during fermentation. The fermentation medium was prepa-

red as 5.72 g K_2HPO_4, 1.5 g KH_2PO_4, 2.0 g $(NH_4)_2SO_4$, 1.0 g yeast extract, 0.24 g $MgSO_4{\cdot}7H_2O$, 0.5 mL $FeSO_4{\cdot}7H_2O$ solution and 1.0 mL trace element solution. The trace element solution consisted of (mg/L distilled water) 200 $CoCl_2{\cdot}2H_2O$, 100 $MnCl_2{\cdot}4H_2O$, 70 $ZnCl_2$, 60 H_3BO_3, 20 $CuCl_2{\cdot}2H_2O$, 35 $Na_2MoO_4{\cdot}2H_2O$, 25 $NiCl_2{\cdot}6H_2O$, and 0.9 ml HCl (37%).

The MCBR was fed with crude glycerol at the concentration determined previously by [7] for a concentration of between 11 to 144 g/L. The substrate was fed in incrementing concentrations as follows, initial glycerol concentrations of (G_{in}); 11, 23, 48, 72, 92, 109, 112, 144 g/L of crude glycerol corresponding to organic loading rates (OLR) of 1.4, 2.9, 6.0, 9.0, 11.5, 13.6, 14.0 and 18.0 g/L.h.

Inoculum Preparation and Biofilm Formation

The inoculum used in this study was Citrobacter *freundii*, strain DSM 15979. The microorganism was provided by Alma Mater Studiorum University in Bologna from the German Collection of Microorganisms and Cell Cultures (DSMZ). The microorganisms were sub-cultured from agar cultures in Tryptic Soy Broth (TSB) that was used as growth medium, to be activated. They were then incubated at 30°C during at least 10 h.

Prior to incubation and fermentation, the bioreactor filled with immobilization materials was autoclaved (121°C at 1 atm for 30 min) for sterilization. The reactor was allowed to cool down and then inoculated with a stock culture of *C. freundii* DSM 15979 (10% (v/v)) together with sterile fermentation medium. The bioreactor was washed with N_2 to maintain anaerobic conditions. The bacteria was inoculated to the immobilized bioreactor under sterile conditions for 3 days with a dilution rate of 0.04 h^{-1} using a peristaltic pump (Watson Marlow 400). The continuous fermentation was initialized at the 72th h of the fermentation following a visible formation of the biofilm on the immobilization material as shown in Fig. 2. Glycerol concentration, thus OLR, in the fermentation medium was changed after at least 6 cycles (=~every 2 days) maintaining a hydraulic retention time (HRT) of 8 h (Dilution rate: 0.125 1/h). The reported results belong to the final three obtained values for each OLR, thus, the analysis were performed in triplicates and the measurements were reported as mean values with standard deviations.

Sampling and Analysis

10 mL of samples were collected from the bioreactor at each sampling point and 1.5 mL of the sample was centrifuged at 7379 x g for 15 min to be analyzed using a microcentrifuge (Beckman Coulter™ Microfuge® 18 Centrifuge with 24 x 0.22 L angle rotor). The supernatant was filtered through 0.22 µm syringe filters. Glycerol as the substrate, and 1,3-PDO, 2,3-BD, lactic acid, acetic acid, succinic acid and ethanol as the products were measured using HPLC (Agilent, USA) with a Phenomenex Rezex RHM Monosaccharide (H+) 300 x 7.8 mm ion exchange column, using a Thermo Surveyor Refractive Index Detector. The column temperature was 65°C and the detector temperature was 40°C and the injection volume is 20 µL. A solution of 5 mM H_2SO_4 was used as mobile phase at a flow rate of 0.6 mL/min [29].

Phosphate buffer solution (pH 7.1) was used to rinse the immobilization materials at the end of fermentation in order to remove the attached microorganisms from the surface of the materials. An additional 10 min sonication was employed in order to further remove remaining biomass on the surfaces followed by a final washing with the phosphate buffer solution was applied to calculate the immobilized to suspended cells percentile. The gravimetric method was used for total suspended solids (TSS) measurements [30]. Filter papers with a diameter of 0.45 µm were dried in an oven for 24 h at 105°C. Following, they were placed into a desiccator to cool to room temperature and filter papers were weighed to record their tares that were used for calculation. After that, the sample that was nearly 5 mL were filtered by the filter paper in the Erlenmeyer flask. The filtered paper was placed into an oven for 24 h at 105°C. Then, they were transferred to the desiccator and left to cool down for 30 min and weighed. All results of weighing were calculated

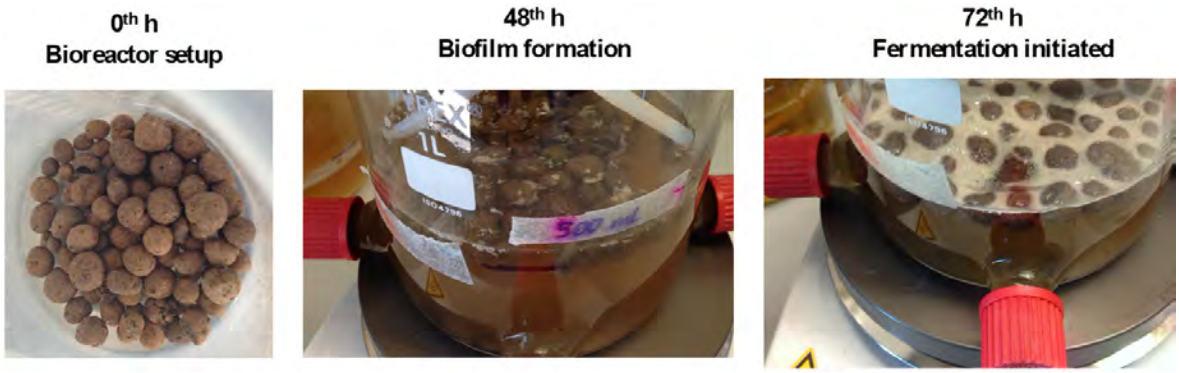

Figure 2. The stages of the ceramic immobilization material at the bioreactor setup (0th h), during biofilm formation (48th h) and at the initiation of fermentation (72th h).

according to the Equation (1) [30]:

$$T_{SS}\ (mg/L) = \begin{pmatrix} Final\ weigh\ of\ filter\ paper\ (g) \\ -Tare\ of\ filter\ paper\ (g) \end{pmatrix} x1000000 / Volume\ of\ sample \quad (1)$$

Calculations

Equation 2 was used to calculate the yields for the end product concentrations, and Equation 3 was used to calculate the productivities of the end products [31].

$$Y = C_x / S_i \quad (2)$$

$$Q = C_x / (t_f - t_i) \quad (3)$$

Where;

Y: the end product yield ($mol_{end\ product}/mol_{consumedglycerol}$); C_x: the compound concentration (g/L); S_i: the initial substrate concentration (g/L); Q: the productivity (g/L.h); t_f: the final fermentation time (h); t_i: the hydraulic retention time (h).

Statistical analysis

All data obtained from the MCBR were compared with a Kruskal-Wallis one-way analysis of variance (ANOVA) on ranks (Sigma Plot, USA). The results were evaluated with a 95% confidence interval.

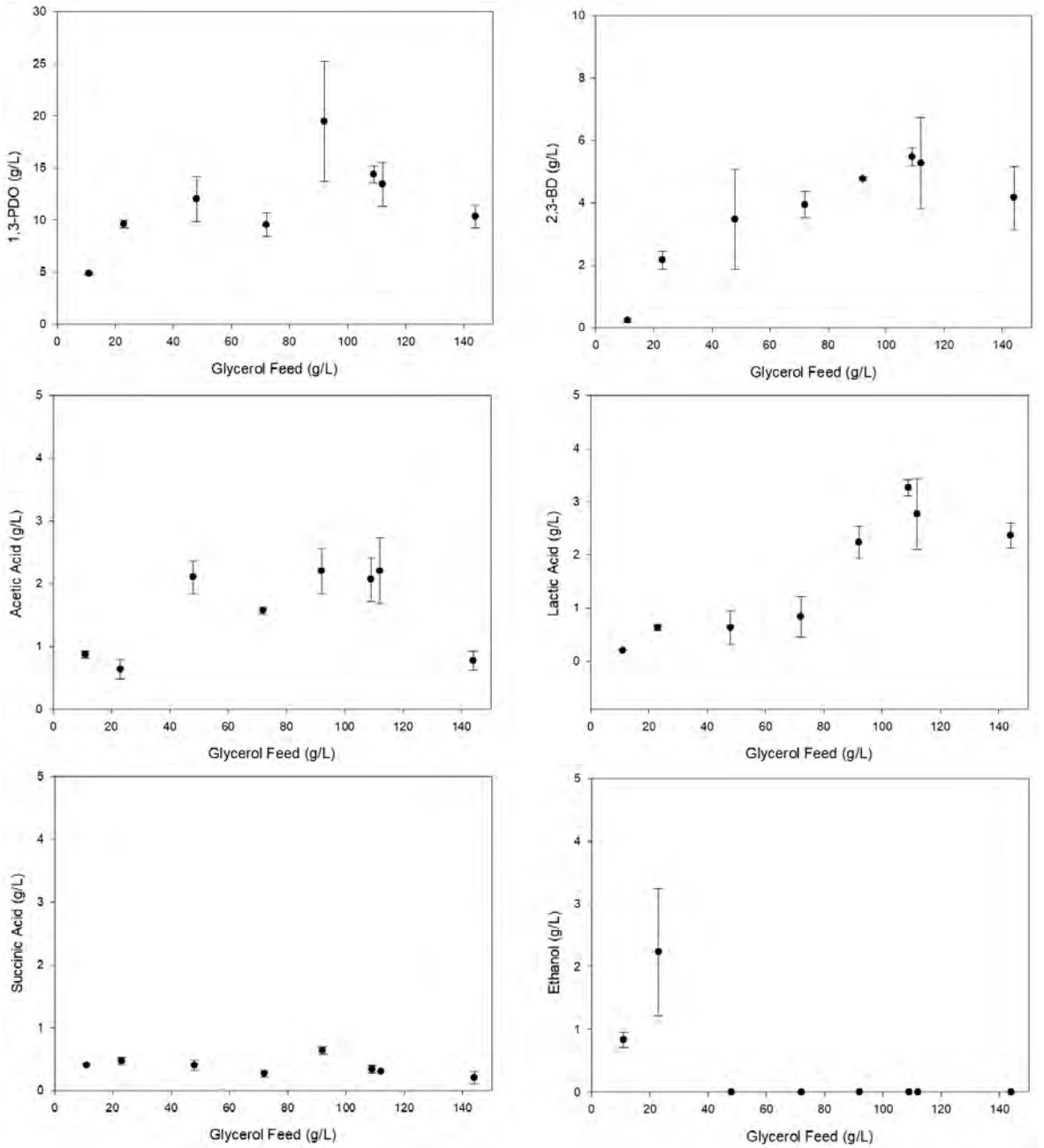

Figure 3. By-product concentrations at elevating glycerol feed (11 to 144 g/L).

RESULTS AND DISCUSSION

The biofilm reactor employed in the current study resulted in several by-products including organic acids, 1,3-PDO, and 2,3-BD. As depicted in Fig. 3, the final product with the highest concentration was 1,3-PDO reaching a maximum value of 26.1 g/L at an OLR of 11.5 g/L.h. 2,3-BD reached the second highest concentration followed by lactic acid, ethanol, acetic acid, and succinic acid; the highest concentrations were reported as 18.8, 3.5, 3.4, 3.0, and 0.8 g/L, respectively. Throughout the study the highest ethanol yield was reported to reach 0.2 mol/mol. However, when the glycerol feed was increased over 48 g/L, no ethanol production was observed. Similarly, according to Vivek et al. (2017), when the initial glycerol concentration was increased up to 60 g/L, no ethanol was reported [9].

In the present study, increased OLR negatively affected glycerol utilization (Table 1). The consumption rate was inversely proportional to the increasing OLR values except for the slight remission at 6.0 g/L.h. This situation can be explained by the acclimatation of the microorganisms following 6 cycles of the same condition, due to a sharp increase in the substrate concentration by 108%. Previous reports in the literature stated the inhibitory effects of high concentrations of the substrate on wild type microorganisms [20]. In order to overcome this issue and enhance the titers of 1,3-PDO and other metabolites, strategies such as acclimation of the microorganisms with the formation of biofilms [32], immobilization on inert materials , entrapment of cells in gels [33] or fed-batch mode of processing have been employed [5, 34, 35]. Similarly to the reported literature, at least 6 cycles of OLR was also successfully applied to the biofilm of *C. freundii* DSM 15979 cells in the present study to enhance the productivities (Table 1). The represented calculations were average of triplicate data during the experiments. ANOVA on ranks (Sigma Plot, USA) showed that there was a statistically significant difference in molar yields of the products based on the elevating initial glycerol concentrations ($p< 0.05$). Aquino de Souza et al. (2014) reported that the entrapped cells of K. *pneumoniae* BLh-1 reached the maximum productions of 1,3-PDO, 2,3-BD and ethanol by 22.22 g/L, 9.98 g/L and 1.42 g/L, respectively when 65 g/L of crude glycerol was fed to the system. In the present study, *C. freundii* DSM 15979 reported the maximum 1,3-PDO production when 92 g/L of crude glycerol was fed to the biofilm reactor together with the highest 2,3-BD titer (18.8 g/L), however, glycerol concentrations higher than 23 g/L resulted in no production of ethanol (Fig. 3). As shown in Fig. 4, the results of the TSS measurements also proved that 76% of the microorganisms were successfully immobilized on the ceramic immobilization material in the form of a biofilm.

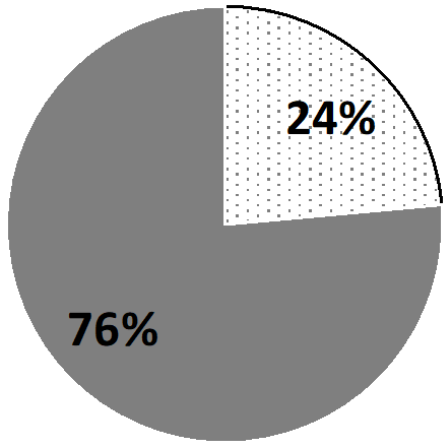

Figure 4. Immobilized (solid colored) vs suspended (dot illustrated) cell ratios as calculated at the end of the study.

A previous study by the research group reported the production of various metabolites from crude glycerol by suspended systems [7]. Accordingly, glycerol consumption by *C. freundii* DSM 15979 was reported to be sharply declined (as low as 4% consumption at Gin 140 g/L) with high glycerol loading as opposed to immobilized cultures reported in the present study. These results indicate the improved resistance of whole cells with the formation of biofilms.

Table 1. MCBR performance (Y in $mol_{end\ product}/molc_{onsumedglycerol}$ and Q in g/L.h) with incrementing glycerol feed.

Monitoring Time (h)	*Glycerolinitial (g/L)*	*OLR (g/L.h)*	*Glycerol Removal (%)*	*Y1,3-PDO*	*Y2,3-BD*	$Y_{lactic\ acid}$	$Y_{aetic\ acid}$	$Y_{succinic\ acid}$	$Y_{ethanol}$	*Q1,3-PDO*	*pH*
72	*11*	*1.4*	*100*	*0.54±0.01*	*0.02±0.01*	*0.02±0.00*	*0.12±0.01*	*0.03±0.00*	*0.15±0.02*	*0.60±0.00*	*6.28±0.35*
120	*23*	*2.9*	*99*	*0.51±0.02*	*0.10±0.01*	*0.03±0.00*	*0.04±0.01*	*0.02±0.00*	*0.20±0.09*	*1.17±0.06*	*6.43±0.43*
168	*48*	*6.0*	*51*	*0.78±0.27*	*0.23±0.23*	*0.03±0.02*	*0.17±0.09*	*0.02±0.01*	*0*	*1.27±0.55*	*6.37±0.15*
216	*72*	*9.0*	*69*	*0.18±0.02*	*0.16±0.05*	*0.0±0.06*	*0.0±0.08*	*0.0±0.01*	*0*	*1.17±0.12*	*6.54±0.07*
264	*92*	*11.5*	*70*	*0.56±0.28*	*0.31±0.10*	*0.14±0.05*	*0.22±0.10*	*0.03±0.01*	*0*	*2.47±0.72*	*6.01±0.17*
288	*109*	*13.6*	*64*	*0.25±0.02*	*0.08±0.01*	*0.05±0.22*	*0.05±0.01*	*0*	*0*	*1.80±0.10*	*6.18±0.16*
384	*112*	*14.0*	*42*	*0.42±0.22*	*0.14±0.08*	*0.07±0.04*	*0.10±0.07*	*0.01±0.00*	*0*	*1.70±0.26*	*6.56±0.47*
432	*144*	*18.0*	*20*	*0.44±0.09*	*0.15±0.02*	*0.09±0.02*	*0.04±0.01*	*0.01±0.00*	*0*	*1.30±0.10*	*6.27±0.16*

Comparison of 1,3-PDO, 2,3-BD and organic acid production

The 1,3-PDO and 2,3-BD molar yields achieved in this study are the maximum ones obtained via crude glycerol fermentation compared to the other reported studies by wild type *C. freundii* strains that formed biofilms (Table 2). The literature reports depicted the feasibility of the valorization of crude glycerol by various strains reaching up to 170 g/L of feed [3, 5].

As shown in Table 1, as the initial substrate concentration was increased, the consumption of glycerol was declined also causing a decrease in the productions of end-products suggesting an exertion of inhibition. A similar case was reported by Metsoviti et al. [5]. The group employed a fed-batch strategy in order to prevent this issue. Accordingly, they successfully improved the yields reaching a maximum 1,3-PDO concentration of 68.1 g/L.

Previous studies has suggested that under conditions where the energy is sufficient, microorganisms prefer the production pathways of products that are less toxic and that energy needs do not direct metabolism [36]. Accordingly, as also reported in Fig. 1, amongst all intermediate and end-products of glycerol fermentation, lactic acid, ethanol, butanol and H2 are the most important competitors of 1,3-PDO due to the requirement of reduced NADH during their production. Lower concentrations of these products are desired to enhance the yields of the target end-product. In the present study, as reported in Table 1, succinic acid was not capable of competing with 1,3-PDO for reducing equivalents, due to its low yields. In addition, although lactic acid commonly achieved lower yields (<0.09 mol/mol), it reached a yield of 0.14 mol/mol at an initial glycerol concentration of 92 g/L. A study by Maina et al. [6] also reported that *C. freundii* VK-19 was capable of producing lactic acid as high as 21.7 g/L, yielding 0.17 mol/mol. Furthermore, similar to the present study, succinic acid productions were reported to be negligible (<0.04 mol/mol). In another study by mixed cultures of Clostridia and Enterobacteria, considerable amounts of lactic acid production were observed during glycerol fermentation [28]. These results in the literature were in agreement with our study where increasing OLR up to a specific concentration (62.5 g/L) increased the 1,3-PDO yields and then decreased the yields due to the possible undesirable presence of inhibitory substances in the raw substrate. These results suggest that lactic acid production should also be minimized to enhance overall yields of 1,3-PDO or 2,3-BD.

One of the main challenges of the utilization of crude glycerol is the choice of microorganisms due to the inhibitory components of the raw substrate [28]. The growth associated production of all products reported in Fig. 1 requires a primary metabolism. In this context, utilizing tolerant species or improving the cell yields are of great importance for higher concentrations of end-products. As shown in Table 2, the 1,3-PDO productivities were significantly improved with the employment of immobilized and continuous systems [9, 37]. Compared with the previously reported literature by *C. freundii*, the highest molar yield was achieved in the present study.

Table 2. Comparison of the operating conditions, 1,3-PDO yields and productivities in various studies using crude or pure glycerol.

*Reactor Type**	*Glycerol (g/L)***	*Mode of action*	*Inoculated Microorganisms*	*1,3-PDO Yield (mol/mol)*	*1,3-PDO Productivity (g/L.h)*	*Reference*
CSTR	*25 PG*	*Batch*	*Klebsiella pneumonia CGMCC 1.6366*	*0.52*	*1.65*	*[38]*
CSTR	*20-80 CG*	*Fed-batch*	*C. butyricum VPI 1718*	*0.67*	*0.78*	*[39]*
PBR	*40 CG 40 Glu*	*Continuous*	*L. brevis N1E9.3.3*	*0.53*	*0.49*	*[9]*
CSTR	*40-170 CG*	*Fed-batch*	*C. freundii FMCC-B 294 (VK-19)*	*0.40*	*0.79*	*[5]*
CSTR	*15-50 PG*	*Batch*	*C. freundii AD119*	*0.72*	*0.96*	*[2]*
PBR	*36.8 PG*	*Continuous*	*C. freundii DSM 30040*	*0.57*	*8.2*	*[37]*
Shaked cultures	*50 CG 1.5 Glu*	*Batch*	*C. freundii*	*0.69*	*-*	*[40]*
MCPR	*11-144 CG*	*Continuous*	*C. freundii DSM 15979*	*0.78*	*2.47*	*This study*

**CSTR: Continuous stirred tank reactor; PBR: Packed bed reactor; MCPR: Modified continous biofilm reactor*

***PG: Pure Glycerol, CG: Crude Glycerol, Glu: Glucose*

CONCLUSION

An adequate approach to enhance the valorization of glycerol into several value-added products was performed with the aid of a modified continuous biofilm reactor (MCBR). This study depicted a novel approach to obtain the multi end-products including 1,3-PDO, 2,3-BD and acetic acid out of crude glycerol in a continuous mode of operation. The glycerol removal was realized between 20 to 100%. 1,3-PDO was obtained in the highest yield of 0.78 mol/mol. The continuous MCBR showed good stability under elevating crude glycerol concentrations showing its feasibility to high OLR. The outcomes of this study may be used as a know-how to scale-up the process in non-sterile conditions for integrated systems to industrial scale biodiesel plants. Furthermore, the production of the valuable biomonomer 1,3-PDO, which has a very important place in the textile sector, can be a very profitable return to the manufacturer.

ACKNOWLEDGEMENT

The author would like to acknowledge Prof. Dr. Nuri Azbar for his insightful discussions. The author would like to acknowledge Prof. Dr. Fabio Fava and Assoc. Prof. Dr. Lorenzo Bertin for their valuable contributions and for providing the

laboratory infrastructure. The author would like to thank Dr. Selene Grilli for her technical assistance with HPLC analysis.

References

1. Kumar V, Durgapal M, Sankaranarayanan M, Somasundar A, Rathnasingh C, Song HH, Seung D, Park S. Effects of mutation of 2,3−butanediol formation pathway on glycerol metabolism and 1,3−propanediol production by Klebsiella pneumoniae J2B. Bioresour Technol (2016) 214 432-440.
2. Drozdzynska A, Pawlicka J, Kubiak P, Kosmider A, Pranke D, Olejnik− Schmidt A, Czacyk K. Conversion of glycerol to 1,3−propanediol by Citrobacter freundii and Hafnia alvei − newly isolated strains from the Enterobacteriaceae. N Biotechnol (2014) 31 402-410.
3. Boenigk R, Bowien S, Gottschalk G. Fermentation of glycerol to 1,3−propanediol in continuous cultures of Citrobacter freundii. Appl Microbiol Biotechnol 1993; 38: 453-457.
4. Homann T, Tag C, Biebl H, et al. Fermentation of glycerol to 1,3−propanediol by Klebsiella and Citrobacter strains. Appl Microbiol Biotechnol (1990) 33 121-126.
5. Metsoviti M, Zeng AP, Koutinas AA, Papanikolau S. Enhanced 1,3−propanediol production by a newly isolated Citrobacter freundii strain cultivated on biodiesel−derived waste glycerol through sterile and non−sterile bioprocesses. J Biotechnol (2013) 163 408-418.
6. Maina S, Kachrimanidou V, Ladakis D, Papanikolau S, Machado de Castro A, Koutinas A. Evaluation of 1,3−propanediol production by two Citrobacter freundii strains using crude glycerol and soybean cake hydrolysate. Environ Sci Pollut Res (2019) 26 35523-35532.
7. Casali S, Gungormusler M, Bertin L, Fava F, Azbar N. Development of a biofilm technology for the production of 1,3−propanediol (1,3−PDO) from crude glycerol. Biochem Eng J. (2012) 64 84−90.
8. da Silva GP, Mack M, Contiero J. Glycerol: A promising and abundant carbon source for industrial microbiology. Biotechnol Adv (2009) 27 30-39.
9. Vivek N, Aswathi T V., Sven PR, Pandey A, Binod P. Self−cycling fermentation for 1,3−propanediol production: Comparative evaluation of metabolite flux in cell recycling, simple batch and continuous processes using Lactobacillus brevis N1E9.3.3 strain. J Biotechnol (2017) 259 110-119.
10. Pflügl S, Marx H, Mattanovich D, Sauer M. 1,3−Propanediol production from glycerol with Lactobacillus diolivorans. Bioresour Technol (2012) 119 133-140.
11. Zabed HM, Zhang Y, Guo Q, Yun J, Yang M, Zhang G, Qi X. Co−biosynthesis of 3−hydroxypropionic acid and 1,3−propanediol by a newly isolated Lactobacillus reuteri strain during whole cell biotransformation of glycerol. J Clean Prod (2019) 226 432-442.
12. Yun J, Yang M, Magocha TA, Zhang H, Xue Y, Zhang G, Qi X. Production of 1,3−propanediol using a novel 1,3−propanediol dehydrogenase from isolated Clostridium butyricum and co−biotransformation of whole cells. Bioresour Technol (2018) 247 838-843.
13. Guo Y, Dai L, Xin B, Tao F, Tang H, Shen Y, Xu P. 1,3−Propanediol production by a newly isolated strain, Clostridium perfringens GYL. Bioresour Technol (2017) 233 406-412.
14. González−Pajuelo M, Meynial−Salles I, Mendes F, Andrade JC, Vasconcelos I, Soucaille P. Metabolic engineering of Clostridium acetobutylicum for the industrial production of 1,3−propanediol from glycerol. Metab Eng (2005) 7 329-336.
15. Gallazzi A, Branska B, Marinelli F, Patakova P. Continuous production of n−butanol by Clostridium pasteurianum DSM 525 using suspended and surface−immobilized cells. J Biotechnol (2015) 216 29-35.
16. Sanguanchaipaiwong V, Leksawasdi N. Using Glycerol as a Sole Carbon Source for Clostridium beijerinckii Fermentation. Energy Procedia (2017) 138 1105-1109.
17. da Silva Ruy AD, de Brito Alves RM, Reis Hewer TL, de Aguiar Pontes D, Teixeira Gomes LS, Pontes Magalhaes LA. Catalysts for glycerol hydrogenolysis to 1,3−propanediol: A review of chemical routes and market. Catal Today (2020) 0-1 DOI: 10.1016/j.cattod.2020.06.035
18. Ji XJ, Huang H, Ouyang PK. Microbial 2,3−butanediol production: A state−of−the−art review. Biotechnol Adv (2011) 29 351-364.
19. Kalck P, Le Berre C, Serp P. Recent advances in the methanol carbonylation reaction into acetic acid. Coord Chem Rev (2020) 402 213078.
20. Sun YQ, Shen JT, Yan L, Zhou JJ, Jiang LL, Chen Y, Yuan JL, Feng EM, Xiu ZL. Advances in bioconversion of glycerol to 1,3−propanediol: Prospects and challenges. Process Biochem (2018) 71 134-146.
21. Białas W, Pikuła M, Mroczyk K, Grajek W. Production of 1,3−propanediol from glycerol by C. butyricum: Optimization of medium composition and kinetic studies. N Biotechnol. (2014) S101 DOI: 10.1016/j.nbt.2014.05.1855.
22. Varrone C, Skiadas I V., Gavala HN. Effect of hydraulic retention time on the modelling and optimization of joint 1,3 PDO and BuA production from 2G glycerol in a chemostat process. Chem Eng J. (2018) 347 1 525−534.
23. Yang X, Choi HS, Lee JH, Lee SK, Han SO, Park C, Kim SW. Improved production of 1,3−propanediol from biodiesel−derived crude glycerol by Klebsiella pneumoniae in fed−batch fermentation. Chem Eng J. (2018) 349 25−36.
24. Wischral D, Zhang J, Cheng C, Lin M, Galotti de Souza LM, Pellegrini Pessoa FL, Pereira Jr N, Yang ST. Production of 1,3−propanediol by Clostridium beijerinckii DSM 791 from crude glycerol and corn steep liquor: Process optimization and metabolic engineering. Bioresour Technol. (2016) 212 100−110.
25. Qureshi N, Annous BA, Ezeji TC, Karcher P, Maddox IS. Biofilm reactors for industrial bioconversion process: Employing potential of enhanced reaction rates. Microb Cell Fact (2005) 4 1-21.
26. Nemati M, Webb C. Immobilized Cell Bioreactors. Second Edi. Elsevier B.V. (2011) 331−346.
27. Paranhos AG de O, Silva EL. Statistical optimization of H2, 1,3−propanediol and propionic acid production from crude glycerol using an anaerobic fluidized bed reactor: Interaction effects of substrate concentration and hydraulic retention time. Biomass and Bioenergy (2020) 138 105575.
28. Sittijunda S, Reungsang A. Fermentation of hydrogen, 1,3−propanediol and ethanol from glycerol as affected by organic loading rate using up−flow anaerobic sludge blanket (UASB) reactor. Int J Hydrogen Energy (2017) 42 27558-27569.

29. Chen H, Fang B, Hu Z. Simultaneous HPLC determination of four key metabolites in the metabolic pathway for production of 1,3−propanediol from glycerol. Chromatographia. (2007) 65 9 629−632.
30. APHA. Standard Methods for the Examination of Water and Wastewater, AWWA, WPCF. 19th ed. Washington, DC, USA: American Public Health Association (1995).
31. Yoneda Y, Yoshida T, Kawaichi S, Daifuku T, Takabe K, Sako Y. Carboxydothermus pertinax sp. nov., a thermophilic, hydrogenogenic, Fe(III)−reducing, sulfur−reducing carboxydotrophic bacterium from an acidic hot spring. Int J Syst Evol Microbiol (2012) 62 1692-1697.
32. Szymanowska−Powałowska D, Leja K. An increasing of the efficiency of microbiological synthesis of 1,3−propanediol from crude glycerol by the concentration of biomass. Electron J Biotechnol (2014) 17 72-78.
33. Aquino de Souza E, Rossi DM, Záchia Ayub MAÔ. Bioconversion of residual glycerol from biodiesel synthesis into 1,3−propanediol using immobilized cells of Klebsiella pneumoniae BLh−1. Renew Energy (2014) 72 253-257.
34. Wong CL, Huang CC, Chen WM, Chang JS. Converting crude glycerol to 1,3−propandiol using resting and immobilized Klebsiella sp. HE−2 cells. Biochem Eng J (2011) 58-59 177-183.
35. Yang X, Kim DS, Choi HS, Kim KC, Thapa LP, Park C, Kim SW. Repeated batch production of 1,3−propanediol from biodiesel derived waste glycerol by Klebsiella pneumoniae. Chem Eng J (2017) 314 660-669.
36. Zeng AP, Biebl H, Schlieker H, Deckwer WD. Pathway analysis of glycerol fermentation by Klebsiella pneumoniae: Regulation of reducing equivalent balance and product formation. Enzyme Microb Technol (1993) 15 770-779.
37. Pflugmacher U, Gottschalk G. Development of an immobilized cell reactor for the production of 1,3−propanediol by Citrobacter freundii. Appl Microbiol Biotechnol (1994) 41 313-316.
38. Zheng Z ming, Guo N ni, Hao J, Cheng KK, Sun Y, Liu DH. Scale−up of micro−aerobic 1,3−propanediol production with Klebsiella pneumonia CGMCC 1.6366. Process Biochem (2009) 44 944-948.
39. Chatzifragkou A, Papanikolaou S, Dietz D, Douelgeraki AI, Nychas GJE, Zeng AP. Production of 1,3−propanediol by Clostridium butyricum growing on biodiesel−derived crude glycerol through a non−sterilized fermentation process. Appl Microbiol Biotechnol (2011) 91 101-112.
40. Anand P, Saxena RK. A comparative study of solvent−assisted pretreatment of biodiesel derived crude glycerol on growth and 1,3−propanediol production from Citrobacter freundii. N Biotechnol (2012) 29 199-205.

Hittite Journal of Science and Engineering, 2021, 8 (1) 63–70
ISSN NUMBER: 2148–4171
DOI: 10.17350/HJSE19030000214

A Kinetic Evaluation for Phenothiazine Base Copolymers

Fatih Dogan
Canakkale Onsekiz Mart University, Secondary Science and Mathematics Education, Canakkale, Turkey

Article History:
Received: 2021/01/10
Accepted: 2021/03/06
Online: 2021/03/31

***Correspondence to**: Fatih Dogan, Canakkale Onsekiz Mart University, Secondary Science and Mathematics Education, Canakkale, Turkey*
E-Mail: fatihdogan@comu.edu.tr
Phone: +90 507 227 18 01

ABSTRACT

In here, the nonisothermal decomposition kinetics of co-polymers based phenothiazine was present-ed. For this, firstly, 3, 7-di-2-thienyl-10H-phenothiazine (TF) was prepared via an optimized Suzu-ki–Miyaura cross-coupling reaction. After monomer (TF) characterization, the copolymerization re-actions with EDOT and thiophene were performed by the electrochemical technique. The molecular masses of the co-polymers were found by gel permeation chromatography (GPC) analysis. Thermal characterizations of the resulting polymers were conducted by thermogravimetric analyses. The thermal decomposition kinetics of the resulting polymers was also performed. For this, the kinetic methods (Tang, FWO, KAS, Kissinger, and Friedman) based on the multiple heating rates were used. Several kinetic parameters related to the decomposition kinetics of the solid-state were revealed.

Keywords:
Thermal decomposition; Kinetic; Phenothiazine; Copolymer.

INTRODUCTION

The first conductive polymers were discovered in 1975. Then, they have attracted considerable attention due to their interesting electrical conductivity [1]. Nowadays, the studies related to conductive polymers have gained a new acceleration due to the rapid developments in science and technology. In most of these studies, it is aimed to give to the polymeric materials some properties of semiconductors. Some properties which do not naturally exist in semiconductors are trying to be imparted to conductive polymers synthetically [2]. Since conductive polymer compounds, which are the product of polymerization, have a wide area in polymer technology, comprehensive studies have been carried out to date [3,4]. Among these conductive polymers, phenothiazine based polymers has been extensively studied for their applications in various electronic and electrochemical legal devices [5,6]. They are good electron-donor and hole transport materials, since the phenotiazine rings have electron-rich sulfur and nitrogen heteroatoms. However, many of their features are still known to be limited. On the other hand, to date, various methods have been used for the synthesis of conductive polymers. Chemical, enzymatic, oxidative, and electrochemical polymerization methods are used effectively for the conversion of monomers carrying groups such as thiophene, pyrrole, and carbazole to conductive polymers. Electrochemical polymerization is one of the most important polymerization methods of recent years. The first electrochemical synthesis is the production of PANi polymer by Letheby [7]. Later this method was used by Szaways [8]. Since then, conductive polymers such as polypyrrole (PPy), polythiophene (PTh), polypurane (PF), polyphenylene (PP), and polycarbazole (PCz) with π-electron conjugate structure have been synthesized for use in many applications [9]. Electrochemical polymerization is highly advantageous over other polymerization methods because of its superior properties such as the reaction being carried out at room temperature, controlling the film thickness by varying the applied voltage or current, the homogeneity of the films, and not requiring purification [10]. Here, it is aimed to synthesize phenothiazine copolymers by constant potential electrolysis. For this, the monomer was prepared as described in the literature [11]. The structure of the synthesized monomers was illuminated by FT-IR, UV-Vis, ^{1}H- and ^{13}C-NMR techniques. Characterizations of copolymers were carried out by TG-DTA, CV, and GPC. In the final stage of the research, the solid-state degradation kinetics of phenothiazine based conductive polymers were calculated using TG-DTG data under non-isothermal conditions. Accordingly, to our knowledge, this study is the first report to exa-

mine the kinetics related to the solid state degradations of phenothiazine based conductive polymers.

EXPERİMENTAL METHODS

Materials

Phenothiazine, 3-thiophene boronic acid, Aliquot 336, N-bromosuccinimide (NBS), silicon diox-ide (SiO_2), tetrakis (triphenylphosphine) palladium (0) [$Pd(PPh_3)_4$], 3,4-ethylenedioxydiophene (EDOT), Potassium carbonate (K_2CO_3), sodium hydroxide (NaOH), thiophene, 18-crown-6, DMSO, DMF, THF, ethyl acetate, ethyl alcohol, methyl alcohol, chloroform, ether, acetone, ace-to-nitrile, 2-methoxy ethanol, hexane, heptane, 1,4-dioxane, $CHCl_3$, and CCl_4 were obtained from Merck (Germany) and used in the experiments without pre-purification.

Measurement Techniques

HEIDOLPH branded magnetic stirrers were used for the synthesis processes. To dry glassware and chemicals J.P. Selecta brand vacuum oven was used. Column chromatography was performed using silica gel. UV-vis spectra of copolymers were obtained from indium–tin oxide (ITO, solid phase) surface using an Analytic Jena Speedcord S-600 diode-array spectrophotometer. Fourier Transform Infrared (FT-IR) Spectrometer (Perkin Elmer FT-IR Spectrum one) and Nuclear Magnet-ic Resonance (NMR) Spectrophotometer (JEOL ECX II 400 MHz) were used for structural charac-terization of synthesized substances. ^1H and ^{13}C-NMR analysis used DMSO-d_6 as a solvent. UV-vis analyzes were performed using a double beam path spectrophotometer and quartz cuvet. DMSO was used as a solvent in UV measurements. The number average molecular weight (M_n), Mass aver-age molar mass (M_w), and polydispersity index (PDI) of the copolymers were found by Viscotek GPC/SEC systems. To determine the electrochemical properties of resulting polymers, cyclic volt-ammograms were taken using CH Instruments 660 C Electrochemical Analyzer (CH Instruments, Texas, USA). The copolymers were coated on platinum or ITO. A platinum wire was used as a counter electrode. The non-aqueous Ag/Ag+ was determined as a reference electrode. After the coating of resulting copolymers was on ITO/glass surface via electro-oxidative polymerization, the films were rinsed with ACN. The thermal properties of synthesized polymers were determined by using Thermogravimetry-Differential Thermal Analysis (TG-DTA Perkin Elmer Diamond Thermal Analysis System) [12,13]. The measurements were carried out in an N_2 atmosphere between 20-1000°C, at the heating rate of 5, 10, 15, and 20°C/min.

Synthesis of 3,7-dibromo-10H-phenothiazine

A solution of 10 mmol (1.99 g) phenothiazine in 20 mL THF was placed in a 100 mL two-necked flask in an ice bath. To the resulting yellow solution, a solution of 22 mmol (3.91 g) of NBS dis-solved in 45 mL of THF was added dropwise for 1 hour. The dark green solution formed after the drop was cooled to room temperature and stirred for a further 24 hours. After the solvent removal, the residue was purified over silica gel. A light green product was obtained (2.50 g, yield: 70%) [14]. The reaction scheme for the synthesis of 3, 7-dibromo-10H-phenothiazine is given in Fig. 1

Synthesis of 3,7-di-2-thienyl-10H-phenothiazine (TF Monomer)

In a 100 mL flask, 4 mmol (1.42 g) of 3, 7-dibromo-10H-phenothiazine was dissolved in a boil-ing ethoxyethanol-water (40: 4, 44 mL) mixture. 20 mmol (2.76 g) of K_2CO_3 was added to the re-sulting green solution and stirred at 130 0C for half an hour. Then 11.2 mmol (1.43 g, 2.8 eq.)

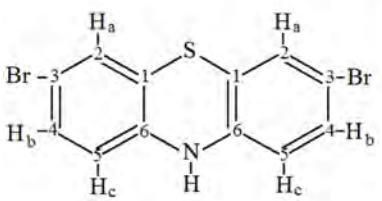

FTIR (ATR, cm^{-1}): 3337 ν (NH stretch, thiomorpholine ring), 1592, 1566, 1441 ν (C = C stretch, phenyl), 1311 ν (C=N bending, thiomorpholine ring), 737 ν (C-S bending, thiomorpholine ring), 649 ν (C-Br bending)

^1H-NMR (DMSO-d_6, ppm, δ): 8.85 (s, 1H, -NH), 6.59 (d, 1H, Ar-HC), 7.14 (dd, 1H, Ar-H_a), 7.11 (s, 1H) (Ar-H_b)

^{13}C-NMR (DMSO-d_6, ppm, δ): 141.43 (6-C), 130.12 (3-C), 128.62 (1-C), 118.72 (5-C), 116.55 (2-C), 113.19 (4-C)

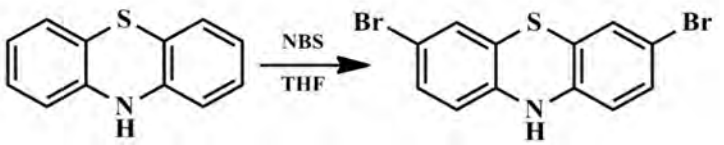

Figure 1. Synthesis of 3, 7-Dibrom-10H-phenothiazine

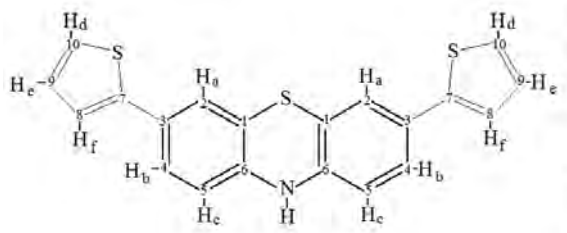

FTIR (ATR, cm^{-1}): 3334 ν (NH stretch, thiomorpholine ring), 1592, 1566, 1465 ν (C = C stretch, phenyl), 1298 ν (CH-N bending, thiomorpholine ring), 798 ν (CH-S bending, thiomorpholine ring);
^{1}H-NMR (DMSO-d_6, ppm, δ): 8.96 (s, 1H, -NH), 7.49 (d, 1H, Ar-Hd), 7. 42 (d, 1H, Ar-Hf), 7.33 (s) , 1H, Ar-Ha), 7.28 (d, 1H, Ar-Hb), 7.13 (t, 1H, Ar-He), 6.75 (d, 1H, Ar-HC);
^{13}C-NMR (DMSO-d 6, ppm, δ): 143.12 (6-C), 141.10 (7-C), 128.86 (1-C), 128.30 (10-C), 125.50 (8-C), 124.88, 123.36 (3-C), 122.89 (9-C), 117.17 (4-C), 115.25 (5-C)

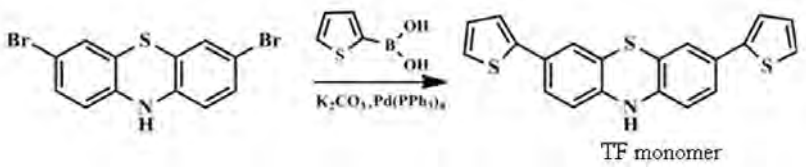

Figure 2. Synthetic scheme of 3, 7-di-2-thienyl-10H-phenothiazine

of 2-thiophene boronic acid and 0.06 mmol (70 mg) [Pd $(PPh)_3]_4$ as catalyst was added and the mixture was refluxed at 130 °C for 2 hours. After two hours, the mixture was cooled down to room temper-ature and precipitated with the distilled water. The precipitation was carried out by stirring the mix-ture continuously with a magnetic stirrer. The precipitate was filtered and washed with an ethanol-acetone (1:1 v/v) solvent mixture. The resulting light yellow product was dried in a vacuum oven at 40°C for 6 hours (1.16 g, yield: 81%) [15]. The reaction scheme for the synthesis of 3, 7-di-2-thienyl-10H-phenothiazine is given in Fig. 2.

Electrochemical Characterization

Data from voltammograms were used to determine the electrochemical properties of the resulting copolymers on the ITO surface [16]. Electrochemical measurements were performed in a quartz cell using non-aqueous Ag/Ag+ as the reference electrode, platinum wire as the counter electrode, and ITO as the working electrode. 0.1 M $TBAPF_6$ was used as a support electrode.

Electrochemical Copolymerization of TF Monomer with Thiophene and EDOT

To determine the electrochemical properties of synthesized TF monomer by using cyclic voltam-mograms, CH Instruments 660 C Electrochemical Analyzer was used. The resulting copolymers were obtained by cyclic voltammograms repeated at a scanning rate of 50 mV/s in 0.1 M $TBAPF_6$/ACN. For this, 20 mg TF monomer and 0.9 ml thiophene (d: 1.05 g/cm^3) were dissolved in 9 ml 0.1 M $TBAPF_6$/ACN and 1 ml $BF_3.OET_2$ support electrolyte solution. Copolymerization was then performed on the ITO surface at a scanning speed of 50 mV/s, with a potential range of (+1.8)-(-0.4) V. In the case of copolymerization of TF monomer with EDOT, 20 mg of TF monomer and 0.7 ml of 3,4-ethylene dioxythiophene (d:1.33 g/cm^3, EDOT) were dissolved in 9 ml of 0.1 M $TBAPF_6$/ACN and 1 ml of $BF_3.OET_2$ support electrolyte solution. Copolymerization was performed by the electrochemical method to the ITO surface at a scanning speed of 50 mV/s, in the potential range (-1.6)-(+1.6) V. Synthetic pathway for electrochemical copolymerizations of the TF monomer with thiophene or EDOT is given in Fig. 3. The films of the resulting copolymer were coated onto the ITO surface by electro oxidative polymerization and then washed with ACN.

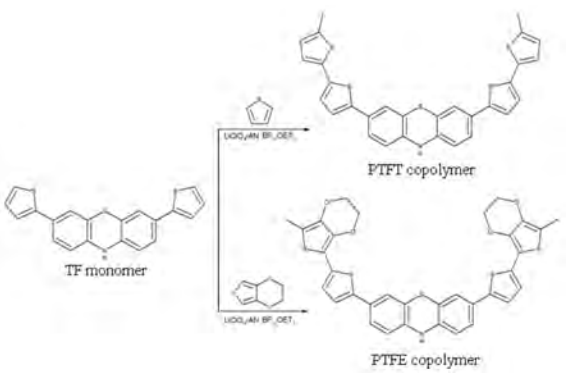

Figure 3. Electrochemical copolymerization of TF monomer by EDOT and thiophene

RESULTS AND DISCUSSION

Structural Characterization

3,7-di-2-thienyl-10H-phenothiazine used in electro-polymerization was synthesized from 3,7-dibromo-10H-phenothiazine according to standard literature procedures [11]. The chemical structure of each compound was confirmed by FT-IR, ^{1}H-NMR, and ^{13}C-NMR spectra. Significant changes were also observed in the FT-IR spectra of each compound relative to the starting material pheno-thiazine. The C-Br bending peak of 3,7-dibromo-10H-phenothiazine was observed at 649 cm^{-1} in the FTIR spectrum. Also, the N-H tensile peak of the thiomorpholine ring was determined at 3337 cm^{-1}, and the C-N peaks at 1311 cm^{-1}. In the 1H-NMR spectrum, the hydrogen atom in the thiomorpho-line ring showed a single signal at 8.85 ppm. Thus, both the FT-IR and ^{1}H-NMR spectra of this compound showed that the Bromine did not bind at the N-position. Also, the aromatic proton signal at 6.59 ppm (1H, binary) and 7.11 ppm (1H, single) was observed. On the other hand, it was deter-mined that the Hb proton at 7.14 ppm split into the doublet of the doublet due to the remote group interaction with the Ha proton. In the ^{13}C-NMR spectrum, characteristic resonance peaks of six dif-ferent carbon atoms between 113-141 ppm were determined. All these results confirm that the -NH group on phenothiazine is protected and that the halogenation reaction takes place via the aromatic ring. However, in the FTIR spectrum of 3,7-di-2-thienyl-10H-phenothiazine, the C-Br peak at 649 cm^{-1} was lost and the C-S peak in the thiomorpholine ring was observed at 798 cm^{-1}. The N-H and C-N peaks in the thiomorpholine ring were also observed, respectively, at 3334 cm^{-1} and 1298 cm^{-1}. In the ^{1}H-NMR spectrum, the N-H bond in the thiomorpholine ring was exhibited as a single peak at 8.96 ppm. Also, this compound gave peaks at 7.49 ppm (1H, doublet), 7.42 ppm (1H, doublet), 7.33 ppm (1H, singlet), 7.28 ppm (1H, doublet), 7.13 ppm (1H, triplet)) and 6.75 ppm (1H, doublet). However, in the ^{13}C-NMR spectrum, this compound showed resonance signals of ten different car-bon atoms between 115-143 ppm.

Optical and Electrochemical Properties

UV-vis spectra of PTFT and PTFE copolymers were taken from the ITO surface and given in Fig. 4. The UV-vis spectrum of the TF monomer exhibited a maximum absorption (λmax) at 364 nm. This maximum peak is attributed to π- π* transitions in the aromatic ring. The UV-vis spectrum of PTFT copolymer showed a peak at 397 nm shifting to 33 nm red when compared to the TF mon-omer. This is related to the higher conjugation of PTFT than the TF monomer. On the other hand, PTFE

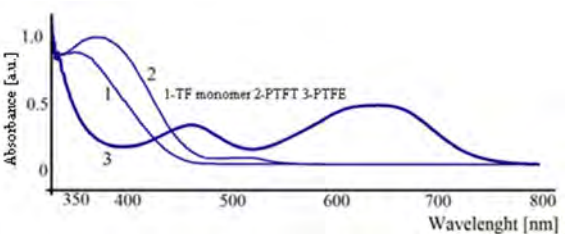

Figure 4. UV-vis spectra of TF, PTFT, and PTFE on ITO surface

showed two peak absorption peaks at 460 nm and 643 nm due to high conjugation compared to both TF and PTFT copolymer. The lowest spectral energy edge bands of the absorption spectra of FT and PTFT copolymer were measured as 481 and 494 nm, respectively. Accordingly, the optical band gaps were 2.57 eV for TF monomer and 2.5 eV for PTFT. In the case of PTFE, the lowest spectral energy edge bands λmax_1 and λmax_2 were determined to be 567 and 783 nm, respectively. Accordingly, the optical band gap for PTFE was calculated as 2.18 eV for λmax_1 and 1.58 eV for λmax_2.

On the other hand, PTFT and PTFE copolymers were formed by electrochemical cyclic Voltam-metry at a scanning rate of 50 mV/s. The first cyclic voltammograms for TF, PTFT, and PTFE co-polymers are given in Fig. 5.

Fig. 5 show the first cyclic voltammograms of PTFE and PTFT at a scanning speed of 50 mV/s. According to Fig. 5, the first oligomeric products were taken in the range of -1.4-1.6 V for PTFT and -0.4-1.6 V for PTFE. The oxidation peak of PTFE was observed at 0.51 V. İts reduction peak was at -0.39 V. Also, the oxidation peak and reduction of PTFT was exhibited at 0.82 V and 0.44 V, respectively. Accordingly, each voltammogram showed a single oxidation and reduction peak with a reversible character. Functioned thiophene compounds such as thiophene or 3,4-ethylene dioxythiophene (EDOT) can be very easily oxidized. The radicals formed as a result of this oxidation can be joined together to form a polymerization reaction easily on the ITO electrode. İn here PTFE and PTFT copolymers were obtained by cyclic Voltammetry. Voltagram collection was continued until no electroactive species could be recovered from the monomer. The copolymeriza-tion reaction of TF monomer with EDOT was carried out between -1.4-1.6 V. In the voltammogram of PTFE, the oxidation peak at 0.51 V shifted

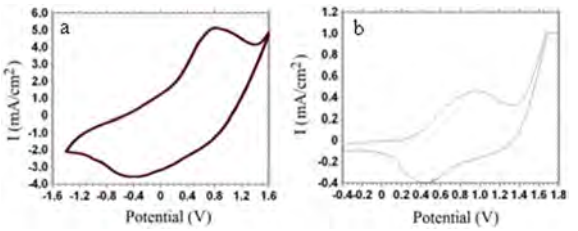

Figure 5. First cyclic voltammograms of PTFE (a) and PTFT (b) at a scanning speed of 50 mV/s

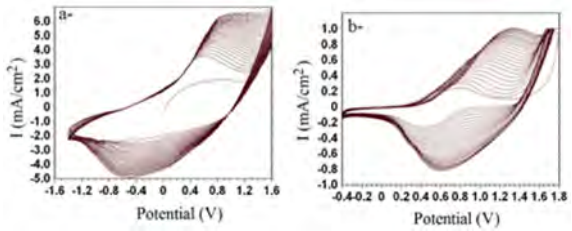

Figure 6. Sequential cyclic voltammograms of PTFE (a) and PTFT (b) in the repeated potential screening of FT.

to 0.88 V and the reduction peak at -0.39 V shifted to 0.62 V. On the other hand, the copolymerization reaction of TF monomer with thiophene was carried out between -0.4-1.8 V. Here, the oxidation potential shifted from 0.82 V to 1.27 V and the reduction potential shifted from 0.44 V to 0.62 V. The sequential voltammograms obtained by con-sequently the shift of the reaction to the high potentials by binding of the active species showed that the copolymerization reactions took place [17]. Cyclic voltammograms for electroactive PTFE and PTFT copolymers deposited on ITO are given in Fig. 6

Furthermore, the dependence of the scanning speed versus the current density of copolymers de-posited on ITO in the 0.1 M $TBAPF_6$/ACN support solution is shown in Fig.s 7 and 8. Fig.s 7 and 8 showed a linear relationship between current density and scanning speed. This event was at-tributed to the non-diffusion process.

It was determined that there is a linear relationship between scanning velocities and current in-tensives in Fig.s 7 and 8, which shows the scanning velocity dependence in copolymerization re-actions. GPC was used to calculate the average molar masses of the soluble portions of the PTFE and PTFT. The results are given in Table 1. According to GPC analysis, polymers have low PDI values. Low PDI indicates a controlled polymerization reaction [18].

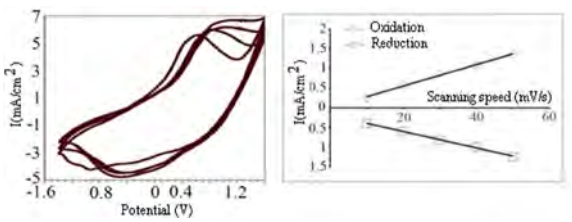

Figure 7. The current density of PTFE at scanning speeds of 10, 20, 40, 60, 80 mV/s

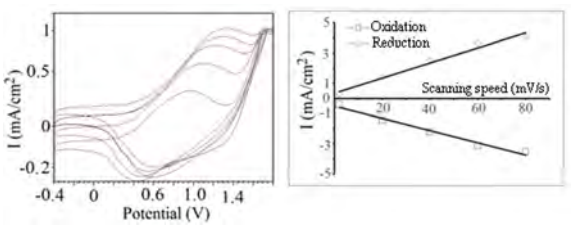

Figure 8. Current density of PTFT at scanning rates of 1, 20, 40, 60, 80 mV/s

Table 1. GPC analysis of PTFE and PTFT

Copolymers	M_n (gmol^{-1})	M_w(gmol^{-1})	PDI
PTFT	22782	32578	1.43
PTFE	13850	19113	1.38

Kinetic Evaluation

Non-isothermal methods are often used for the evaluation of mechanisms and kinetics of solid-state reactions. Most of these thermo analytic methods are based on the Arrhenius equation.

$$k = A\exp(-E / RT) \tag{1}$$

and rate expression occurs

$$da / dt = kf(a) \tag{2}$$

Here, f (α) is the kinetic function. α is the conversion fraction. If f (α) = (1-α) n and dT / dt = β occur equally at constant temperature, Eq. 2 can be written as follows.

$$g(a) = \int_0^a \left[\frac{1}{(1-n)^n}\right] da = \frac{A}{\beta}\int_{T_0}^{T} \exp(\frac{-E}{RT})dT \tag{3}$$

Here; n is the degree of reaction. Eq. 4 can be written for the special case n = 1. On the other hand, Eq. 5 can be written for n ≠ 1 values.

$$\int_0^a \left[\frac{1}{(1-n)}\right] da = -\ln(1-a) \tag{4}$$

$$\int_0^a \left[\frac{1}{(1-n)^n}\right] da = -\frac{1-(1-a)^{1-n}}{1-n} \tag{5}$$

Many techniques are using different approximations to solve Eq. 3. The following isoconver-sional methods were used to calculate kinetic parameters related to the solid-state degradation of copolymers.

Tang Method

When an appropriate approach is used for the solution of Eq. 2 and the logarithm of both sides is taken, the equation given below can be obtained [19].

$$\ln\left(\frac{g(a)}{T^{1.894661}}\right) = \begin{bmatrix} \ln\dfrac{AR}{Rg(a)} \\ +3.635041 \\ -1.894661\ln E \end{bmatrix} - \left(\frac{1.001450E}{RT}\right) \tag{6}$$

Here, the activation energy (E_a) can be found from the slopes of the Arrhenius plots at different heating rates.

Kissenger-Akahira-Sunose Method

This method is an integral isoconversional method and E_a is calculated in similar ways as in other methods. According to the Kissenger-Akahira-Sunose method, an equation is obtained as follows [20,21].

$$\ln\left(\frac{g(a)}{T^2}\right) = \ln\left[\frac{AR}{Eg(a)}\right] - \frac{E}{RT} \quad (7)$$

Kissinger Method

E_a can be calculated without using any reaction mechanism, by using the following equation [20].

$$\ln\left(\frac{\beta}{T_{max}^2}\right) = \left\{\frac{AR}{E} + \ln\left[n(1-a_{max})^{n-1}\right]\right\} - \frac{E}{RT_{max}} \quad (8)$$

where β, T_{max}, A, α_{max} and n are the heating rate, temperature, pre-exponential factor, the maxi-mum conversion fraction, and reaction order. E_a can be calculated from the graph of ln ($\beta/T2_{max}$) ver-sus 1000 /T_{max}.

Flynn-Wall-Ozawa Method

This is an integral method. In this technique, A, f (α), and E_a are independent of both conversion fraction and the temperature. This technique uses the following logarithmic equation [22,23].

$$\log\beta = \log\left[\frac{AE}{R}\right] - \log\beta + \log p\left(\frac{E}{RT}\right)\frac{E}{RT} \quad (9)$$

Using Doyle approximation and assuming E/RT> 20 for the integral function, the above equation can be simplified as follows

$$\log\beta = \log\left[\frac{AE}{R}\right] - \log g(g(a)) - 2.315 - 0.4567\frac{E}{RT} \quad (10)$$

Friedman Method

The Friedman method uses Eq. 11 based on the Arrhenius equation for thermal decomposition kinetics [24].

$$\ln\left(\frac{da}{dt}\right) = \ln(A) + \ln(1-n) - \frac{E}{RT} \quad (11)$$

In the above equations, α, g(α), β, T_m, A, and R are the degree of reaction, integral function, heating rate, temperature, pre-exponential factor, and gas constant, respectively. A line is obtained by plot-ting 1/T versus ln (dα /dt) and E/R is determined from the slope of this line.

Thermal Decomposition Kinetic

The decomposition kinetics of the copolymers were performed by the TG technique. Kinetic pa-rameters were calculated using multiple heating rate methods. The TG curves obtained in the dy-namic nitrogen atmosphere of the copolymers were given in Fig. 9. TG experiments were carried out in nitrogen of 50 mL min^{-1} gas at heating rates of 5, 10, 15, and 20 °C min^{-1}. Analyses were performed by using 8-10 mg samples. All TG curves showed that copolymers degrade in one step.

The first decomposition temperature (T_{on}) in addition to the temperatures at which 20% and 50% mass losses occurred were found from the TG thermograms. Furthermore, DTG curves were used to determine temperatures (T_{max}) corresponding to the maximum decomposition rate. DTA curves were used to determine the exothermic and endothermic nature of decomposition. According to the TG curve of PTFE copolymer at a heating rate of 5 ° C/min, the initial decomposition temperature was 104 ° C. 20% and 50% mass loss was observed at 245 °C and 328 °C, respectively. The amount of residue at 1000°C was calculated to be about

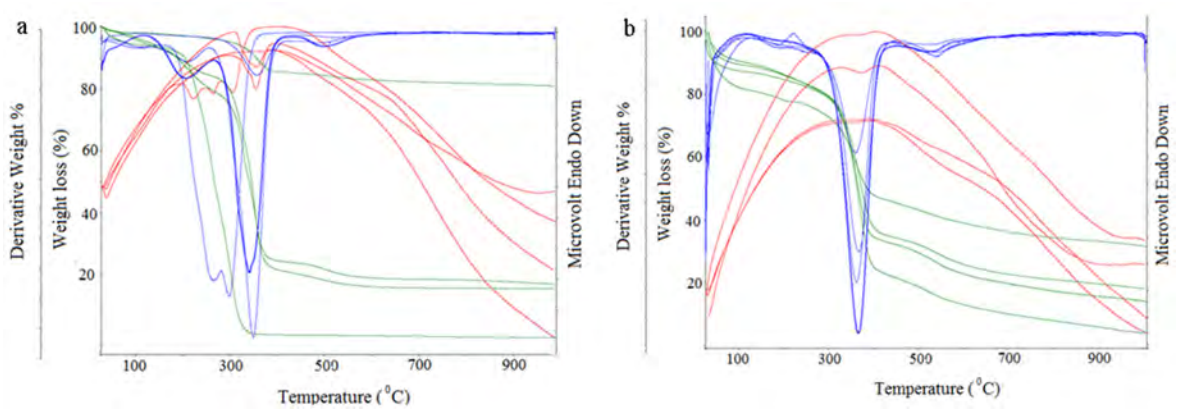

Figure 9. TG / DTG and DTA thermograms of PTFE (a) and PTFT (b) at different heating rates

11%. This compound was degraded in one step and T_{max} was found as 303 °C. During the decomposition of the PTFE copolymer, the presence of an endothermic peak at 318 °C was observed in the DTA curve. According to the TG curve obtained at a heating rate of 5 oC/min of PTFT copolymers the initial decomposition temperature was deter-mined as 231 oC. The temperatures at which 20% and 50% mass loss were observed were 283 ° C and 347 °C, respectively. The amount of residue at 1000°C was calculated to be approximately 8%. This compound was determined to be degraded in one step. From the DTG curve, T_{max} was calculated as 381 °C. During the decomposition of PTFT copolymers, the presence of an endothermic peak at 399 ° C was observed in the DTA curve.

Kinetic Studies

There are many techniques for the solution of Eq. 3. In this study, several techniques were used to investigate the kinetic parameters of copolymers. These techniques are FWO, KAS, Tang, and Kissinger methods. For these methods, the TG curves at multiple heating rates are used. For the calculation the kinetic parameters of copolymers, firstly Kissinger method and isoconversional meth-ods were used. According to the Kissinger method, E_a related to the thermal decomposition kinetics of PTFE and PTFT was found to as 75.23 kJ mol^{-1} and 83.47 kJ mol^{-1}, respectively. According to equation [6], E_a can be found from the graph of 1000 / T versus ln ($\beta/T^{1.894661}$). The average value of E_a for PTFE and PTFT was found to as 75.8 $kJmol^{-1}$ and 93.8 $kJmol^{-1}$, respectively. The values obtained for copolymers were given in Table 2. KAS is an another method

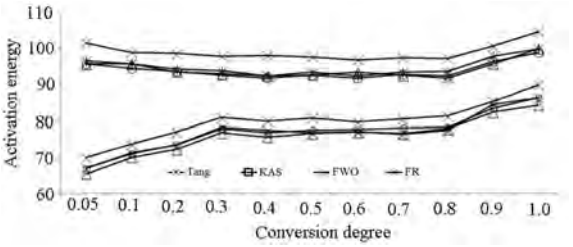

Figure 10. E_a values as a function of the conversion degree

used in this study. In the conversion fractions given α = 0.05-0.95, E_a determined from the slope of the graph of ln (β/T^2) ver-sus 1000/T was calculated as 74.7 and 92.8 $kJmol^{-1}$ for PTFE and PTFT, respectively. The result is very close to the value obtained by the Tang method. Another method used in this study is FWO. At a constant conversion, the slope of the line obtained from log β versus 1000/T graph is equal to 0.456 E/RT. E_a can be found from here. In Fig. 15, the plots of ln β versus 1000/T at a different conver-sion value are plotted, and the values found here are 75.7 and 93.1 $kJmol^{-1}$ for PTFE and PTFT, re-spectively. As a result, the E_a obtained by all three methods for copolymers were very close to each other. Finally, Ea for PTFE and PTFT using the Friedman method was determined as 78.8 and 97.9 $kJmol^{-1}$, respectively.

Fig. 10 shows the Arrhenius type curves in the range of α = 0.05-0.95. As given in Fig. 10, the minimum E_a values required for copolymers to start degradation is 64.3 and 94.6 $kJmol^{-1}$ for PTFE and PTFT, respectively. E_a required for the degradation step of PTFE and PTFT copolymer are very close to each other within the limits of 0.2 <α <0.9. When the

Table 2. E_a values obtained by Tang, KAS, FWO, and Friedman methods

Decomposition Steps								
	PTFE				*PTFT*			
α	*Tang*	*KAS*	*FWO*	*FR*	*Tang*	*KAS*	*FWO*	*FR*
0.05	*65.8*	*64.3*	*65.9*	*68.9*	*91.6*	*94.6*	*94.6*	*100.5*
0.1	*69.8*	*68.9*	*70.1*	*72.5*	*94.7*	*93.4*	*94.6*	*97.8*
0.2	*72.3*	*71.1*	*72.4*	*75.8*	*93.2*	*92.6*	*92.4*	*97.5*
0.3	*76.8*	*75.6*	*77.1*	*79.8*	*92.7*	*91.6*	*91.9*	*96.7*
0.4	*75.7*	*74.5*	*76.4*	*78.9*	*91.4*	*90.7*	*91.4*	*96.9*
0.5	*76.4*	*75.4*	*75.6*	*79.7*	*92.3*	*91.5*	*91.6*	*96.5*
0.6	*76.5*	*75.8*	*75.9*	*78.6*	*91.4*	*90.8*	*92.3*	*95.7*
0.7	*76.9*	*75.4*	*75.2*	*79.4*	*92.3*	*91.7*	*91.5*	*96.4*
0.8	*77.1*	*76.7*	*76.3*	*80.2*	*92.5*	*91.4*	*90.8*	*96.2*
0.9	*82.3*	*81.3*	*83.5*	*84.3*	*96.8*	*95.3*	*94.7*	*99.6*
0.95	*85.2*	*83.2*	*85.2*	*88.9*	*98.9*	*97.8*	*98.8*	*103.6*
Average	*75.8*	*74.7*	*75.7*	*78.8*	*93.8*	*92.8*	*93.1*	*97.9*

α; conversion fraction

mass loss reaches 90%, co-polymers have required energy of 90 kJmol^{-1}

CONCLUSION

Here, a phenothiazine monomer whose preparation was previously presented in the literature was again synthesized and its PTFE and PTFT were prepared by the electropolymerization method. Characterization of the phenothiazine-based monomer was performed by UV-Vis, FT-IR, ^{1}H-NMR, and ^{13}C-NMR spectra. Also, the average molecular mass of PTFE and PTFT by the GPC was found as approximately 13850 g mol^{-1} and 22782 g mol^{-1}, respectively. In the following study, the solid-state decomposition kinetics of PTFE and PTFT were evaluated by using thermal curves. The kinetic parameters of the decomposition were determined using Kissinger, Tang, KAS, FWO, and Fried-man methods based on multiple heating rates. Accordingly, the mean values of Ea obtained by the Tang method for PTFE and PTFT were 75.8 and 93.8 kJmol^{-1}, respectively. The obtained co-polymers can be used in various applications such as organic field-effect transistors [25], chemilumi-nescence [26] and light-emitting diodes [27] due to their the electro-optical properties

ACKNOWLEDGMENT

This study was supported by Çanakkale Onsekiz Mart University, the Scientific Research Coordination Unit, (Project Nu:FBA:2013-83)

References

1. Shirakawa, H., Louis, E.J., MacDiarmid, A.G., Chiang, C.K, Heeger, A.J. Synthesis of elec-trically conducting organic polymers: halogen derivatives of polyacetylene, (CH)x. Journal of the Chemical Society, Chemical Communications, 16 (1977) 578-580
2. Forster, R.J, Vos, J.G. Homogeneous and heterogeneous charge transfer dynamics of [Os(bipy)2(PVP)nCl]Cl films in neutral pH electrolytes, Electrochimica Acta, 37 (1992) 159-167.
3. Aktaş N, Optimization of biopolymerization rate by response surface methodology (RSM), Enzyme and Microbial Technology 37 (4) (2005) 441-447
4. Güreşir M, Aktaş N, Tanyolaç A, Influence of reaction conditions on the rate of enzymic polymerization of pyrogallol using laccase, Process Biochemistry 40 (3-4) (2005) 1175-1182
5. Cho, N. S., Park, J. H., Lee, S. K., Lee, J.-H., Shim, H.-K., Park, M.-J., Hwang, D.-H.; Jung, B.-J. Saturated and efficient red light-emitting fluorene-based alternating polymers contai-ning phenothiazine derivatives, Macromolecules 39 (2006) 177-183.
6. Alam, M. M., Jenekhe, S. A. Polybenzobisazoles Are Efficient Electron Transport Materials for Improving the Performance and Stability of Polymer Light-Emitting Diodes, Chemistry of Material, 14 (2002) 4775-4780.
7. Letheby, H. On the production of a blue substance by the electrolysis of sulfate of aniline, Journal of Chemical Science, 15 (1862) 161-163.
8. 8. Szaways, E.C. Electrolytic preparation of induline dyes, Journal of the Chemical Society, Transactions 77 (1990) 207-212.
9. Saxena, V, Malhotra, B.D. Prospects of conducting polymers in molecular electronics, Cur-rent Applied Physics, 3 (2003) 293-305.
10. Kumar, D, Sharma, R.C. Advances in conductive polymers, European Polymer Journal, 34 (1998) 1053-1060.
11. Tezel, R.N, Kaya, İ. Thiophene substituted phenothiazine polymers: Design, synthesis and characterization, Arabian Journal of Chemistry, 13 (2020) 3123-3136.
12. Doğan, F., Ozdek, N., Selcuki, N.A, Kaya, I. The synthesis, characterization and effect of molar mass distribution on solid-state degradation kinetics of oligo(orcinol), Journal of Thermal Analysıs and Calorımetry, 138(1) (2019) 163-173.
13. Dogan, F, Kaya, İ., Solid State Decomposition Kinetics of Green Light Emitting Polyphe-nol Nanoparticles , Materıals Focus, 5(1) (2016) 5-10.
14. Hsieh, T.S., Wu, J.Y,. Chang, C.C. Multiple fluorescent behaviors of phenothiazine-based organic molecules. Dyes and Pigments, 112 (2015) 34-41.
15. Hemgesberg, M., Bayarmagnai, B., Jacobs, N., Bay, S., Follmann, S., Wilhelm, C., Zhou, Z., Hartmann, M., Müller, T. J. J., Ernst, S., Wittstock, G, Thiel, W. R. Structurally stressed PT09SBA: A close look at the properties of large pore photoluminescent, redox-active meso-porous hybrid silica. RSC Advances, 3 (2013) 8242-8253.
16. Bohn, C., Sadki, S., Brennan, A.B, Reynolds, J.R. In Situ Electrochemical Strain Gage Mon-itoring of Actuation in Conducting Polymers. Journal of The Electrochemical Society, 149 (2002) E281-E285
17. Colladet, K., Nicolas, M., Goris, L., Lutsen, L, Vanderzande, D. Low-band gap polymers for photovoltaic applications. Thin Solid Films, 7-11 (2004)
18. Doğan, F., Kaya, İ, Temizkan, K. Chemical oxidative synthesis and characterization of poly (8-hydroxyquinoline) particles. Journal of Macromolecular Science Part A-Pure and Applied Chemistry, 51 (2014) 948-961.
19. Tang, W., Liu, Y., Yang, X, Wang, C. Kinetic studies of the calcination of ammonium meta-vanadate by thermal methods. Industrial & Engineering Chemistry Research, 43(9) (2004) 2054-2059.
20. Kissinger, H.E. Reaction kinetics in differential thermal analysis, Analytical Chemistry, 29 (11) (1957) 1702–1706.
21. Akahira T, Sunose, T. Method of determining activation deterioration constant of electrical insulating materials, Research Report Chiba Institute of Technology, 16 (1971) 22–31.
22. Ozawa, T. A new method of analyzing thermogravimetric data, Bulletin of the Chemical So-ciety of Japan, 38 (11) (1965) 1881–1886.
23. Flynn, J.H, Wall, L.A. A quick, direct method for the determination of activation energy from thermogravimetric data, Journal of Polymer Science Part C: Polymer Letters, 4 (5) (1966) 323-328.
24. Friedman, H.L. New methods for evaluating kinetic parameters from thermal analysis data, Journal of Polymer Science Part C: Polymer Symposia, 6 (1965) 183-195.
25. Hwang, D.-H., Kim, S.-K., Park, M.-J., Lee, J.-H., Koo, B.-W., Kang, I.-N., Kim, S.-H., Zyung, T. Conjugated Polymers Based on Phenothiazine and Fluorene in Light-Emitting Di-odes and Field Effect Transistors, Chemistry of Material, 16 (2004) 1298-1303.
26. Gomurashvili, Z., Crivello, J. V. Monomeric and Polymeric Phenothiazine Photosensitizers for Photoinitiated Cationic Polymerization, Macromolecules 35 (2002) 2962-2969.
27. Tamoto, N., Adachi, C., Nagai, K. Electroluminescence of 1,3,4-Oxadiazole and Tripheny-lamine-Containing Molecules as an Emitter in Organic Multilayer Light Emitting Diodes, Chemistry of Material, 9 (1997) 1077-1085.

Hittite Journal of Science and Engineering, 2021, 8 (1) 71–77
ISSN NUMBER: 2148–4171
DOI: 10.17350/HJSE19030000215

Differential Pulse Voltammetric Determination of Clozapine in Drug Dosage Forms at Bismuth Film Electrode

Ozlem Kurtoglu Yigit **Ebru Gokmese** **Faruk Gokmese**
Hitit University, Department of Chemistry, Corum, Turkey

Article History:
Received: 2021/01/20
Accepted: 2021/03/06
Online: 2021/03/31

***Correspondence to**: Ebru Gokmese, Hitit University, Department of Chemistry, 19030, Corum, Turkey*
E-Mail: ebrugokmese@hitit.edu.tr
Phone: +90 364 227 7000
Fax: +90 364 227 7005

ABSTRACT

A new differential pulse voltammetric method for the determination of clozapine in drug dosage forms has been described. In this study, the amount of clozapine in commercial forms has been determined at bismuth modified glassy carbon electrode by taking advantage of the electrochemical oxidation of it. The glassy carbon electrode was modified with $BiCl_3$ to prepare the bismuth film electrode. The acetate buffer solution at pH = 5.00 was selected as the supporting electrolyte in where the maximum current was observed for clozapine at the bismuth film electrode. The effect of pH on peak current and peak potential of clozapine was investigated by differential pulse voltammetry (DPV), and the effect of scan rate on the peak current was examined by cyclic voltammetry (CV). With this developed voltammetric method, the detection limit for clozapine in the working range of 1 µM and 10 µM was found to be 6.112×10^{-9}. The amount of clozapine in the drug tablets was stated after the determination of analytical parameters. The recovery study was executed to check the accuracy and precision of the applied method.

Keywords:
Clozapine; bismuth film; drug analysis; modified electrode; differential pulse voltammetry

INTRODUCTION

Clozapine, which has a heterocyclic structure is 8-chloro-11-(4-methyl-1-piperazinyl)-5H-dibenzo-diazepine and Fig. 1 shows the chemical structure of this compound [1,2]. Clozapine, which is a strong antipsychotic agent from the dibenzodiazepine group, is called a typical antipsychotic since it has typical pharmacological and clinical features. Many studies comparing clozapine with traditional antipsychotics have shown that clozapine is at least as effective as traditional antipsychotics, even in some cases, this effect has increased [3].

Clozapine has been used in the treatment of patients with schizophrenic resistant to treatment who are caused by neuroleptic drugs that block the typical D2 receptor and develop unsuccessful physiological conditions. Also, clozapine treatment as in conventional antipsychotics stops the abnormal movements of Tardive dyskinesia and clozapine can additionally cure the defect of movement. On the other hand, clozapine is partially active in the treatment of tardivdistonia [4, 5]. Clozapine is also used to treat some schizophrenic patients cannot be treated by traditional neuroleptic drugs. Since the analysis of clozapine in pharmaceutical and chemical liquids is important, different analytical methods such as chromatography [6,7] and spectrophotometry [8] have been used to determine dosage forms. Studies on the therapeutic and toxic effects of drugs have shown that sensitive methods are required to obtain results at the trace level. The sensitivity of the studies with spectroscopic methods is not sufficient. Voltammetric and polarographic studies of the electrochemical behavior of clozapine are available in the literature [9,10]. To date, techniques for the detection of clozapine, including high-performance liquid chromatography, spectrophotometry, chemiluminescence, capillary electrophoresis, and titrimetry, are available [11, 12]. These methods, however, are exhausting, costly, and require the pretreatment of samples. On the other hand, electrochemical techniques such as voltammetry supply a wide linear working range as well as high precision, low cost, and high accuracy. Therefore, studies on the electrochemistry of drugs have increased in recent years [13, 14]. Since clozapine is a good electroactive substance, electroanalytical results of oxidation behavior in different electrodes have been described [15,16].

Electrochemical techniques are strong and multipurpose analytical techniques that can easily solve many pharmaceutical-related problems. Especially vol-

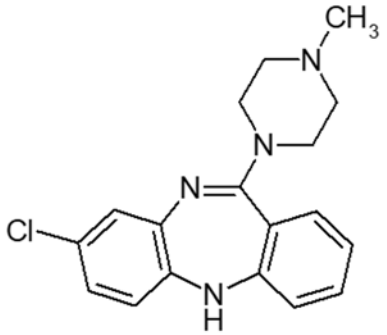

Figure 1. The chemical structure of Clozapine

tammetry is an effective electrochemical analytical technique with high sensitivity, selectivity, large linear range, and low-cost devices. Although there are studies on the oxidation behavior of clozapine in the literature, no studies have been found with bismuth film electrode. Therefore, a study on electrochemical properties, determination of clozapine, and validation of applied voltammetric techniques were performed on bismuth film electrode. This study aims to examine the electrochemical properties of clozapine and to develop a sensitive electrochemical methodology for direct and rapid determination of clozapine from pharmaceutical formulations on bismuth film electrode using voltammetric techniques.

MATERIAL AND METHODS

Reagents

Clozapine and drug tablets are commercially available. A 1×10^{-2} M stock solution of clozapine was prepared in methanol and stored in the fridge. In all voltammetric studies, standard solutions were prepared by diluting the stock solutions with methanol. The suitability of 0.04 M Britton-Robinson (pH 3.50-8.00) and 0.2 M acetate buffer (pH 3.50 - 8.00) as supporting electrolyte was investigated and acetate buffer was selected. Buffers and supporting electrolytes were prepared with CH_3COOH (Reidel de Haen, 100%), H_3PO_4 (Carlo Erba, 35%), H_3B0_3 (Merck), NaOH (Reidel de Haen). Glassy carbon electrode was polished with slurries prepared from 1, 0.3 and, 0.05-micron size alumina powders and deionized water on the Buehler cloth. Also, argon gas (99% purity), methanol, and deionized water were used without any purification. To prepare a bismuth-coated glassy carbon electrode, 100 ppm $BiCl_3$ was prepared in 0.2 M KCl solution.

Apparatus and Instrumentation

Voltammetric studies were performed with CH Instruments 660C Model Potentiostat/Galvanostat. A triple electrode system formed bismuth coated glassy carbon electrode as a working electrode, Ag/AgCl electrode as reference electrode and platinum wire as a counter electrode was used. All voltammetric responses were taken versus the Ag/AgCl electrode. pH measurements were made with a PL-700PV model pH meter. The deionized water used in the preparation of the solutions was obtained from the Zeneer Power-Water Purification System. Measurements executed at ambient laboratory temperature.

Differential pulse voltammetry conditions were: Pulse amplitude, 50 mV; pulse width 50 ms; scan rate, 20 mV s^{-1}.

The Procedure of Pharmaceutical Preparations

The stock solution of 1×10^{-2} M clozapine was prepared daily in methanol. The standard solutions for the calibration study were prepared by diluting the appropriate volumes of these stock solutions. The measurements for individual concentration was repeated three times. After preparing the calibration graph (10^{-5} µM - 1 µM), the determination process was started from the drug tablet containing clozapine. Ten drug tablets (each tablet containing 25 mg clozapine according to the label) were weighed and well ground to a fine powder. The stock solution containing 1×10^{-2} M clozapine in methanol was prepared in a 100 mL volumetric flask.

RESULTS AND DISCUSSION

Preparation of Working Electrode

Bismuth-coated glassy carbon electrode is used as a working electrode. The first step of the modification process is polishing a commercial glassy carbon electrode (GC). Therefore, the GC (CHI 104, 0.071 cm^2 area) was polished successively in alumina slurries in which 1-, 0.3-, and 0.05 µm alumina particles, respectively, as described previously [17]. The coating solution was 100 ppm $BiCl_3$ solution in 0.5 M KCl supporting electrolyte. The aqueous medium was buffered with acetic acid/sodium acetate buffer solution. The coating step was performed to dip the GC in the coating solution and then apply the amperometric technique at -1 V potential. The electrochemical characterization of the bismuth coated GC electrode was achieved by using 1 mM dopamine and ferrocene solutions. The voltammograms for dopamine and ferrocene were demonstrated in Fig. 2 and Fig. 3, respectively.

When we compare the voltammetric results from both the bare GC and bismuth coated GC, it is distinguished that the electrode was successfully coated with bismuth. At the bare GC, there is only one anodic peak observed at about 0.5 V potential with an accompanying cathodic peak. These peaks belong to electrochemical oxidation and reduction of

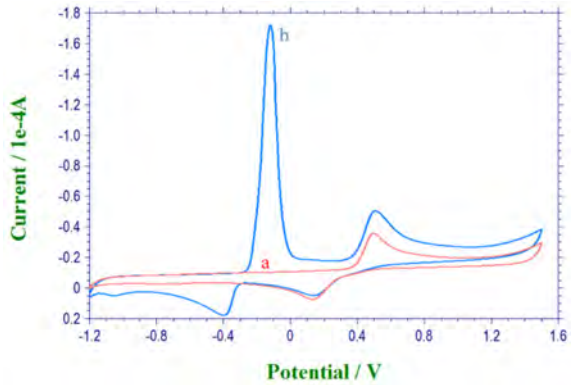

Figure 2. The cyclic voltammograms for 1 mM dopamine solution in 0.5 M NaCl supporting electrolyte at a) the bare GC electrode and b) the bismuth coated GC (bismuth film) electrode (scan rate: 0.1 Vs^{-1}).

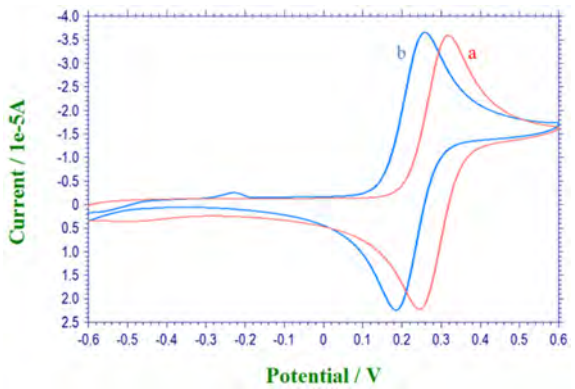

Figure 3. The cyclic voltammograms for 1 mM ferrocene solution in 0.1 M TBATFB supporting electrolyte in acetonitrile at a) the bare GC electrode and b) the bismuth coated GC (bismuth film) electrode (scan rate: 0.1 Vs^{-1}).

dopamine. On the other hand, one different anodic peak additionally shows up at about -0.1 V potential, which is more negative than that of dopamine. This new narrow peak was attributed to the oxidation of bismuth on the GC surface (Fig. 2).

In addition to the dopamine test, the electrochemical behavior of ferrocene also supported the coating of GC with bismuth. Fig. 3 shows the cyclic voltammograms of 1 mM ferrocene solutions. The first one belongs to the electrochemical oxidation of ferrocene at bare GC electrode. On the other hand, the second one represents the same reaction but at the bismuth coated GC electrode. As shown from the results, there are some differences between the two voltammograms. The oxidation potential shifted to a more negative value because of the surface change. This behavior gave a hint about the potential catalytic effect of bismuth. Besides, a new oxidation peak showed up at around -0.2 V in the case of bismuth coated GC electrode. This potential is very near to the oxidation of bismuth on the surface. These results confirmed the modification of the GC electrode with bismuth and preparation of bismuth coated GC electrode.

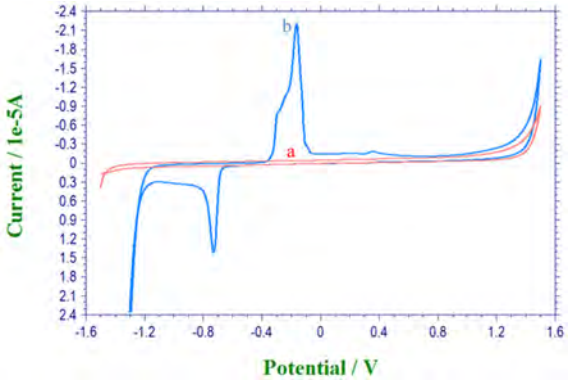

Figure 4. The cyclic voltammograms for 2 µM clozapine solution in 0.2 M acetate buffer (pH=5.00) solution at a) the bare GC electrode and b) the bismuth coated GC (bismuth film) electrode (scan rate: 0.1 Vs^{-1}).

The Electrooxidation of Clozapine at Bismuth Modified GC Electrode

The electrooxidation of clozapine was investigated using two different electrodes. When the peak currents of clozapine at bare GC and bismuth coated GC electrodes were compared, the calculation showed that the peak current for the modified electrode (bismuth coated GC) is approximately 75 times higher than that of bare GC electrode. This result demonstrated that the new modified electrode was more sensitive than the commercial GC electrode (Fig. 4).

Determination of Optimum Conditions for Oxidation of Clozapine

The effects of pH and supporting electrolyte on the oxidation potential and peak current were monitoring various conditions. First, the conditions for which the highest current was observed for the oxidation of clozapine were determined. Using differential pulse voltammetry (DPV) technique, the dependence of peak current and potential on pH was investigated in both acetic acid/acetate and Britton Robinson buffer solutions as a supporting electrolyte. The results are tabulated in Table 1 for acetate and BR buffer solutions.

The change in the peak current with pH was also plotted (Fig. 5) as well as peak potential (Fig. 6).

According to the results given in Table 1 and the behaviors observed in Fig. 5 and Fig. 6, the maximum peak current was 0.5958 µA and obtained in an acetate buffer solution with a pH of 5. Fig. 5 shows the effect of pH on the oxidation of clozapine. As seen from the figure, anodic peak potentials away from positive values as the pH values increase. This change occurred as the potential value decreased from 384 mV to 216 mV as the pH increased from 3 to pH 8. This behavior shows that protons are involved in the electrode process.

Table 1. Voltammetric results for the study of pH and buffer type effect on the electrochemical oxidation of clozapine (2 µM clozapine, 0.2 M acetate buffer, 0.04 M BR buffer)

pH	Acetate Buffer		BR Buffer	
	Current(µA)	Potential (V)	Current(µA)	Potential (V)
3.5	0.357	0.444	0.171	0.384
5.0	0.596	0.320	0.380	0.328
6.5	0.032	0.204	0.540	0.264
8.0	0.583	0.080	0.489	0.216

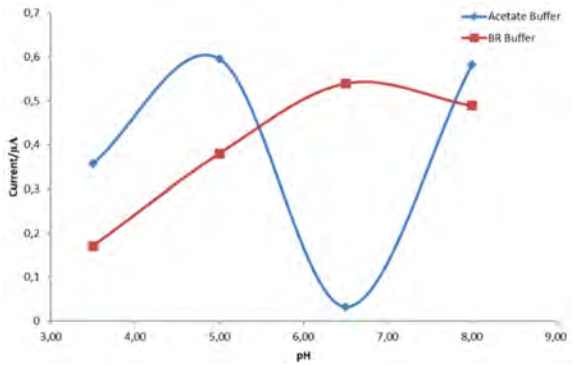

Figure 5. The effect of pH from different buffers on the peak current of 2 µM clozapine solution.

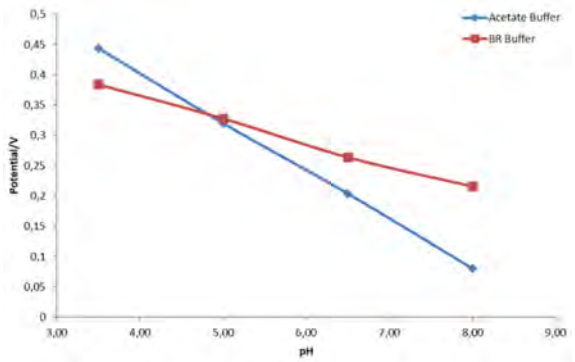

Figure 6. The effect of pH from different buffers on the peak potential of 2 µM clozapine solution.

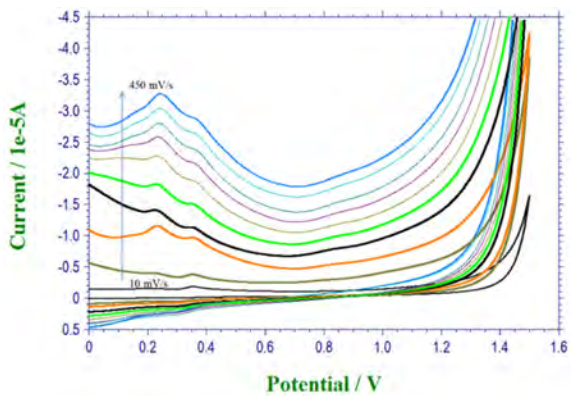

Figure 7. The cyclic voltammograms of 2 µM clozapine for different scan rates from 10 mVs^{-1} to 450 mVs^{-1} at bismuth film electrode in 0.2 M acetate buffer solution (pH=5.00).

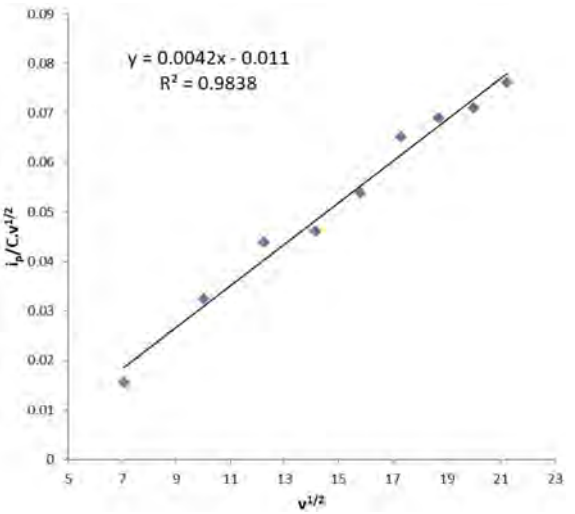

Figure 8. The dependence of current function ($Ip/Cv^{1/2}$) to the square root of scan rate ($v^{1/2}$) from CV study of 2 µM clozapine at bismuth film electrode in 0.2 M acetate buffer solution (pH=5.00).

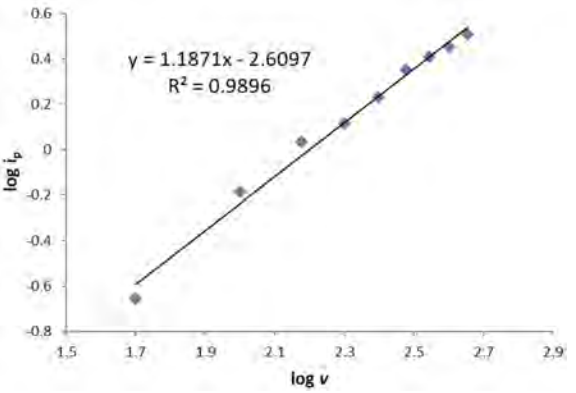

Figure 9. The log Ip–log v curve from CV study of 2 µM clozapine at bismuth film electrode in 0.2 M acetate buffer solution (pH=5.00).

The Variation of Current with The Scan Rate

The oxidation of clozapine (2 µM) has been investigated in acetate buffer solution (pH=5.0) by using cyclic voltammetry (CV). The voltammograms obtained from nine different scan rates between 50 mVs^{-1} and 450 mVs^{-1} were given in Fig. 7. In this range of scan rate values, there is a linear relationship between the square root of scan rate ($v^{1/2}$) and current function ($Ip/Cv^{1/2}$). This behavior can be seen from Fig. 8 and shows that this is an adsorption controlled current. Furthermore, when the logarithm of the peak current and the scan rate is examined (Fig. 8), the slope is found to be 1.1834, which is another criterion that the current is adsorption controlled [18].

Determination of Analytical Working Range

The analytical working range was determined according to the measurements obtained by the DPV technique in acetate (pH = 5.00) buffer solution in the concentration range of 1 µM–10 µM (Fig. 10). Voltammograms at different concentrations for clozapine were recorded under

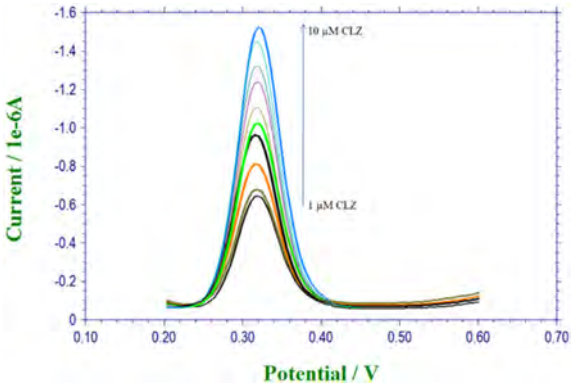

Figure 10. The differential pulse voltammograms of clozapine for different concentrations from 1 µM to 10 µM at bismuth film electrode in 0.2 M acetate buffer solution (pH=5.00).

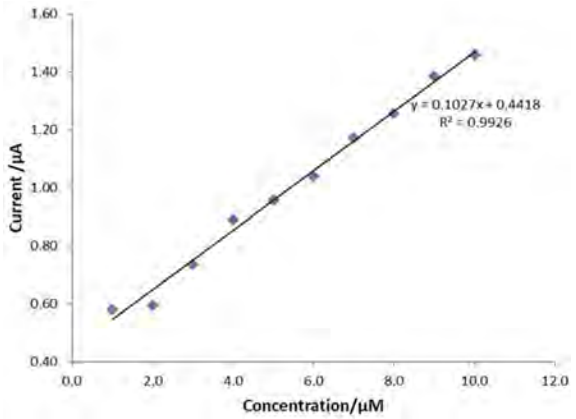

Figure 11. The calibration graph for determination of clozapine at bismuth film electrode in 0.2 M acetate buffer solution (pH=5.00).

optimal analytical conditions. For clozapine, a calibration curve with high linearity was obtained in this medium in the range of 1 µM-10 µM (Fig. 11).

According to the equations, LOD=3 s/m and LOQ=10 s/m, the limit of detection and the limit of quantitation were calculated using measured peak currents, respectively. Where "s" is the standard deviation of peak currents (for three measurements) and "m" is the slope of the calibration curve [19]. LOD and LOQ were calculated as 6.112×10^{-9} mol/L and 2.0373×10^{-8} mol/L for bismuth-modified glassy carbon electrodes, respectively (Table 2).

On the other hand, there are several references in the literature about the determination of CLZ. The results of these methods as well as that of the present study are given in Table 3. Table 3 contains the information about these studies such as working electrodes, the techniques used, the linear ranges, and LOD.

Analytical Application and Recovery Study

Commercial drug tablets containing 25 mg of clozapine per tablet were exactly weighed and ground to a fine powder. A stock solution of concentration 1×10^{-2} mol/L was prepared by weighing the appropriate amount of the powdered solid and dissolving it in methanol. Appropriate solutions were prepared by taking proper volumes of the stock solution and diluting with 0.2 mol/L acetic acid/sodium acetate buffer solution used as supporting electrolyte. The quantity of clozapine in the trading tablet was calculated as 25.3 ± 2.2 mg using the calibration equation.

Besides, a recovery test was performed for the developed method, and the results are given in Table 5. According to the results, the new analytical method has shown that tablets can be applied successfully without any intervention in the determination of clozapine. When the amount of clozapine was added, and the amount of clozapine detected was compared, recovery from the commercial tablets was found to be 97.00%.

Table 2. Analytical parameters of the calibration graph for differential pulse voltammetric determination of clozapine at bismuth film electrode in 0.2 M acetate buffer solution (pH=5.00)

Parameters	*Results*
Linear concentration range, mol/L	*from 1×10^{-6} to 10×10^{-6}*
Slope, µA M^{-1}	*0.10274*
SD of slope	*0.00314*
The correlation coefficient, r	*0.9963*
Regression standard deviation, sr	*2.850×10^{-8}*
Number of measurements	*3*
LOD, mol L^{-1}	*6.112×10^{-9}*
LOQ, mol L^{-1}	*2.0373×10^{-8}*

Table 3. The comparison of different studies in the literature with the present study for voltammetric determination of CLZ

WE	*Technique*	*Linear Range*	*LOD*
HMDE	*SWAdCS*	*1.0 – 3.3 nM*	*0.45 nM*
TiO_2NP/MCPE	*AD-DPV*	*0.5 – 45 µM*	*61.00 nM*
PPY/CNT/GCE	*LSV*	*0.01 – 5.00 µM*	*3.00 nM*
EPGCE	*AdSV*	*0.1 – 1 µM*	*8.00 nM*
F_3O_4/Ala/Pd/GCE	*DPV*	*3 – 70 nM*	*1.53 nM*
Ru/TiO_2/CPE	*SWV*	*0.9 – 40 µM*	*0.43 nM*
Bi/GCE	*DPV*	*1 – 10 µM*	*6.11 nM*

WE: Working Electrode, HMDE: hanging Mercury Drop Electrode NP: Nanoparticles, MCPE: Modified Carbon Paste Electrode, PPY: PolyPyrrole, CNT: Carbon Nanotube, GCE: Glassy Carbon Electrode, EP: Electrochemically Pretreated, SWAdCS: Square Wave Adsorptive Cathodic Stripping, AD-DPV: Adsorptive Differential Voltammetry, LSV: Linear Sweep Voltammetry.

CONCLUSION

In this study, the electrochemical oxidation property of clozapine on the bismuth coated glassy carbon electro-

Table 4. Result for the determination of clozapine in a drug dosage form

Drug form	*Declared*	*Found[a]/mg*	*RSD, %*
Tablet	*25 mg per tablet*	*25.3 ±0.3*	*1.2*

a: Average of 3 different measurements.

Table 5. Recovery study for the determination of clozapine in a drug tablet

Sample	*Spiked*	*Found*	*Recovery, %*	*RSD, %*
Drug tablet	*6.536x10-3mg*	*6.363x10^{-3}mg*	*97*	*1.32*

de was investigated by using DPV and CV techniques. Oxidation peaks between 0.3 V and 0.6 V were determined on voltammograms taken with acetate buffers (pH 3.50-8.00) at different pH values. Voltammograms were obtained by using the DPV technique in different electrolytes selected in acidic and basic regions. The working medium was determined according to the obtained pH-Ip change.

When the peak currents of clozapine in the glassy carbon electrode (0.330 µA) and modified electrode (21.69 µA) are compared, the peak current at the modified electrode is about 70 times higher, indicating that the modified electrode is more sensitive than the bare GC electrode. As a result, this study suggests a new method for the determination of CLZ. As seen from Table 3 some different methods and electrodes have been used for the determination of CLZ but it is the first time to use the bismuth modified carbon electrode for this purpose. The linear range and LOD of this method are near the other methods.

ACKNOWLEDGEMENT

The authors would like to express their gratitude to Selehattin Yılmaz, who provided the drug active substance.

References

1. Mohamed A, Sheikka MA. Spectrophotometric determination of clozapine based on its oxidation with bromate in a micellar medium. IL Farmaco, 59 (2004) 907. DOI: 10.1016/j.farmac.2004.07.008.
2. Hammam E, Tawfik A, Ghoneim AA. Adsorptive stripping voltammetric quantification of the antipsychotic drug clozapine in bulk form, pharmaceutical formulation and human serum at a mercury electrode. Journal of Pharmaceutical Biomedical Analysis 36 (2004) 149. DOI: 10.1016/j.jpba.2004.04.012.
3. Güven FM, Birsöz S. Klozapin ve Şizofreni Sağaltımındaki Yeri. Klinik Psikiyatri 4 (2001) 124-128.
4. Lieberman JA, Saltz BL, Johns CA, Pollack S, Borenstein M, Kane J. The effects of clozapine on tardive dyskinesia. The British Journal of Psychiatry 158 (1991) 503. DOI: 10.1192/bjp.158.4.503.
5. Freudenreich O, Henderson DC, Walsh JP, Culhane M.A., Goff DC. Risperidone augmentation for schizophrenia partially responsive to clozapine: A double-blind, placebo-contolled trial. Schizophrenia Research 92 (2007) 90. DOI: 10.1016/j.schres.2006.12.030
6. Guitton C, Kinowski JM, Regis A., Bressolle F. Determination of clozapine and its major metabolites in human plasma and red blood cells by high-performance liquid chromatography with ultraviolet absorbance detection. Journal of Chromatography B 690 (1997) 211-222. DOI: 10.1016/S0378-4347(96)00362-3.
7. Taha EA, Soliman SM, Abdellatef HE, Ayad MM. Colorimetric methods for the determination of some tricyclic antidepressant drugs in their pure and dosage forms, Mikrochimica Acta 140 (2002) 175-182. DOI:10.1007/s00604-002-0904.
8. Gosser Jr. DK, Cyclic Voltammetry: Simulation and analysis of reaction mechanisms, VCH Publishers, New York, 1983, ISBN: 978-1560810261.
9. Mashhadizadeh MH, Afshar E. Electrochemical investigation of clozapine at TiO_2 nanoparticles modified carbon paste electrode and simultaneous adsorptive voltammetric determination of two antipsychotic drugs. Electrochimica Acta 87 (2013) 816. DOI: 10.4103/2229-5186.79345.
10. Weber JM, Volke J. 75 years in the polarography of pharmaceuticals and physiologically active substances. Pharmazie 46 (1991) 853.
11. Edno L, Combourieu I, Cazenave M, Tignol J. Assay for quantitation of clozapine and its metabolite N-desmethyl clozapine in human plasma by high performance liquid chromatography with ultraviolet detection. Journal of Pharmaceutical and Biomedical Analysis 16 (1997) 311. DOI: 10.1016/s0731-7085(97)00048-4.
12. Raggi MA, Bugamelli F, Mandrioli R, Sabbioni C, Volterra V, Fanali S. Rapid capillary electrophoretic method for the determination of clozapine and desmethylclozapine in human plasma, Journal of Chromatography A 916 (2001) 289-296. DOI: 10.1016/S0021-9673(01)00520-9.
13. Elqudaby HM, Mohamed GG, El-Din GMG. Electrochemical behaviour of trimebutine at activated glassy carbon electrode and its direct determination in ürine and pharmaceutics by square wave and differential pulse voltammetry. International Journal of Electrochemical Science 9 (2014) 856-869.
14. Demirbilek E, Saglıkoglu G, Yılmaz S. Electrochemical investigation of isoniazid on poly (p-aminobenzene sulfonic acid) film modified glassy carbon electrode. International Journal of Electrochemical Science 10 (2015) 4428-4438.
15. Shahrokhian S, Kamalzadeh Z, Hamzehloei A. Electrochemical determination of clozapine on MWCNTs/New coccine doped PPY modified GCE: An experimental design approach, Bioelectrochemistry 90 (2013) 36. DOI: 10.1016/j.bioelechem.2012.10.002.
16. Tammari E, Neshadali A, Lotfi S, Veisi H. Fabrication of an electrochemical sensor based on magnetic nanocomposite Fe_3O_4/β-Alanine/Pd modified glassy carbon electrode for determination of the nanomolar level of clozapine in biological model and pharmaceutical samples. Sensors and Actuators B: Chemistry 241 (2017) 879. DOI: 10.1016/j.snb.2016.11.014.
17. Gökmeşe F, Gökmeşe E, Emire Z. A simple and rapid method for preparing carbon nanopore electrode ensemble coating a glassy carbon electrode with chromate. Hittite Journal of Science and Engineering 3 (2016) 1. DOI: 10.17350/HJSE19030000025.
18. Bard AJ, Faulkner LR. Electrochemical Methods; Fundamentals and Applications. John Wiley and Sons, Inc., New York, 2001, ISBN: 0-471-04372-9, page 833.
19. Shrivastava A., Gupta VB. Methods for the determination of limit of detection and limit of quantitation of the analytical methods. Chronicles of Young Scientists 2 (2011) 21. DOI: 10.4103/2229-5186.79345.
20. K. Farhadi, A. Karimpour, Electrochemical behavior and

determination of clozapine on a glassy carbon electrode modified by electrochemical oxidation, Anal. Sci. 23, (2007) 479.
21. N.P. Shetti, D.S. Nayak, S.J. Malode, R.M. Kulkarni, An electrochemical sensor for clozapine at ruthenium doped TiO_2 nanoparticles modified electrode, Sensors and Actuators B: Chem., 247 (2017) 858.

Hittite Journal of Science and Engineering, 2021, 8 (1) 79–83
ISSN NUMBER: 2148–4171
DOI: 10.17350/HJSE19030000216

Evaluation of Oxidant-Antioxidant Status of Fluvoxamine on Human Lymphocyte Cell Culture

Suzan Muratoglu Severcan[1] Cinar Severcan[2] Mostafa Norizadeh Tazehkand[3] Zehra Safi Oz[4] Aslihan Gurbuz[5]

[1]Ankara University, Department of Forensic Chemistry and Forensic Toxicology, Ankara, Turkey
[2]Zonguldak Bulent Ecevit University, Department of Biochemistry, Zonguldak, Turkey
[3]Zonguldak Bulent Ecevit University, Department of Pharmaceutical Biotechnology, Zonguldak, Turkey
[4]Zonguldak Bulent Ecevit University, Department of Medical Biology, Zonguldak, Turkey
[5]Ankara University, Department of Biochemistry, Ankara, Turkey

Article History:
Received: 2021/02/27
Accepted: 2021/03/23
Online: 2021/03/31

***Correspondence to**: Suzan Muratoglu Severcan, Ankara University, Forensic Toxicology, Ankara, Turkey*
E-Mail: suzansevercan@gmail.com
Phone: +90 553 983 77 74

ABSTRACT

Depression is one of the prevalent psychiatric diseases in Turkey and the world. Fluvoxamine is a strong selective serotonin reuptake inhibitor (SSRI) that is used as an antidepressant. No study investigating the doses of Fluvoxamine treatment that may lead to a disruption in the oxidant-antioxidant balance on the cellular level in addition to its beneficial effects has been found in the literature. For this purpose, by creating Fluvoxamine application groups at the doses of 7.5, 15, 30 and 60 µM and durations of 24 and 48 hours on human lymphocyte cell cultures, we investigated the total oxidant status (TOS), total antioxidant status (TAS) and oxidative stress index (OSI). According to the results of the study, the TOS levels of all dose groups increased significantly in the 24- and 48-hour applications ($p<0.05$). While the TAS levels significantly increased in the 24-hour application of the doses of 7.5 and 15 µM and 48-application of the dose of 7.5 µM, they significantly decreased in the 24- and 48-hour applications of the doses of 30 and 60 µM ($p<0.05$). The OSI level increased significantly in the 24- and 48-hour applications of the doses of 30 and 60 µM. The results of our study demonstrated that, in the 24- and 48-hour applications of the doses of 30 and 60 µM, the antioxidant system could not compensate and the cells exposed to oxidative stress.

Keywords:
Human lymphocyte cell culture; Total oxidant status (TOS); Total antioxidant status (TAS); Oxidative stress index (OSI); Fluvoxamine.

INTRODUCTION

Depression is one of the most prevalent psychiatric disorders, and it causes severe attacks, domestic unrest, suicidal tendencies and significant socioeconomic losses in individuals. It was reported that approximately 21% of the population worldwide is affected by depression (1,2). The prevalence of depression in Turkey is approximately 10% (3). Risk factors for depression include sex, middle age, being single, low income and disability, in addition to a history of depression in the family, negative childhood experiences, other psychiatric disorders and chronic conditions like diabetes (4). The pathophysiology of depression has not been completely understood yet. It has been associated with monoaminergic neurotransmitters (serotonin, norepinephrine and dopamine) in the brain. In clinical psychiatry, distinguishing bipolar and major depression is highly important (5). The most frequently used method in the treatment of depression is prescription of antidepressant drugs (6). The usage rates of antidepressants increased between 2000 and 2010 in Europe (7). Although antidepressant use in Turkey has increased in recent years, it was reported that it is still under the OECD average of 63 doses per 1000 individuals per day as 44 doses (8).

Free radicals are molecules containing an unpaired electron in an atomic orbit. In the presence of an unpaired electron, these radicals are unstable and highly reactive. The affinity of these radicals to bond with structures like proteins, lipids, nucleic acids and enzymes is high. When free radicals bond with biomolecules that are important for the maintenance of the metabolism, they disrupt their structures. In the normal physiological process, antioxidant molecules can scavenge free radicals, but in the case that free radical production can-

not be compensated by the antioxidant mechanism, oxidative stress develops. The increasing oxidative stress may lead to inflammation, ageing, diabetes, cardiovascular disorders and some types of cancer (9).

Fluvoxamine is a second-generation selective serotonin reuptake inhibitor (SSRI) that is used in the treatment of major depressive disorder, obsessive-compulsive disorder, anxiety and eating disorders. In the serotonin (5-hydroxytryptamine) metabolism, it specifically inhibits the reuptake of 5HT (10).

No study on the oxidative stress and antioxidant status of Fluvoxamine on cell cultures has been encountered in the literature. In addition to the toxic effects of drugs, it is also important to assess them in terms of dose-dependent oxidative stress and antioxidant status. This is why we aimed to examine the total oxidant status (TOS), total antioxidant status (TAS) and oxidative stress index (OSI) in human lymphocyte cultures.

MATERIAL AND METHOD

For the study, individuals who were voluntary, healthy, at close ages to each other, did not use any medication, did not use any special dietary supplement and did not smoke were selected as blood donors (2 female and 2 male participants at the ages of 18-25). These individuals filled out an informed consent form and voluntarily participated in the study.

This project was approved by the Clinical Studies Ethics Board of Zonguldak Bülent Ecevit University on the date of 20.06.2019 and with the protocol number of 2019-97-12/06.

Chemicals

Liquid Fluvoxamine at 99% purity was purchased from Sigma. Fig. 1 shows its chemical structure.

Cell Culture

The LD50 value was determined as 60 µM by conducting a preliminary study with the method reported by Norizadeh Tazehkand and Topaktas (11). For the study, the Fluvoxamine dose groups were determined by starting with the LD50 value as 60 µM, 30 µM, 15 µM and 7.5 µM for applications of 24 and 48 hours. In addition to these, a control group on which no Fluvoxamine application was made was selected. A total of 36 cell cultures including 4 cell cultures in each group were formed. The cell cultures were formed under sterile conditions by taking 0.2 ml of peripheral blood (1/10 heparinized) and adding it into 2.5 ml of chromosome medium. The cells were incubated in an incubator at 37±1°C for 68 hours (12). The determined Fluvoxamine doses were added to the cell cultures at the 24th and 48th hours.

Biochemical Analyses

After 68 hours, the tubes were centrifuged at 2000 rpm for 10 min. The supernatants were collected for TAS, TOS and OSI measurements and kept at -80°C.

TAS Measurement

TAS level measurement was made with a Rel Assay Diagnostics Kit (Catalog No: RL0017). The kit's method is based on the antioxidants in the sample reducing the dark blue-green ABTS radical into a colorless ABTS form. The absorbance change observed at 660 nm is calculated in relation to the total antioxidant level of the sample. The experiment is calibrated with a stable antioxidant standard solution that is an analog of vitamin E and known as the Trolox equivalent. The results are expressed as µmol / L.

TOS Measurement

TOS level measurement was made with a Rel Assay Diagnostics Kit (Catalog No: RL0024). In the kit's method, oxidants found in the sample oxidize the ferrous ion-chelator complex into ferric ion. The oxidation reaction is prolonged by enhancer molecules that are abundantly present in the reaction medium. This way, the ferric ions create a colored complex with chromogenic in the acidic environment, and the total oxidant molecule amount is determined spectrophotometrically. The experiment is calibrated by hydrogen peroxide, and the results are expressed in the form of micromolar hydrogen peroxide equivalent per liter (µmol H_2O_2 Equiv./L).

OSI Value

The TAS and TOS units were converted into µmol, and the OSI value was calculated as the percentage value of the TOS/TAS ratio.

Data Analysis

The SPSS (Statistical Package for the Social Sciences) version 25 software was used to analyze the data obtained in the study and create tables. Kruskal Wallis test was used to determine the significance levels of intergroup differences. For the significance values of $p<0.05$, Mann-Whitney U test was used to determine the significance of the difference between 2 groups. For the comparisons

Table 1. TAS median (min-max) levels of all groups and significant difference

Fluvoksamin administration	*n*	*Exposing time (hours)*	*TAS (mmol / L)*	*p value*
Control	4	*none*	*0,22 (0,2-0,25)*	-
7,5 µM	4	*24*	*0,26 (0,21-0,28)*	*0,144*
15 µM	4	*24*	*0,34 (0,31-0,38) **	*0,021*
30 µM	4	*24*	*0,08 (0,03-0,08) **	*0,020*
60 µM	4	*24*	*0,07 (0,06-0,09) **	*0,020*
7,5 µM	4	*48*	*0,24 (0,17-0,29)*	*1*
15 µM	4	*48*	*0,35 (0,21-0,39)*	*0,110*
30 µM	4	*48*	*0,08 (0,03-0,09) **	*0,021*
60 µM	4	*48*	*0,07 (0,03-0,09) **	*0,021*

n:number of cell culture, *significant difference compare to Group 1

between 2 groups, $p<0.05$ was accepted as statistically significant. To examine the correlations between the parameters, Spearman's correlation analysis was conducted between the non-normally distributed groups.

RESULTS

The significance of the difference among all groups in terms of the TAS, TOS and OSI values was determined (respectively, $p=0.000$, $p=0.000$, $p=0.001$).

The TAS levels of the groups in comparison to the control did not differ significantly in 24-hour application of 7.5 µM dose and 48-hour applications of 7.5 µM and 15 µM doses while an significantly increase was measured in the 24-hour application of the 15 µM dose. However, the groups of 24- and 48-hour applications of the 30 and 60 µM doses significantly decreased in comparison to the control (Table 1 and Fig. 1).

The TOS levels of the groups increased significantly in comparison to the control in the 24- and 48-hour applications of all doses (Table 2 and Fig. 2).

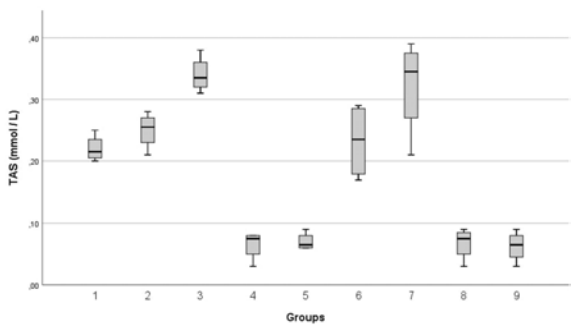

Figure 1. The TAS levels of groups

Table 2. TOS median (min-max) levels of all groups and significant difference

Fluvoksamin administration	*n*	*Exposing time (hours)*	*TOS (µmol / L)*	*p value*
Control	4	*none*	*1,04 (0,87-1,20)*	-
7,5 µM	4	*24*	*1,34 (1,15-1,42) **	*0,043*
15 µM	4	*24*	*1,69 (1,47-1,95) **	*0,021*
30 µM	4	*24*	*1,8 (1,62-1,91) **	*0,021*
60 µM	4	*24*	*1,87 (1,63-2,09) **	*0,021*
7,5 µM	4	*48*	*1,25 (1,22-1,28) **	*0,021*
15 µM	4	*48*	*1,48 (1,31-1,72) **	*0,021*
30 µM	4	*48*	*1,8 (1,78-2,1) **	*0,021*
60 µM	4	*48*	*2,13 (1,9-2,3) **	*0,021*

n:number of cell culture, *significant difference compare to Group 1

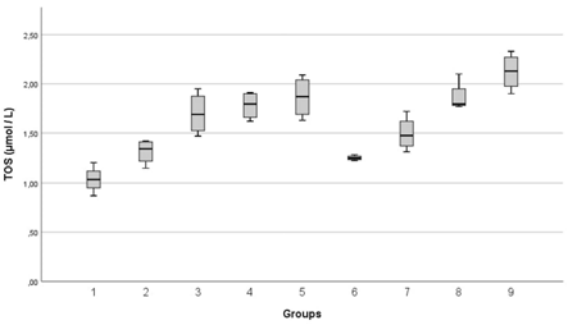

Figure 2. The TOS levels of groups

Table 3. OSI median (min-max) levels of all groups and significant difference

Fluvoksamin administration	*n*	*Exposing time (hours)*	*OSI*	*p value*
Control	4	*none*	*0,47(0,41-0,55)*	-
7,5 µM	4	*24*	*0,53 (0,51-0,55)*	*0,386*
15 µM	4	*24*	*0,51 (0,42-0,58)*	*0,386*
30 µM	4	*24*	*2,43 (2,03-6,3) **	*0,021*
60 µM	4	*24*	*2,78 (1,94-3,48) **	*0,021*
7,5 µM	4	*48*	*0,55 (0,44-0,74)*	*0,248*
15 µM	4	*48*	*0,44 (0,42-0,62)*	*0,564*
30 µM	4	*48*	*2,62 (1,97-6) **	*0,021*
60 µM	4	*48*	*3,52 (2,28-6,33) **	*0,021*

n:number of cell culture, *significant difference compare to Group 1

The difference in the OSI levels in comparison to the control was not significant in the 24- and 48-hour Fluvoxamine applications at the doses of 7.5 and 15 µM. In the 24- and 48-hour applications of the 30 and 60 µM doses, the

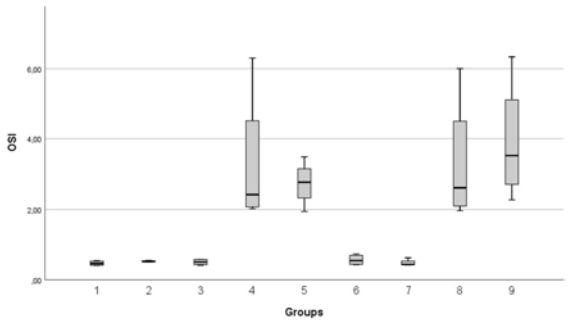

Figure 3. The OSI levels of groups

Table 4. Correlation among parameters

Fluvoksamin administration		*TAS*	*TOS*	*OSI*
TAS	*r value*	*1*	*-0,514*	*-0,906*
	p value	-	*0,001 ** *	*0,000 ** *
TOS	*r value*	*-0,514*	*1*	*0,743*
	p value	*0,001 ** *	-	*0,000 ** *
OSI	*r value*	*-0,906*	*0,743*	*1*
	p value	*0,000 ** *	*0,000 ** *	-

** Correlation is significant at the 0,01 (2-tailed)

OSI levels of the groups significantly increased when compared to the control (Table 3 and Fig. 3).

The results of the Spearman's correlation analysis are given in Table 4.

Accordingly, there were negative correlations between the TAS and TOS levels (Fig. 4) and between the TAS and OSI levels (Fig. 5) ($p<0.01$) and a positive correlation between the TOS and OSI levels ($p<0.01$) (Fig. 6).

DISCUSSION

Depression is a high-prevalence disease that reduces functional capacity and quality of life and causes comorbidities and mortalities. With the increasing number of cases in the last decade, many studies have been conducted, and new treatment methods have been developed. There are several different antidepressants that have been shown to be effective in randomized studies (12). Fluvoxamine is an antidepressant drug which is a strong SSRI. It is a highly lipophilic compound, in enters the cell fast and is used in the treatment of anxiety, bipolar disorder, obsessive-compulsive disorder and especially major depression (13).

An increase in reactive oxygen species (ROS) may be scavenged in the cellular physiological process by main an-

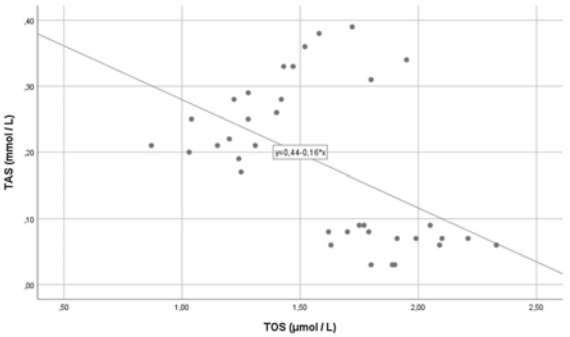

Figure 4. The correlation between TAS and TOS

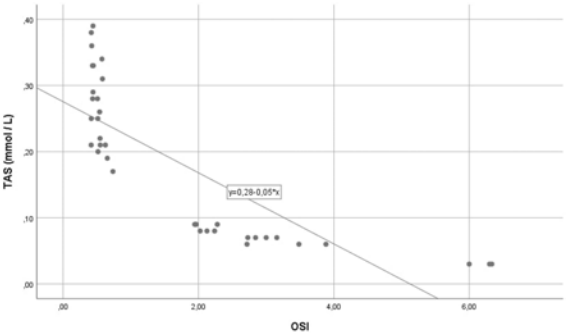

Figure 5. The correlation between TAS and OSİ

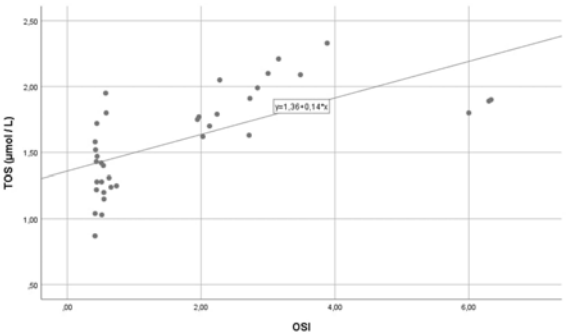

Figure 6. The correlation between TOS and OSİ

tioxidant system enzymes such as superoxide dismutase (SOD), catalase and glutathione peroxidase. By interacting with the biomolecules of cells such as lipids, proteins and nucleic acids, ROS may disrupt the natural structures of these molecules (14). With the method they developed, Erel proposed the measurement of TOS products rather than showing the oxidation products of lipids, proteins and DNA (15). They also proposed measuring the total antioxidant capacity rather than measuring different antioxidant molecules separately (16). They reported that it will be meaningful to interpret oxidative stress by calculating the percentage ratio of TOS/TAS (15,16).

İstifli et al. demonstrated that administration of Sertraline, which is an SSRI used as an antidepressant, on human lymphocyte cell cultures by LD50 (5 µg/mL) and 3.75 µg/mL for 24 and 48 hours and observed as a result that TOS and

OSI increased significantly (17). In the experimental animal models on which they applied lipopolysaccharides, Abdel-Salem et al. observed that, with Fluvoxamine treatment, oxidative stress decreased, and antioxidant molecules were increased in liver and brain tissues (18).

Although it has been reported that Fluvoxamine reduces oxidative stress and triggers the antioxidant system as a treatment, it is needed to know its doses that may disrupt the oxidant-antioxidant balance by contact with cells. According to the results of our study, it was observed that the TOS level significantly increased in the 24- and 48-hour applications of the included Fluvoxamine doses ($p<0.05$). As the dose increased in the groups, the mean and median values also increased. Considering the TAS levels of the dose groups, significant increases in the 24-hour applications of the 7.5 and 15 μM doses and the 48-hour application of the 7.5 μM dose ($p<0.05$), as well as an insignificant increase in the 48-hour application of the 15 μM dose, were observed. This situation indicates that, as a response to the increasing TOS, the cellular antioxidant system was induced. Despite this, the TAS levels significantly decreased in the 24- and 48-hour applications of the 30 and 60 μM doses ($p<0.05$). The results demonstrate that, at the doses of 30 and 60 μM, the cellular antioxidant system is disrupted against the increasing reactive oxygen species. The finding that clarifies this situation best is the OSI levels of the groups. The OSI level significantly increased in the 24- and 48-hour applications of the 30 and 60 μM doses ($p<0.05$). Although there was a significant increase in the TOS levels in the 24- and 48-hour applications of the 7.5 and 15 μM doses, there was no significant change in the OSI levels. These findings demonstrate that the cell was protected from oxidative stress with the increase in the antioxidant system as a response to the increase in ROS in the 24- and 48-hour applications of the 7.5 and 15 μM doses. According to our correlation analysis results, this significant relationship was also demonstrated by the pairwise comparisons of the TAS, TOS and OSI values.

CONCLUSION

The results of our study showed that, although the antioxidant system was able to scavenge the increased reactive oxygen species in the 24- and 48-hour applications of the 7.5 and 15 μM doses of Fluvoxamine which is used in depression treatment on the created human lymphocyte cell cultures, in the 24- and 48-hour applications of the 30 and 60 μM doses, this oxidative status could not be compensated by the antioxidant system, and the cells were subjected to oxidative stress.

The findings of our study clearly showed the doses of Fluvoxamine at which there would be oxidative stress on the cellular level. We believe that these results will provide a significant insight into protection of public health by making an important contribution to the literature.

References

1. Möller HJ, Bitter I, Bobes J, Fountoulakis K, Höschl C, Kasper S. Position statement of the European Psychiatric Association (EPA) on the value of antidepressants in the treatment of unipolar depression. European Psychiatry 27(2) (2012) 114-128.
2. Gadassi R, Mor N. Confusing acceptance and mere politeness: Depression and sensitivity to Duchenne smiles. Journal of Behavior Therapy and Experimental Psychiatry 50 (2016) 8-14.
3. Açıkgöz A, Dayı A, Binbay T. Üniversitede okuyan kız öğrencilerde depresyon prevalansı ve ilişkili faktörler. Cukurova Medicine Journal 43(1) (2018) 131-140.
4. Semenkovich K, Brown ME, Svrakic DM, Lustman PJ. Depression in type 2 diabetes mellitus: prevalence, impact, and treatment. Drugs 75(6) (2015) 577-587.
5. Casey DA. Depression in Older Adults: A Treatable Medical Condition. Primary Care 44(3) (2017) 499-510.
6. Yüzbaşıoğlu D, Avuloğlu Yılmaz E, Ünal F. Antidepresan ilaçlar ve genotoksisite. TÜBAV Bilim Dergisi 9(1) (2016) 17-28.
7. Gusmão R, Quintão S, McDaid D, Arensman E, Audenhove CA, Coffey C, Värnik C, Värnik P, Coyne J, Hegerl U. Antidepressant Utilization and Suicide in Europe: An Ecological Multi-National Study. PLoS One 8(6) (2013) e66455.
8. Health at a Glance 2019 : OECD Indicators. https://www.oecd-ilibrary.org/sites/43146d4b-en/index.html?itemId=/content/component/43146d4b-en, 20.02.2021, https://doi.org/10.1787/888934018089.
9. Lobo V, Patil A, Phatak A, Chandra N. Free radicals, antioxidants and functional foods: Impact on human health. Pharmacognosy Reviews 4(8) (2010) 118-126.
10. Otter J, McIntyre IM, Morhaime J, Cantrell L. A fluvoxamine-related fatality: Case report with postmortem concentrations. Forensic Science International 300 (2019) e31-e33.
11. Norizadeh Tazehkand M, Topaktas M. The in vitro genotoxic and cytotoxic effects of remeron on human peripheral blood lymphocytes. Drug and Chemical Toxicology. 38(3) (2015) 266-271.
12. Cuijpers P, Quero S, Dowrick C, Arroll B. Psychological Treatment of Depression in Primary Care: Recent Developments. Current Psychiatry Reports 21(12) (2019) 129.
13. Hashimoto K. Activation of sigma-1 receptor chaperone in the treatment of neuropsychiatric diseases and its clinical implication. Journal of Pharmacological Sciences 127(1) (2015) 6-9.
14. Rogrigo R. Oxidative stress and antioxidants: their role in human disease. Nova Science Publishers, pp. 2-18, New York, 2009.
15. Erel O. A new automated colorimetric method for measuring total oxidant status. Clinical Biochemistry 38 (2005) 1103–1111.
16. Erel O. A novel automated direct measurement method for total antioxidant capacity using a new generation, more stable ABTS radical cation. Clinical Biochemistry 37 (2004) 277– 285.
17. Istifli ES, Çelik R, Hüsunet MT, Çetinel N, Demirhan O, Ila HB. In vitro cytogenotoxic evaluation of sertraline. Interdisciplinary Toxicology 11(3) (2018) 181-188.
18. Abdel-Salam OME, Morsy SMY, Sleem AA. The effect of different antidepressant drugs on oxidative stress after lipopolysaccharide administration in mice. Experimental Clinical Science Journal 10 (2011) 290-302.